SHELL EFFECTS IN FISSION FRAGMENT MASS DISTRIBUTION OF NEUTRON DEFICIENT NUCLEI AROUND A$\sim$200

By

SHILPI GUPTA

PHYS01201404018

Nuclear physics Division

Bhabha Atomic Research Centre, Mumbai.

A thesis submitted to the
Board of Studies in Physical Sciences

In partial fulfillment of the requirements

For the Degree of

DOCTOR OF PHILOSOPHY

of

HOMI BHABHA NATIONAL INSTITUTE

June, 2020

Homi Bhabha National Institute

Recommendations of the Viva Voce Committee

As members of the Viva Voce Committee, we recommend that the dissertation prepared by **SHILPI GUPTA** entitled **"Shell effects in fission fragment mass distribution of neutron deficient nuclei around A∼200"** may be accepted as fulfilling the thesis requirement for the award of Degree of Doctor of Philosophy.

Chairman : Prof. B. K. Nayak

BK Nayak Date : 20|10|2020

Convener : Prof. A. Shrivastava

Aradhana Shrivastava Date : 20. 10. 2020

Member : Prof. K. Mahata

Mahata Date : 20. 10. 2020

Member : Prof. R. Tripathi

Rahul. Date : 20.10.2020

External Examiner : Prof. C. Bhattacharya

C. Bhattacharya Date : 20. 10. 2020

Final approval and acceptance of this dissertation is contingent upon the candidate's submission of the final copies of the thesis to HBNI.

I/We hereby certify that I/We have read this dissertation prepared under my/Our direction and recommend that it may be accepted as fulfilling the thesis requirement.

Aradhana Shrivastava Date : 20. 10. 2020.

Guide : Prof. A. Shrivastava

STATEMENT BY AUTHOR

This dissertation has been submitted in partial fulfillment of requirements for an advanced degree at Homi Bhabha National Institute (HBNI) and is deposited in the library to be made available to borrowers under rules of the HBNI.

Brief quotations from this dissertation are allowable without special permission, provided that accurate acknowledgement of source is made. Requests for permission for extended quotation from or reproduction of this manuscript in whole or in part may be granted by the Competent Authority of HBNI when in his or her judgment the proposed use of the material is in the interests of scholarship. In all other instances, however, permission must be obtained from the author.

Shilpi

SHILPI GUPTA

DECLARATION

I, hereby declare that the investigation presented in the thesis has been carried out by me. The work is original and the work has not been submitted earlier as a whole or in part for a degree/diploma at this or any other Institution or University.

Shilpi

SHILPI GUPTA

List of Publications arising from the thesis

Journal

1. Competing asymmetric fusion-fission and quasifission in neutron-deficient sub-lead nuclei
   Shilpi Gupta, K. Mahata, A. Shrivastava, K. Ramachandran, S.K. Pandit, P.C. Rout, V.V. Parkar, R. Tripathi, A. Kumar, B.K. Nayak, E.T. Mirgule, A. Saxena, S. Kailas, A. Jhingan, A.K. Nasirov, G.A. Yuldasheva, P. N. Nadtochy and C. Schmitt
   Phys. Lett. B **803** 135297 (2020).

2. Asymmetric fission around lead: The case of ^{198}Po
   Shilpi Gupta, C. Schmitt, K. Mahata, A. Shrivastava, P. Sugathan, A. Jhingan, K.S Golda, N. Saneesh, M. Kumar, G. Kaur, L. Stuttge, D. Arora, H. Arora, A. Chatterjee, K. Chauhan, S.K Duggi, D.P. Kaur, V. Mishra, Prashant N. Patil and K. Rani
   Phys. Rev. C **100**, 064608 (2019).

3. Evidence for the general dominance of proton shells in low-energy fission
   K. Mahata, C. Schmitt, **Shilpi Gupta**, A. Shrivastava, G. Scamps and K.-H. Schmidt
   Under review.

Conferences

1. Fission fragment mass distributions from ^{193}Tl,
   Shilpi Gupta, K. Mahata, A. Shrivastava, S.K. Pandit, P.C. Rout, V.V. Parkar, A. Kumar, P. Patale, K. Ramachandran, B.K. Nayak, E.T Mirgule, A. Jhingan
   DAE Symp. on Nucl. Phys. vol. 64, 479 (2019)

2. Fission-fragment mass distribution in neutron-deficient Po at low excitation energy,
Shilpi Gupta, C. Schmitt, A. Shrivastava, K. Mahata, P. Sugathan, A. Jhingan, K. S. Golda, N. Saneesh, A. Chatterjee, G. Kaur, D. Arora, M. Kumar, L. Stuttge, S. K. Duggi, P. N. Patil
International Nuclear Physics Conference Abstract book 258 (2019)

3. Fission-fragment mass distribution in neutron-deficient Po at low excitation energy,
Shilpi Gupta, C. Schmitt, A. Shrivastava, K. Mahata, P. Sugathan, A. Jhingan, K. S. Golda, N. Saneesh, A. Chatterjee, G. Kaur, D. Arora, M. Kumar, L. Stuttge, S. K. Duggi, P. N. Patil
DAE International Symposium on Nucl. Phys. vol. 63, 640 (2018)

4. Fission Fragment mass distribution for ^{16}O+^{175}Lu,
Shilpi Gupta, K. Mahata, A. Shrivastava, K. Ramachandran, V.V. Parkar, S.K. Pandit, P.C. Rout, A. Kumar, P. Patale, T.K Ghosh, A. Sen, B.K Nayak, E.T. Mirgule, A. Saxena, A. Jhingan
DAE Symp. on Nucl. Phys. vol. 62, 378 (2017)

5. Fission Fragment mass distribution for neutron deficient nuclei in A$\sim$200 region,
Shilpi Gupta, A. Shrivastava, K. Mahata, K. Ramachandran, S. K. Pandit, P. C. Rout, V. V. Parkar, G. Mohanto, A. Parihari, A. Kumar, P. Patale, B. K. Nayak, E. T. Mirgule, A. Saxena, A. Jhingan, P. Sugathan
DAE Symp. on Nucl. Phys. vol. 61, 606 (2016)

To

My beloved parents

Urvashi Gupta

&

Subhash Chandra Gupta

ACKNOWLEDGEMENTS

First and foremost, I would like to express my deep and sincere gratitude towards my thesis supervisor, Dr. A. Shrivastava, for being a guiding light in my life both professionally as well as personally since past few years. My sincere thanks and respect also goes to my co-guide Dr. K. Mahata. His rational scientific thinking has been a key factor behind the success of this research work. I am particularly grateful to Dr. Christelle Schmidt for her enlightening discussions throughout the course of this work. Her deep knowledge of fission field guided me to see and appreciate the beauty and complexity of fission process.

I wish to express my sincere thanks to Dr. K. Ramachandran for his numerous help at various stages of this journey. I am extremely thankful to Dr. S. K. Pandit and Dr. V. V. Parkar for several fruitful discussions and their critical reading of the manuscripts and the thesis. I must also thank Dr. E. T. Mirgule and Dr. P. C. Rout for their constant support and encouragement. I am thankful to Mr. A. Kumar for his valuable support during this research work.

I would like to express my deepest appreciation to the members of my doctoral committee Dr. B. K. Nayak, Dr. Alok Saxena, Dr. Chandana Bhattacharya and Dr. R. Tripathi for their critical assessment and suggestions during the progress review and pre-synopsis viva-voce.

I express my heartfelt thanks to Dr. S. Kailas and Dr. A. Navin for their invaluable suggestions at different stages of this work. Special thanks to Dr. V. Nanal for providing extensive experimental support throughout this research work. I am extremely thankful to Dr. A. Chatterjee for his fruitful discussions, suggestions and extended support in data acquisition at IUAC delhi. Also, I gratefully acknowledge the enormous help and assistance provided by Dr. P. Sugathan, Dr. Akhil Jhingan, Dr. K. S. Golda and Dr. N. Saneesh during our experiment at IUAC.

I am extremely thankful to Dr. A. K. Nasirov and Dr. G.A. Yuldasheva for providing DNS model calculations and Dr. P.N. Nadtochy for providing 4D Langevin dynamical model calculations used in this work. Also, I must thank Dr. Louise Stuttge for a successful collaboration.

I am thankful to Mr. P. Patale and Mr. R. Kujur for their immense help and assistance during the experiments. The help of the NPD and HBNI office staff and each and every member of NPD during this period is heartily acknowledged.

I am grateful to technical staff of the Pelletron-Linac facility Mumbai and technical staff of IUAC Delhi for smooth running of the machine during the experiments.

I am thankful for the joyful company of my friends Sangeeta Dhuri, Dr. Anamika Parihari, Chavi Joshi, Ananya Kundu and Dipayan Chattopadhyay, Kavita Chauhan during my PhD journey. I must thank Harisree for her ample help at various stages. I must thank Dr. Yogesh Sawant, Mr. Raman Gandhi, Mr. G. K. Prajapati and Mr. L. S. Dhanu for their cheerful accompany during this work.

Words are insufficient for me to express my deep gratitude towards my M.Sc nuclear physics professor Dr. V. K. Tiwari Sir. His insightful teaching motivated me to appreciate the beauty of quantum mechanics and nuclear physics. I am extremely thankful to my school teachers specifically S. K. Upadhyay Sir for believing in me and always encouraging me to do the best. Many thanks to my school and college friends, Shraddha, Momi, Shweta, Malvika and Anoop for always being with me.

Last but definitely not the least, I thank God for blessing me with so much loving, caring and always supporting family. I must thank my stress busters, my nieces (Shubhi, Shruti and Yati) for their unconditional love. Finally, I wish to thank my parents for their endless love and encouragement, without whom I would have been nothing.

Shilpi

Shilpi Gupta

CONTENTS

Homi Bhabha National Institute

Ph. D. PROGRAMME

1.	**Name of the Student:**	Shilpi Gupta
2.	**Name of the Constituent Institution:**	Bhabha Atomic Research Centre
3.	**Enrolment No. :**	PHYS01201404018
4.	**Title of the Thesis:**	Shell effects in fission fragment mass distribution of neutron defficient nuclei in A$\sim$200 region
5.	**Board of Studies:**	Physical Sciences

SYNOPSIS

Nuclear fission is a complex process that results in the splitting of a single nucleus into two or more lighter nuclei. Reliable knowledge of this process is important not only for the fundamental research like nuclear physics and astrophysics but also for the applications in nuclear energy, production of isotopes for medical and industrial purposes and safeguards [1, 2].

Soon after its recognition by Meitner and Frisch [4], Bohr and Wheeler explained nuclear fission using liquid drop model (LDM) [5]. In this macroscopic approach, nucleus is considered as a drop of homogeneously charged liquid. A slight deformation in such a charged drop can result in competition between attractive surface energy and coulomb repulsive energy. As the deformation of the nucleus continues to increase, the sum of decreasing coulomb energy and slowly increasing surface energy produces a barrier in potential energy surface (PES). The top of this barrier is called saddle point and the minimum amount of energy required by a nucleus in ground state to reach the saddle point is called fission barrier (B_f). According to LDM, the path leading to minimum potential energy for the two separated fragments pass through symmetric mass split. Hence the predicted fission fragment mass distribution (FFMD) is always symmetric, independent of the fissioning compound nucleus (CN). Although this simplified model could explain various fission observable like fission probability and its variation with excitation energy, it failed to explain predominantly asymmetric FFMD observed in low energy fission of actinides. Clearly this failure was consequence of not taking into account the single particle (microscopic) effects. Realizing the need for inclusion of quantum nature of nucleus for describing fission process, Strutinsky in 1967 first suggested a means of combining the macroscopic and microscopic contribution to the binding energy by assuming quantum effects as small deviation from a uniform distribution in energy levels, assumed in LDM [5]. In this shell correction incorporated liquid drop model, as the coulomb energy and surface energy changes with comparable magnitude (with increase in deformation), the residual interaction term (which is comparatively very small from coulomb energy and surface energy) largely affects the potential energy landscape by creating wiggles in the surface. These multiple valleys/dips in the PES allows the possibility of multiple fission modes for a given CN.

In the initial days of nuclear fission studies, the data were obtained using fission induced by light projectiles like neutron, proton, gamma rays or the spontaneous fission of heavy nuclei. A systematic study of these data indicated that, with increasing mass of the fissioning nucleus, the mass of the heavier fission fragment (FF) remained stable (A$\sim$140) while that of the lighter fragment increased. This stability of the heavier fragment mass was conjectured to be made of two distinct contributions: the so-called S1 mode located at $A_H \approx 134$ and ascribed to the neutron $N_H=82$ spherical shell, and the S2 mode at $A_H \approx 144$ due to a $N_H \approx 88$ deformed shell [2, 9]. The sudden transition from asymmetric to symmetric fission for nuclei around Fm (Z=100) further supported this interpretation. For almost two decades, this understanding of fission process, remained irrefutable. In the beginning of current century, new generation advanced detection and measurement systems made it possible to measure FFs mass as well as charge distribution of several nuclei, with very good precision, which were previously unavailable in conventional fission experiments. In their pioneering work, Schmidt et.al. [8] reported FFs charge distribution for 70 short lived radioactive nuclei between astatine and uranium. An elaborate study of all these fissioning nucleus unfolded the fact that under the broad peak of constant A, it is actually the constant Z of the heavier fragment, which is stable at Z≈52 and 55 [9]. These values of Z of the heavier fragment are not preferred either from spherical or from deformed shell consideration in N or Z. Further experiments performed to measure FFs mass and charge distribution with good precision using other advanced techniques, supported the results [10, 11]. The origin of this favored Z split is still under debate [12, 13].

Another unexpected observation was reported by Andreyev *et.al.* in 2010 [18] where they measured FFs mass and TKE distribution for ^{180}Hg populated in β decay of ^{180}Tl. According to above mentioned shell correction incorporated liquid drop model, ^{180}Hg is expected to fission symmetrically in two semi-magic ^{90}Zr nuclei having close neutron shell of N=50. Contrary to this expectation, the very low energy fission of ^{180}Hg was observed to be highly asymmetric with lighter and heavier fragment mass peaks at 79 and 101. Later, observation of multi-modal fission for ^{194,196}Po and ^{202}Rn opened a whole “new" (pre-actinide) region of asymmetric fission to be investigated.

These observations triggered several theoretical groups to perform calculations in the sub lead region. However they were based on very different approaches, hence created confusion in understanding the actual mechanism behind the splitting of fissioning nucleus in terms of A and Z. More experimental information is nevertheless mandatory to get a clear picture.

Motivated by this requirement, in the present thesis work, we carried out measurements of FF mass and TKE distribution for compound nucleus ^{191}Au and ^{198}Po using heavy ion induced fusion fission reaction. In the first case, by populating ^{191}Au via two very different entrance channels, presence of quasifission has been investigated in order to disentangle the role of entrance channel dynamics versus shell effects in FFs. For later case of ^{198}Po, FF mass distribution is measured to study the evolution of asymmetric and symmetric components as a function of N and Z of the fissioning system. The element polonium (Z=84) is situated ideally mid-way between mercury (Z = 80) and traditional actinides (Z$\geq$ 88), over which fragment properties are observed to change fast [14]. Furthermore, a consistent analysis of the experimental information collected so far on asymmetric fragmentation in low-energy fission of neutron-deficient nuclei around lead is performed to get a unified picture of fission process. The details of the work executed are described below.

1. Investigation of entrance channel effect on asymmetric fission

Although the low excitation energy required for studying asymmetric fission of pre-actinides can be ideally reached in β delayed and electromagnetic-induced fission, the number of systems accessible to these approaches is limited in practice. In such a scenario, heavy-ion induced fusion-fission is the only alternative way to study FF mass distribution. This method is useful to study nuclear fission not only as a function of compound nucleus N/Z (N=number of neutrons, Z=number of protons of the fissioning nucleus) but as a function of compound nucleus excitation energy (E*) as well. However, as the heavy beam brings in higher excitation energy and angular momentum (l), it opens the possibility of quasifission [15]. The quasifission, is a non-compound (non-equilibrated) nuclear process which depends strongly on the entrance channel parameters like charge product (or mass asymmetry), deformation of the colliding nuclei, shell closure and neutron excess in addition to the CN fissility [15]. The mass of reaction products coming from this non-equilibrated process can severely overlap with the mass of fragments originating from complete fusion fission. Hence, quasifission can mimic the presence of multi-modal CN fission. Investigation of the role of quasifission is essential for an accurate modelling of the excitation energy dependence of microscopic effects. Ignoring this aspect might lead to ambiguity in the inferred multi-modal fission in pre-actinide region. Till now, mass-asymmetric fission and its evolution with excitation energy in neutron deficient sub-lead nuclei, viz. ^{179,189}Au, ^{180,182,190}Hg and ^{178}Pt have been studied using beams of ^{12}C, ^{35}Cl, ^{36}Ar and ^{40}Ca, respectively. In pre-actinide region, evidence of quasifission has been found in ^{202}Po (Z = 84), formed in ^{34}S+ ^{168}Er reaction having target projectile charge product (Z_pZ_t) as low as 1088. However, the quassifission was considered to be negligible and its exact nature and extent was not investigated in the heavy-ion induced reactions used to study the presence of asymmetric fission in nuclei with Z≤80, having Z_pZ_t in the range 1054 to 1200.

We have investigated the possible presence of quasifission in pre-actinide region by measuring FF mass distributions of ^{191}Au, formed via two different entrance channels, viz. ^{16}O+^{175}Lu and ^{37}Cl+^{154}Sm reactions [32]. Both the experiments were performed at BARC-TIFR Pelletron-Linac Facility, Mumbai using pulsed beams of ^{16}O and ^{37}Cl on a 280μg/cm^2 thick ^{175}Lu (97.41% enriched) target having 150μg/cm^2 thick Al backing and a 200μg/cm^2 thick ^{154}Sm (>99% enriched) target with 550μg/cm^2 thick Al backing, respectively. Fission fragments time-of-flights (TOF) with respect to the arrival of the beam pulse, positions(x,y) and energy losses were recorded using two large area (12.5×7.5 cm^2) position sensitive multiwire proportional counters (MWPCs) kept at folding angles, at a distance of 24 cm from the target, covering an angular range of 30^0 each. The detected fragment velocity vectors were calculated from the time of flight (TOF) and position information. The fission events were selected by putting two dimensional gates in the TOF difference verses energy loss spectra and the fragment mass distributions were deduced using the TOF difference method [16]. Small corrections in the fragment mass due to their energy loss in the target and backing were obtained in an iterative manner on event by event basis. A detailed comparison of the obtained FFs mass distribution and its widths (σ) for two different entrance channels have been performed using semi-empirical code GEF (GEneral description of Fission observables), 4D Langevin dynamical model and statistical relation for σ (as function of CN temperature T and $\langle l^2 \rangle$) respectively. The Dinuclear System (DNS) model calculation have also been performed to see the possible presence and estimation of non-compound events. The results provide conclusive evidence indicating substantial presence of quasifission in the sub-Pb region. The mass of fragments originating from compound nuclear fission are found to considerably overlap with the mass of fragments coming from quasifission reaction. The present measurement along with a systematic analysis of the available experimental data present so far, shows that there is a significant presence of quasifission in the reactions involving heavier projectiles (Z$\geq$17) with spherical as well as deformed targets used to investigate fission of neutron deficient nuclei in pre-actinide region.

2. Multimodal fission at the center of pre-actinide region

To explore the pre-actinide region beyond Hg (Z>80), we measured FF mass and TKE distributions of ^{198}Po [33]. We selected ^{198}Po, as it is ideally situated mid-way between Hg and actinides. It is thus a priori particularly suited to search for a connection between pre-actinide and actinide asymmetric fission. The mass distribution, highly asymmetric for ^{178,180}Hg, evolves towards a dominantly symmetric component in ^{202}Rn through a triple-humped distribution for ^{194,196}Po. Information on isotope A = 198 permits to proceed further along the polonium chain and to map out the balance between asymmetric and symmetric splitting as a function of fissioning system N and Z. The compound nucleus ^{198}Po was formed by bombarding a 200 μg/cm^2 thick isotopically-enriched (83.2%) ^{170}Yb target, evaporated onto 22 μg/cm^2 thick C backing, with a ^{28}Si beam of energies 119, 122 and 130 MeV. This experiment was performed at the 15UD Pelletron LINAC accelerator facility of IUAC, New Delhi. Applying the same data acquisition and analysis procedure as mentioned above, the deduced FFs mass and TKE distributions were analyzed to see for possible presence of multi-modal fission. Comparison with the data showed that a good description can be achieved by the GEF code for representative measurements in this region. The calculation was then used to trace back the fission properties of ^{198}Po close to threshold.

3. Systematic trend: evolution of fragment properties

Most advanced theories proposed to explain the results around Hg seems to agree about a common origin (i.e. shell effects in FFs) of asymmetric splitting in the pre-actinide and actinide region but the underlying mechanism is not clear. In this thesis work, a consistent analysis of the experimental results collected so far on low energy fission is performed. In case of pre-actinides, a regular pattern has emerged revealing the leading role played by the proton number of the lighter fragment. It is observed that as proton number of the fissioning nuclei increases the number of protons in the lighter fragment remained stable with Z≈36, while that of the heavier fragment increased. This observation is in striking connection with the pattern observed in the actinide region, where proton number in the heavier fragment remains stable (as discussed earlier). A unified picture is seen to explain the fragment properties all the way from pre-actinides to actinides. Lastly, GEF predictions have been used to study the evolution of fragment mass distribution over a wide domain, pointing towards the necessary theoretical effort regarding dynamical transition from a fissioning system to a fragment driven process.

The thesis is organized into seven chapters. In chapter 1, the importance of understanding fission process and its study in pre-actinide region has been discussed. Current status of the field and motivation of the present thesis work is described. Chapter 2 contains a brief description of various theoretical models proposed to explain fission in pre-actinide region. Chapter 3 contains the details of present experimental setup and data acquisition system along with a brief description of the Pelletron Linac Facility. The analysis method to separate fission events and deduction of fragment mass and TKE are discussed. Corrections in the fragment mass due to their energy loss in the target and backing on event by event basis is also explained. The results of measurement of FFs mass distribution from ^{191}Au as well as its comparison with various theoretical model prediction is given in chapter 4. Measurement of mass and TKE distribution for ^{28}Si+^{170}Yb forming ^{198}Po is provided in Chapter 5. Chapter 6 contains a systematic study of all available MD measurements for low energy fission in actinide and pre-actinide region, to better understand the process of nuclear fission and get a unified picture. Lastly, the summary of the thesis and future scope of the work are highlighted in Chapter 7.

Bibliography

[1] A.N. Andreyev, *et. al.*, Rep. Prog. Phys. 81 016301 (2018), and references therein.

[2] K.-H. Schmidt, B. Jurado, Rep. Prog. Phys. **81** 106301 (2018), and references therein.

[4] L. Meitner, O. R. Frisch, Nature **143**, 239 (1939).

[5] N. Bohr, J.R. Wheeler, Phys. Rev. **56**, 426 (1939).

[5] V. M. Strutinsky , Nucl. Phys. A **95**, 420-442 (1967)

[9] B. D. Wilkins *et. al.*, Phys. Rev. C **14**, 1832 (1976).

[18] A. N. Andreyev *et. al.*, Phys. Rev. Lett **105**, 252502 (2010).

[8] K.-H. Schmidt *et. al.*, Nucl. Phys. A **665**, 221 (2000).

[9] C. Bockstiegel *et. al.*, International Journal of Modern Physics E **18**, 873 (2009).

[10] Pellereau *et. al.*, Phys.Rev. C **95**, 054603 (2017).

[11] D. Ramos *et. al.*, Phys.Rev. C **99**, 024615 (2019).

[12] G. Scamps and C. Simenell, Nature (London) **564**, 382 (2018).

[13] T. Ichikawa and P. Moller, Phys. Lett. B **789**, 679 (2019).

[14] L. Ghys *et. al.*, Phys. Rev. C **90**, 041301 (2014).

[15] R. Du Rietz *et. al.*, Phys. Rev. C **88**, 054618 (2013)

[16] R.K Choudhury *et. al.*, Phys. Rev. C **60**, 054609 (1999).

[32] Shilpi Gupta *et. al.*, Phys. Lett. B **803**, 135297 (2020).

[33] Shilpi Gupta *et. al.*, Phys. Rev. C **100**, 064608 (2019).

List of Figures

List of Tables

1

Introduction

1.1 Preamble

Nuclear fission is a complex process where a single nucleus splits into two or more heavy nuclei, releasing a large amount of energy. This mechanism of nuclear splitting not only offers a rich laboratory for research on nuclear properties, its detailed knowledge is crucial for applications like nuclear energy and medicine [1, 2].

Although nuclear fission is a large scale collective phenomena, this process is primarily governed by a delicate interplay of the macroscopic (liquid drop) and the microscopic (single particle) effects, whose accurate modelling is still a challenge for nuclear theory. In this scenario, experimental determination of different observable quantities associated with this process, for example final fragment masses, their total kinetic energies, angular distribution etc. are of fundamental importance for nuclear physics. Among these observables, fission fragment mass distribution is an efficient tool to probe structure effects and dynamics associated with the process.

Earlier, from an extensive set of experimental measurements and theoretical studies of several nuclei in the *actinide* region, it was concluded that the shell effects in the fragments are playing the decisive role for final mass split. Hence, these shell effects are main cause of asymmetric fission whenever observed.

In recent times, the study of fission fragment mass distribution in $pre-actinide$ region has received much attention. A "new type of asymmetric fission" has been identified in this region. It began with the unexpected observation of asymmetric mass split in β-delayed fission of ^{180}Tl at ISOLDE CERN [18]. If the understanding of fission process gained in "old" actinide region is extrapolated for nuclei in pre-actinide region, ^{180}Hg is expected to fission symmetrically into two semi-magic ^{90}Zr nuclei. However, the experimental fission fragment mass distribution of ^{180}Hg formed at very low excitation energy ($\sim$1 MeV) above fission barrier, were found to peak at fragment mass of 80 and 100. Several state of the art theories were proposed to explain this result. Having different approaches, these theories gave very contradictory interpretation of the fission process, regarding role of shell effects at saddle or scission and nuclear dynamics [17, 24, 27, 28]. A brief review of theoretical and experimental developments in the process of understanding nuclear fission, using fission fragment mass distribution is given in next section.

1.2 A classical description of nuclear fission

The process of nuclear fission remains as a puzzle in the field of nuclear physics since last 80 years. Soon after its discovery by Otto Hahn and Fritz Strassman in 1938 [3, 4], liquid drop model (LDM) was proposed by Bohr and Wheeler to explain this process [5]. In this macroscopic approach, nucleus is considered as homogeneously charged, in-compressible liquid drop held together by the nuclear forces. Analyzing the energetics of such a drop lead Weizsacker and Bethe [6] to semi-empirical mass formula, which describes the binding energy of a nucleus in terms of its volume, surface, Coulomb, symmetry and pairing energy as,

$$B_{\mathrm{LDM}}(N,Z) = a_{\mathrm{v}}A - a_{\mathrm{s}}A^{2/3} - a_{\mathrm{c}}\frac{Z(Z-1)}{A^{1/3}} - a_{\mathrm{A}}\frac{(N-Z)^2}{A} + a_{\mathrm{p}}\frac{(-1)^N + (-1)^Z}{2A^{3/4}} \tag{1.1}$$

As the nucleus gets more and more deformed, the deformation dependent attractive surface energy and repulsive Coulomb energy changes with comparable magnitude, creating a barrier in potential energy surface. A liquid drop potential energy surface for a nucleus as a function of elongation is shown in Fig. 1.1 as blue dashed line. The minimum amount of energy required by the nucleus in ground state to reach maxima of potential energy surface (saddle point) is called fission barrier B_f^{mac}.

Considering small axially symmetric distortion in a spherical nucleus, its radius can be written as

$$R(\theta) = R_0[1 + \alpha_2 P_2 \mathrm{Cos}(\theta)] \tag{1.2}$$

where θ is angle of radius vector with respect to the body fixed frame of the fissioning nucleus, R_0 is the radius of undistorted sphere and α_2 is a parameter describing the amount of quadrupole distortion. Higher order terms are neglected in above equation as they are inconsequential for small distortions. The surface

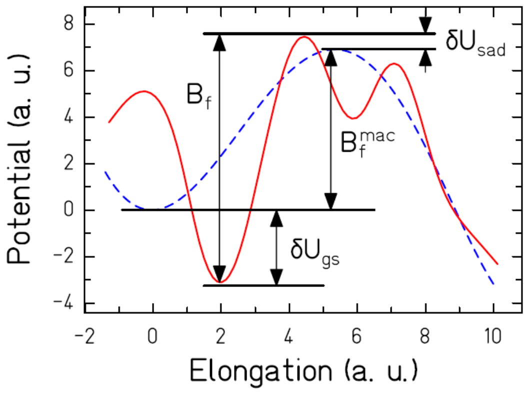

Figure 1.1: Macroscopic and microscopic potential energy for a heavy nuclei as a function of elongation as described in Ref. [2].

and Coulomb energies for small distortion are given by

$$E_s = E_{s0}[1 + \frac{2}{5}{\alpha_2}^2] \tag{1.3}$$

$$E_c = E_{c0}[1 - \frac{1}{5}{\alpha_2}^2] \tag{1.4}$$

where E_{s0} and E_{c0} are surface and Coulomb energies of undistorted sphere respectively. According to Bohr and Wheeler prescription [5], when the fissility defined as $\chi = \Delta\mathrm{E_c}/\Delta\mathrm{E_s}$ is less than 1, i.e till the decrease in Coulomb energy($\Delta\mathrm{E_c} = \frac{1}{5}{\alpha_2}^2 E_{c0}$) is smaller than increase in surface energy($\Delta\mathrm{E_s} = \frac{2}{5}{\alpha_2}^2 E_{s0}$), a deformed nucleus do not undergo fission. The nucleus becomes critically unstable as soon as χ shifts to 1, for $\chi>1$ there will be no potential energy barrier and the nucleus will split into two fragments, instantaneously.

1.3 Fission fragment mass distribution: Symmetric or Asymmetric?

Fragment mass distribution predicted according to LDM consideration is always symmetric. However, spontaneous and light ion induced fission fragment mass distribution studied soon after discovery of fission showed that most of nuclei in actinide region fissions preferentially into two asymmetric fragments. Later, due to inadequacy of LDM in explaining multiple nuclear properties like extra stability of magic nuclei, excited states of a nucleus etc., single particle model (shell model) was proposed. This model assumes that each nucleon moves in a potential well that is an approximate representation of the interaction of that nucleon with all the other nucleons. Shell model approach was very successful in explaining the nuclear properties, still calculating fission barrier by only using this microscopic approach was not possible. The associated errors in calculating Coulomb and surface energy microscopically can many times lead to large uncertainty in the fission barrier calculation. Strutinsky in the year 1967 first suggested a means of combining the macroscopic (LDM) and microscopic (shell model) contribution to calculate the binding energy [7] by assuming quantum effects as small deviation from a uniform distribution in energy levels, assumed in LDM. The total binding energy is then written as

$$B(N,Z) = B_{\mathrm{LDM}}(N,Z) + \sum_{n,p}(\delta\mathrm{U} + \mathrm{P}) \tag{1.5}$$

where

$$\delta\mathrm{U} = \mathrm{U} - \tilde{\mathrm{U}} \tag{1.6}$$

is the deviation measured as difference between energy in "shell" quantal distribution $\mathrm{U} = \sum_v \mathrm{E}_v 2n_v$ and energy in uniform distribution $\tilde{\mathrm{U}} = 2\int_{-\infty}^{\tilde{\lambda}} \mathrm{E}\tilde{\mathrm{g}}(\mathrm{E})d\mathrm{E}$ of nucleon states. Here, E_v and n_v are the energy and occupation number of the v^{th} shell respectively calculated in an average potential (shell model) and $\tilde{\mathrm{g}}$ is the uniform distribution of nucleon states (LDM) with chemical potential $\tilde{\lambda}$. In the residual interaction term P, pairing energy mainly contributes because unlike other interaction, it carries strong exponential dependence on density of nucleon states. This shell correction incorporated LDM prediction of potential energy shown as red continuous line in Fig. 1.1 was able to explain asymmetric fission fragment mass distribution observed in actinide region quite well. As the microscopic shell effects which depends strongly on proton and neutron numbers can result in complex potential energy surfaces, where multiple asymmetric or symmetric valleys can be present. It is due to these various probable paths (valleys), a nucleus can have multiple fission modes.

A while later around 1972, systematic study of fission fragment mass distribution as a function of the mass of the fissioning nucleus, shown in Fig. 1.2 [8] reveals that as the mass of the fissioning nucleus increases, the mass of the heavier fragment remained approximately fixed (A $\sim$ 140) while the mass of the lighter fragment increased. This result was interpreted in terms of shell effect in the heavy fragment. It was concluded that as the closed shell structure energetically favour the formation of doubly magic nuclei ($^{132}_{50}\mathrm{Sn}_{82}$) and at scission there is deformation dependent shell correction for N=88, these two effects combinely drives the formation of heavier fragment with mass A$\sim$140 [9]. The sudden transition from asymmetric to symmetric fission for nuclei around Fm (Z=100) further supported this interpretation. For almost two decades, this understanding of fission process remained irrefutable. In the beginning of current century, new generation advanced detection and measurement techniques made it possible to measure fission fragment mass as well as charge distribution of several nuclei, which were previously unavailable in conventional fission experiment, with very good precision. In their pioneering work Schmidt *et al* [10] reported fission fragment charge distribution for 70 short lived radioactive nuclei between astatine and uranium. In this work, relativistic secondary projectile beam was produced by fragmentation of primary 1 A GeV ^{238}U beam and each of this secondary projectile was then identified in its nuclear charge and mass numbers. When these secondary projectiles were made to interact with high Z (^{208}Pb in this case) secondary target, the giant resonance, mostly the giant dipole resonances were excited by electromagnetic interaction and fission from excitation energy around 11 MeV was induced. An elaborate study of all these fissioning nuclei unfolded the fact that under the broad peak of constant A, it is actually the constant Z of the heavier fragment, which is stable at Z=52 and Z=55 [11, 12]. These values of Z of the heavier fragment is not preferred either from spherical or from known deformed shell consideration in N or Z. Further experiments performed to measure fission fragment mass and charge with good precision using other advanced techniques, supported the results [13, 14, 15]. The origin of this favoured Z split is still under debate [16, 17].

Another unanticipated result was observed by Andreyev *et al* [18] after measuring fission fragment mass distribution of ^{180}Hg. In this benchmark work, the novel method of β-delayed fission was applied to study fission. The β-delayed fission is a two step nuclear process where, parent nucleus undergoes β decay (by

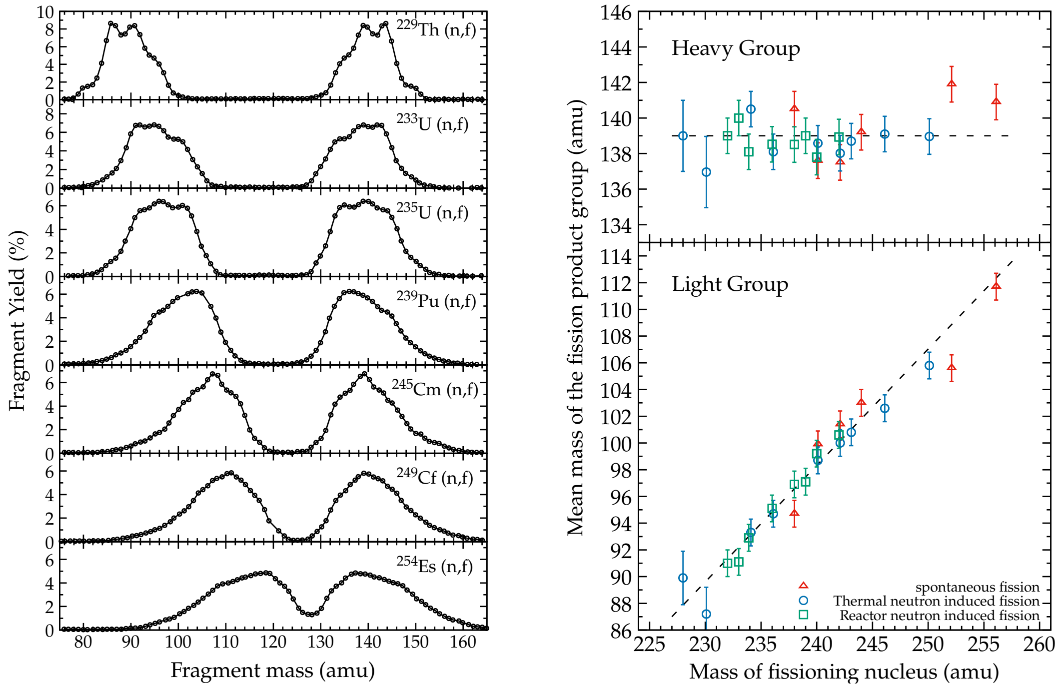

Figure 1.2: (Left) Fission fragment mass distribution from Z=90 to Z=99 [19] (Right) Average mass of heavy and light fragment as a function of mass of the fissioning nucleus [8].

electron capture in this case as ^{180}Tl is neutron deficient), producing a daughter nucleus in excited state with maximum possible energy equal to associated Q value of the reaction, followed by subsequent fission of the daughter nucleus if resulting excitation energy is greater than its fission barrier B_f. Till now only β-delayed fission give access to most exotic cases of very low energy fission studies of nuclei which are far away from line of stability in the nuclear chart as they are not accessible by any other technique. This experiment, was particularly unique, as for the first time β-delayed fission experiment in Pb region was done using combination of ISOLDE (Isotope mass Separator On-Line facility) and RILIS (Resonance Ionization LASER Ion Source), to achieve an unambiguous isotopic selection of the precursor element. In this experiment, a 1.4 GeV proton beam impinging on a thick (50 g/cm^2) ^{238}U target, produced a variety of reaction products via spallation, fragmentation and fission reactions. Among the neutral reaction products diffused in the subsequently placed hot cavity, thallium atoms were selectively ionized to a 1^+ charge state by two overlapping precisely tuned and synchronized laser beams. These ionized thallium ions were then extracted by the high-voltage potential of 30 kV, followed by ISOLDE mass separator for specific selection of A=180. This pure beam of ^{180}Tl was then deposited on a thin C foil. The coincidence fission fragments were then detected using two Si detectors kept on both sides of the foil. These detectors were properly calibrated for TKE and mass measurement after correction for pulse height defect in the detector [20, 21]. The mass and total kinetic energy (TKE) spectrum of observed coincident fission fragments are shown in Fig. 1.3.

As discussed earlier, from an extensive study in actinide region it was concluded that the asymmetric low energy fission is primarily derived from fragment shell stabilization of ^{132}Sn. A set of data from Ref. [10] demonstrated the transition from mostly asymmetric fission in the actinides towards symmetric fission as the dominant mode in the light thorium to astatine region. Other studies by Itkis *et al* [22] in the mass region A$\sim$185-215 supported this result of symmetric fission in sub-Pb region. These observations outlined a trend from which it was anticipated that ^{180}Hg will undergo symmetric fission populating two semi-magic ^{90}Zr nuclei. However, the observed mass distribution was found to be highly asymmetric with heavier and lighter mass peaks centred around A_H=100(1) and A_L=80(1). The observed narrow width of the heavier and lighter mass groups (4.0(3) amu), producing high peak to valley ratio made the result distinctively different from the expectation. Also, a single-peaked and narrow Gaussian-like TKE distribution confirmed that a single fission mode is dominating in ^{180}Hg. The corresponding most probable Z values obtained for these masses, under unchanged charge density (UCD) assumption are Z_H=44(2) and Z_L=36(2), respectively. The authors of this

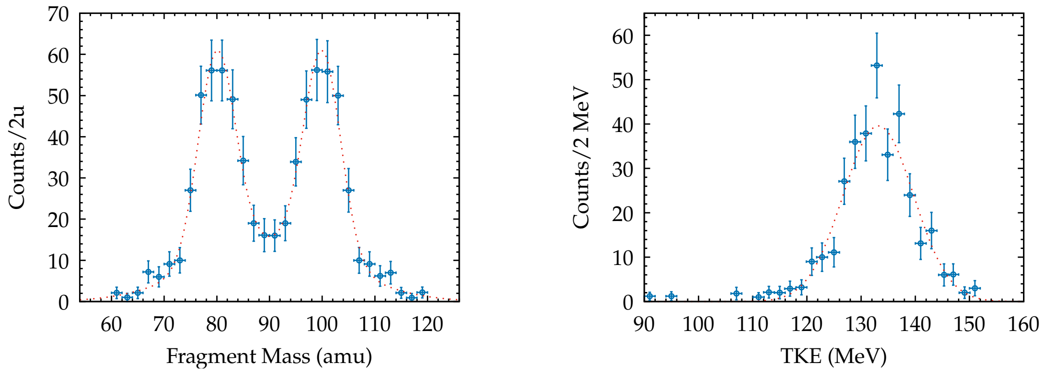

Figure 1.3: (Left) The derived fission-fragment mass and (Right)total kinetic energy distribution of ^{180}Hg [18].

work then tried to understand the fission process and interpret the result using multidimensional fission potential-energy surface calculation based on five independent shape parameters [23]. These parameters are namely, elongation (along fission direction), mass asymmetry $(A_H\text{-}A_L)/(A_H+A_L)$, left and right fragment deformation and neck radius. The structure of the surfaces obtained for ^{180}Hg and ^{236}U by applying immersion method [24] is shown in Fig. 1.4. calculations indicated that the only saddle present in ^{180}Tl is at 0.63 MeV below the Q value of electron capture, i.e below maximum available excitation energy, leads to mass asymmetric valley. Although there is a deeper mass symmetric valley, separated from mass asymmetric valley by a ridge, but the entrance to this valley lies at much

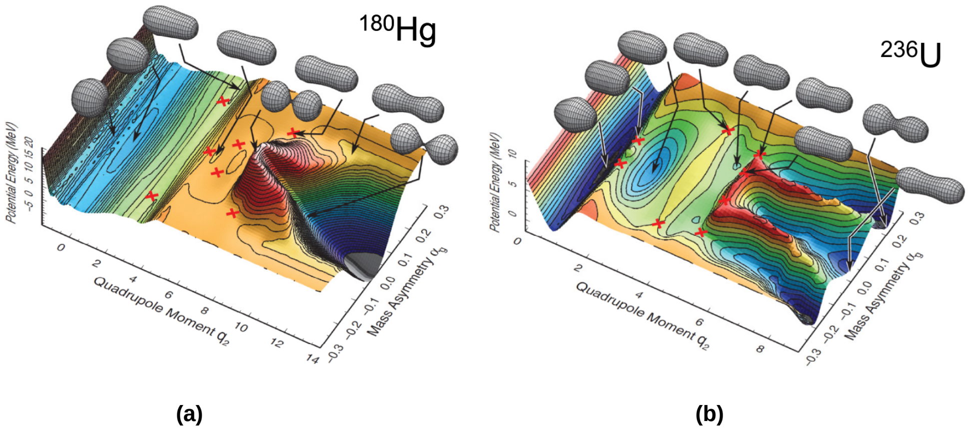

Figure 1.4: Potential-energy surface for ^{180}Hg and ^{236}U in two dimensions (elongation and asymmetry) resulting from a five-dimensional analysis as described in Ref. [18]. The shapes of the fissioning nucleus at various deformations are shown and connected by arrows to their locations on PES.

higher excitation energy. It was observed that, unlike ^{236}U where strong shell corrections persists up to very long deformations, there is *only* symmetric valley at higher elongations in case of ^{180}Hg. When the ridge disappears, one might expect the fission of ^{180}Hg to go through symmetric path. However, at such large elongations, the neck radius might be so small that it restricts further mass flow and the mass asymmetry is frozen. It was concluded that observed mass asymmetry in this mass region is due to shell effects around the saddle point and not due to those of the final fragments [17]. Later, βDF measurements of ^{194,196}At and ^{202}Fr found to exhibit multimodal nature, revealing the presence of both symmetric and asymmetric mode of fragment mass split simultaneously.

These observations triggered several other theoretical groups also to perform calculations in sub lead region, that are based on very different approaches.

The fully self-consistent models, which aims to describe the fission process in a quantum-mechanical framework under the influence of an effective nuclear force, correlate the observed mass asymmetries to the shell structure of pre-scission configurations and associated it with molecular structures [25, 26]. This model also predict a relatively flat potential energy surface (PES) at larger deformation to explain the observed multimodal fission in some of the nuclei in this region. Scission point model, which strive to explain the result assuming that statistical equilibrium is established at scission, could also explain the results [27, 28]. Deformation dependent shell effects in the final fragments are also studied to explain the observed mass distributions in this region. A recent time dependent microscopic study, showing the impact of pear-shaped fission fragments in the mass-asymmetric fission in actinides, also speculate the importance of octupole deformation of the fragments in fission [16, 29]. Shortly before scission, when the fragments are connected by a neck, each fragment have a pear shape. This enhances the production of nuclei which can exhibit octupole shapes for no or little cost in energy instead of spherical closed shell nuclei which are hard to deform. In this microscopic calculation, it was conjectured that octupole correlations induced by shell gaps at Z=34 and N=52-56 in fragments are responsible for observed fission fragment mass distributions of preactinide nuclei.

Till now, the neutron-deficient nuclei (N/Z $\sim$ 1.25-1.4) in the region Au - Rn are barely studied experimentally using various fission techniques. In order to test the validity of various theoretical models proposed to explain the observed structures in mass distribution of nuclei in sub lead region, more experimental data is required. The low excitation energy required for studying asymmetric fission of neutron-deficient pre-actinides can be ideally reached in β-delayed and electromagnetic-induced fission. Unfortunately, the number of systems accessible to these approaches are currently limited, and the statistics is usually low. To complement the fission data provided by the low energy β-delayed fission at ISOLDE and Coulex-induced fission at SOFIA(GSI), a worldwide effort is currently invested in the alternative heavy-ion fusion-induced fission approach.

So far, fragment mass distributions for very few systems namely ^{180,190}Hg [55], ^{178}Pt [58], ^{182,195}Hg [57] and ^{179,189}Au [56] have been studied using heavy ion fusion fission approach to get a deeper insight of asymmetric fission around A$\sim$200. In these studies, both ^{180}Hg and ^{190}Hg populated using ^{36}Ar beam on ^{144,154}Sm target showed flat top mass distributions at all measured energies (E^*_{CN} = 33.4 - 70.5 MeV, $E^*_{B_f}$ = 23.9-41.2 MeV) and indicated the presence of microscopic effects even at large excitation energies [55]. The measured mass distributions of ^{182}Hg in ^{40}Ca+^{142}Nd reaction suggested presence of a mass asymmetric component at the lowest energy. However, relatively less neutron deficient ^{195}Hg in ^{13}C induced reaction showed no sign of asymmetric fission [57]. In ^{35}Cl+^{144,154}Sm reactions, the measured mass distribution for ^{179}Au showed similar deviation from a Gaussian shape at the lowest energy as in ^{182}Hg [56] but the deviation in ^{189}Au was found to be much weaker. From the measured correlations of mass and total kinetic energy in ^{36}Ar+^{142}Nd system the presence of multimodal fission in ^{178}Pt has been inferred [58].

A brief discussion of heavy ion reaction mechanism is given in next section.

1.4 Heavy ion reactions

In the collision of two heavy (A $>$ 4) nuclei, as the relative distance continues to decrease, the interacting nuclei starts experiencing a long range repulsive Coulomb force and a short range attractive nuclear force. The competition between these two forces creates a barrier with an energy pocket inside it. This barrier is called fusion barrier (V_b). A nucleus-nucleus potential for the reaction ^{16}O+^{175}Lu, in case of zero angular momentum (l=0), is shown in Fig 1.5.

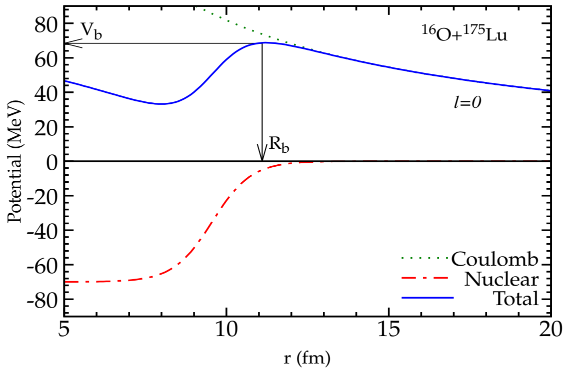

Figure 1.5: Nucleus-nucleus potential for the reaction ^{16}O+^{175}Lu.

For non zero angular momentum, the net potential experienced by the colliding nuclei is given as,

$$V_{total} = V_{Coulomb} + V_{nuclear} + V_{centrifugal} \tag{1.7}$$

when the angular momentum, l, carried by the projectile increases, the barrier height increases and the pocket becomes shallower. Interaction between two heavy ions can result in different nuclear processes depending on quantities like impact parameter (b), relative kinetic energy ($E_{c.m}$), mass of the interacting nuclei etc. For the case of heavy ion collision, where the associated de-Broglie wavelength is much smaller compared to the dimensions involved, the concept of classical trajectory is valid. In this consideration, one can understand the possibility of different nuclear reaction processes in terms of b. Here, impact parameter, b is defined as the perpendicular distance from the centre of the force field to the path of the undeflected projectile. A schematic of different nuclear processes observed in heavy ion collisions as a function of impact parameter is shown in Fig. 1.6.

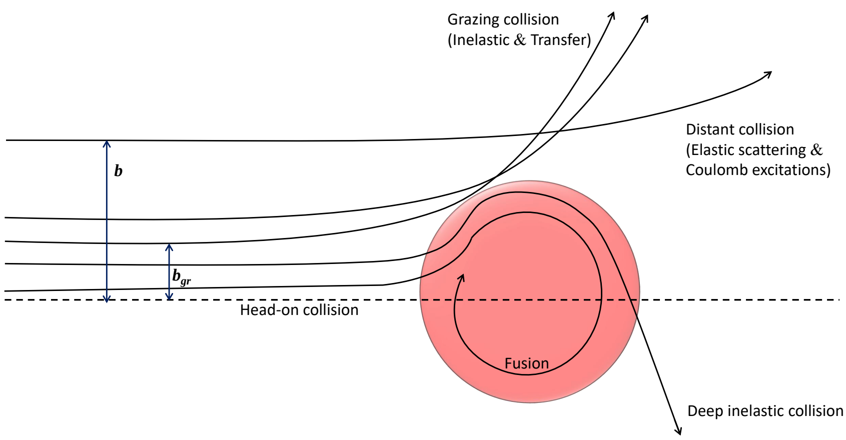

Figure 1.6: Different processes observed in heavy ion collisions as a function of impact parameter.

When the impact parameter is very large (distant collision, $b >$ grazing impact parameter, b_{gr}) or the energy is below the Coulomb barrier, the interaction will take place via Coulomb force only. Most of the incident particle will get elastically scattered, with no change in relative kinetic energy. In case of large impact parameter, there will be loss of flux, only if the reaction partners get excited due to Coulomb repulsion. For the grazing trajectory ($b \sim b_{gr}$), the distance of closest approach become equal to the interaction radius, $R = r_o({A_p}^{1/3} + {A_t}^{1/3})$ and the nuclei start to feel the nuclear force. Here, A_p and A_t are mass number of projectile and target respectively. In this case, direct reactions i.e inelastic excitations or transfer of nucleons starts occurring, where a small fraction of the relative kinetic energy gets converted into internal excitation of the participant nuclei or exchange of small number of nucleons takes place. With further decrease in impact parameter ($b < b_{gr}$) a large amount of energy and angular momentum is transferred from relative motion to intrinsic excitations, still the the collision partners keep their identity up to a net exchange of few nucleons. Such events are known as multi-nucleon transfer and deep inelastic collision (DIC) [30]. In the last possible case, i.e for an approximately head-on collision, the projectile may get completely captured inside the target and form a composite system with charge and mass number Z_p+Z_t and A_p+A_t respectively. If all degrees of freedom get equilibrated in this composite system, a compound nucleus will be formed which may decay via fission. Only these fission events can provide us information about the actual saddle shape of the fissioning nucleus and fusion fission dynamics.

For higher angular momentum, the centrifugal force increases and the depth of potential trap in the nucleus-nucleus interaction becomes shallower. Beyond a certain value of angular momentum (l_{cr}, critical angular momentum), the energy pocket vanishes and the system re-separates immediately after capture, without complete equilibration. Fig 1.7 shows the spin distribution ($d\sigma/dl$) of various reactions as a function of angular momenta.

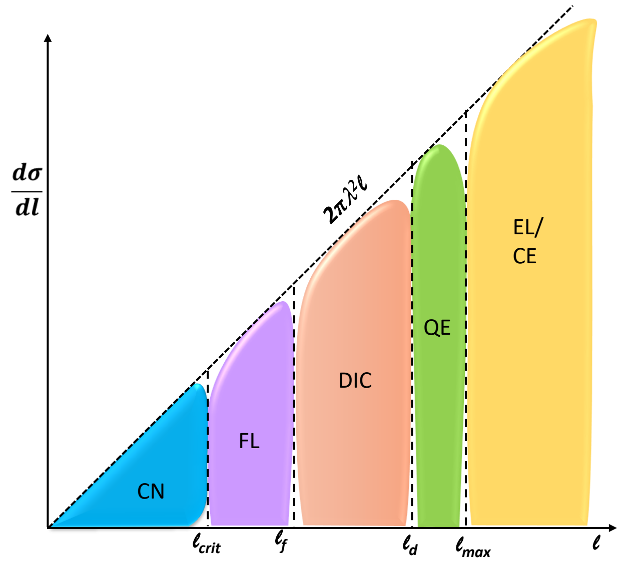

Figure 1.7: l dependence of the partial cross sections for compound nucleus (CN), fission like (FL), deep inelastic collision (DIC), quasielastic collision (QE), elastic collision (EL) and Coulomb excitation (CE) processes.

1.5 Quasifission

Fig. 1.8 illustrate three main categories of dissipative reaction mechanisms in heavy ion induced reactions. The formation of a compound nucleus can be considered as a two step nuclear process. In the first step, the projectile crosses the fusion barrier and combines with the target to form a composite system with total number of protons equal to $Z_p + Z_t$ and total number of neutrons equal to $N_p + N_t$. In second step, the multiple interaction among these nucleons leads to complete equilibration in all degrees of freedom (shape, mass asymmetry, energy etc.), forming a spherical CN that no longer have any memory of its entrance channel. However, if the system reseparates before second step, i.e before complete equilibration, it leads to non-compound nuclear processes called quasifission (QF). In terms of reaction time scale, QF is another dissipative process that bridges the gap between DIC and CN formation. In quasifission processes, after capture of projectile into the target, the composite system do go through considerable transfer of mass along with full relaxation of the relative kinetic energy, but reseparates without complete mass and shape equilibration. The elongated system decay in fission like events before a compact compound nucleus can be formed.

The difference between QF and compound nucleus fission can be understood in terms of potential energy landscape also as shown in Fig. 1.9. In both the cases, the composite system of projectile and target gets trapped behind the conditional saddle point for mass asymmetric entrance channel (orange dash curve, sudden potential for fusion). After this, as the components of this composite system evolves towards symmetry, the potential between them also evolves (blue dash curve, adiabatic potential). As shown in Fig. 1.9(a), this composite system is already inside the true saddle point forming a compact mono-nucleus. If the excitation energy of this CN is more than the fission barrier, the system will further decay into two fission fragments. In case of quasifission the composite system could not form a compact mono-nucleus, as the saddle configuration itself comes out to be too short to keep the system trapped for long and the system breaks into two fission like fragments. There is another similar process to QF called fast fission. This happens at very high energies where the angular momentum dependent fission barrier vanishes and the system formed after capture of projectile into the target soon breaks into fission like fragments.

The process of quasifission is largely effected by entrance channel properties as

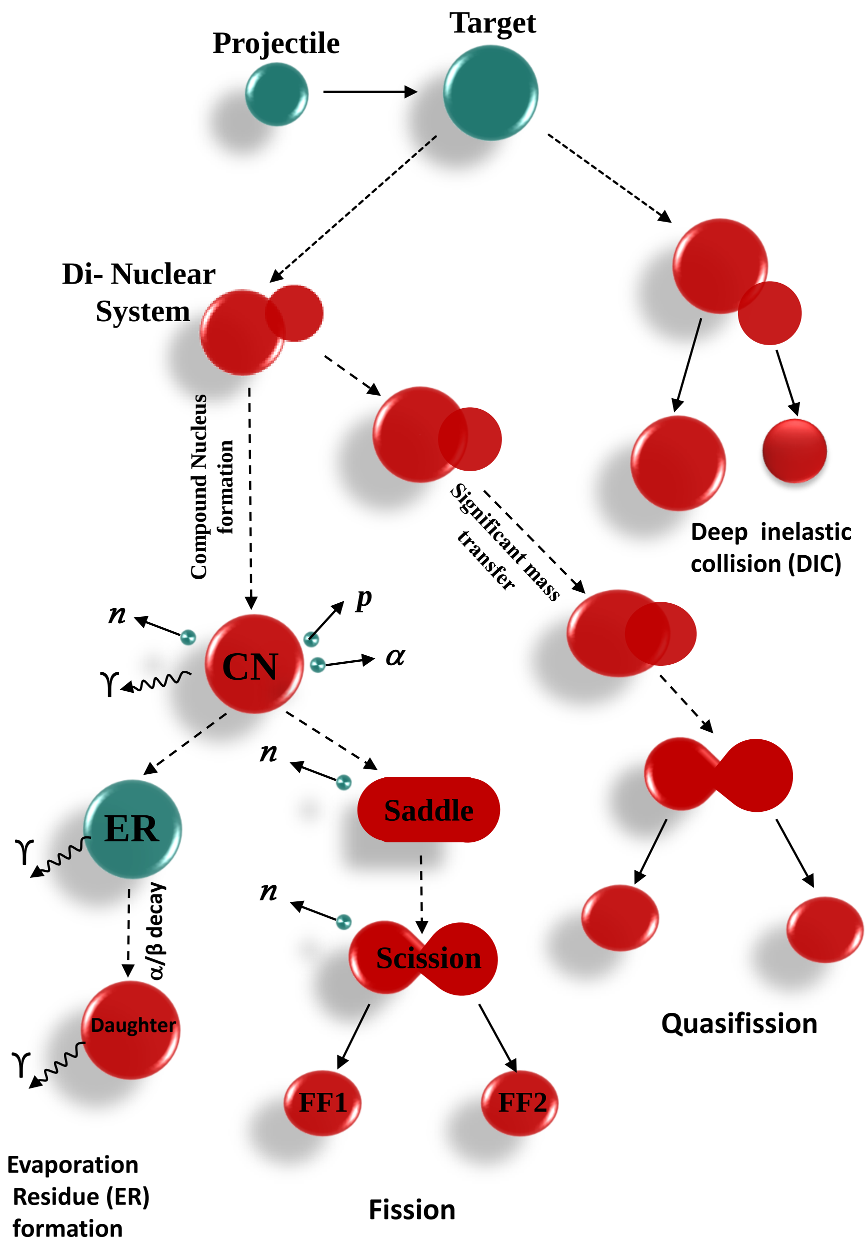

Figure 1.8: A schematic diagram illustrating different heavy ion induced reaction channels after formation of a composite system of projectile and target.

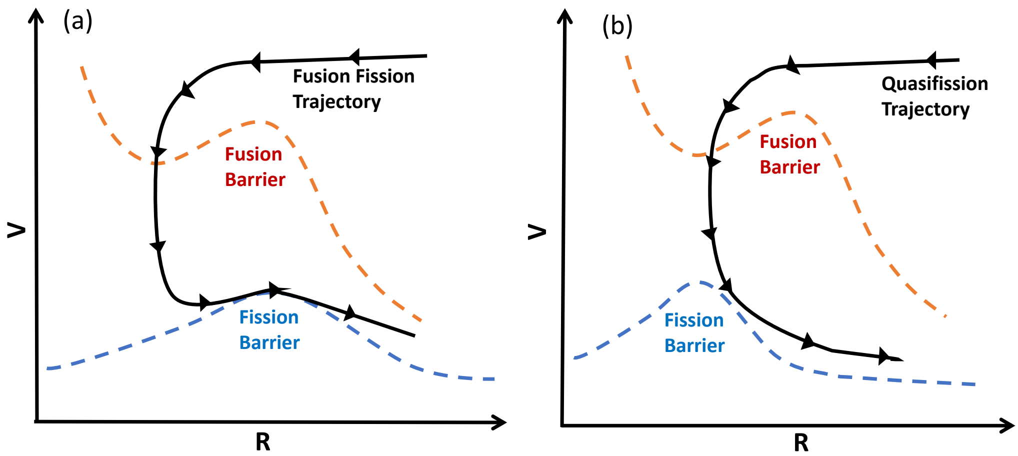

Figure 1.9: A schematic diagram illustrating potential energy surface and trajectories in case of (a)compound nucleus fission and (b)quasifission.

described below.

1. Mass asymmetry (or Charge product) of projectile and target ($\alpha = (A_p - A_T)/(A_p + A_T)$): Dynamical model calculations [45, 46, 47] based on the evolution of the composite system in a three dimensional space of nuclear shape explains the effect of entrance channel mass asymmetry on the process of quasifission, in terms of Businaro-Gallone critical mass asymmetry (α_{BG}). Here, α_{BG} is the point where elongated shape get unstable with respect to asymmetric deformations [48]. The systems having entrance channel mass asymmetries on either side of this point follow different path to fusion. For entrance channel mass asymmetry, α, greater than α_{BG}, the composite system experience a driving force towards larger asymmetry and smaller

elongation, leading to the formation of a CN. For $\alpha < \alpha_{BG}$, the mass flow from heavier target to lighter projectile increases, resulting in formation of a more elongated shape and hence increase in quasifission probability. Later, Abe [49] parametrized the fissility (χ) dependence of α_{BG} in simple form as,

$$\alpha_{BG} = \begin{cases} 0 & \text{if } \chi < \chi_{BG} \\ p\sqrt{\frac{(\chi-\chi_{BG})}{(\chi-\chi_{BG})+q}} & \text{if } \chi > \chi_{BG} \end{cases} \tag{1.8}$$

where, p=1.12, q=0.24 and χ_{BG}=0.396. Here, following the formalism of Ref. [47], the CN fissility χ is calculated as,

$$\chi = \frac{Z^2/A}{50.883\{1 - 1.7826[(N-Z)/A]^2\}} \tag{1.9}$$

Although, it was predicted that the onset of quasifission will take place for $Z_pZ_t > 1600$ as there will be requirement of extra-extra push to form a CN, later studies reported existence of QF for values of Z_pZ_t far less than this threshold.

2. Deformation alignment: In the investigation of experimental data, presence of quasifission was observed due to deformation in colliding nuclei also. Collisions with the tips of the deformed target nuclei result in quasifission, while collisions with the sides result in fusion. This phenomenon was explained as, once the composite system is inside the fusion barrier, the radial motion is rapidly damped, and the nuclear system will start to evolve in shape over the potential energy surface. Hence, the trajectory leading from the most

compact injection i.e collisions with the sides, results in fusion fission and the one leading from tip to tip collision, results in QF.

3. Asymmetry of the projectile and target N/Z ratios: Experimental data have also indicated that, reactions with small isospin asymmetry and magic numbers in the entrance channel reduce quasi-fission. Also, small isospin asymmetry with non-magic systems show more quasi-fission. In case of large initial isospin asymmetry and magic system, N/Z equilibration takes place in the early stage of fusion process, modifying the identities of the collision partners and resulting in enhancement of QF.

In a systematic analysis of large set of data by R. du Rietz *et al* [50], the presence of QF in different region of nuclear chart was analysed by mapping the mass-angle distribution (MAD) characteristics with QF timescales. The different MAD categories can be briefly described as,

1. MAD 1: This category of MAD represents fast QF, where scission occurs very soon after initial contact. Since the sticking time is small, the composite system reseparate before completing one full rotation. These MADs exhibit strong mass angle correlation. Due to little mass transfer, the fission like fragments from such reactions lie close to (and may even overlap with) target like or projectile like fragments (deep-inelastic events).

2. MAD 2: Having sticking time a little more than that of MAD 1, these mass-angle distributions exhibit a clear non isotropic distribution.

3. MAD 3: This MAD category corresponds to slow QF where due to very

long sticking time, a significant mass transfer takes place. The composite system undergo more than one full rotation resulting in loss of mass-angle correlations. Since these fission like events appear close to or inside the fusion-fission mass region, experimental identification of such QF events is extremely difficult.

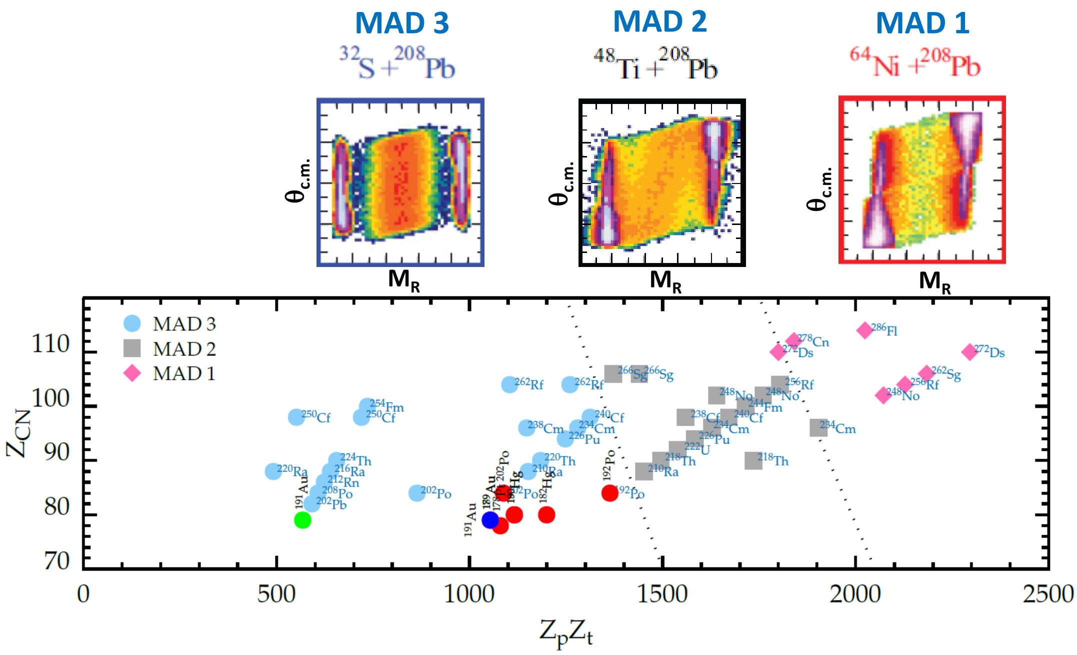

Figure 1.10: Different experimental MAD1, MAD2 and MAD3 plotted with respect to entrance channel parameter Z_pZ_t. Here, Diamond (pink), square (gray) and circle (blue) represents MAD category 1,2 and 3 respectively. A representative plot of each MAD type is also shown in upper half of the figure. Dotted lines represents empirical boundary for separating different catagory. Data taken from [50]. Red circles data represents few studies done in sub-lead region. Green and blue circles represents two different entrance channel measurements forming ^{191}Au.

A comparison of different experimental MADs with respect to entrance channel parameter Z_pZ_t is shown in Fig. 1.10. On the lighter side of this explored map i.e for smaller Z_pZ_t values, experimental evidence of QF has been found in ^{202}Po (Z = 84), formed in ^{34}S+^{168}Er reaction having Z_pZ_t as low as 1088. Here, red circles represents very few measurements performed for getting a deeper insight of shell effects in fission around A$\sim$200. Although the possible presence of QF was not ruled out in ^{40}Ca+^{142}Nd reaction [57], its exact nature and extent in the sub-Pb region remained unexplored.

Although predicting the amount of QF for a given bombarding energy and projectile-target combination is still a challenge, its presence can be easily identified in fission observables. Early experimental evidence of QF include, anomalous angular anisotropy, broadened mass distribution widths of fission fragments and strong correlation between fragment mass and its emission angle. In the present study, later two phenomenon associated with QF has been exploited to study its presence for reactions populating neutron deficient nuclei in pre-actinide region.

1.6 Motivation of present study

To get a detailed understanding of role of shell effects in deciding fission fragment mass distribution around A$\sim$200, we planned three investigations in the present thesis work with the aim to disentangle the role of entrance channel dynamics versus shell effects in deciding fragment mass split, examine evolution of different modes of fission with compound nucleus N/Z and do a consistent analysis of low-energy fission fragment mass distribution data collected so far to get a unified picture of fission process. A brief description of all these studies is given below.

* Since the mass of reaction products coming from QF process can severely overlap with the mass of fragments originating from fusion fission, in many cases, depending on entrance channel properties this non-equilibrated process can mimic the presence of multi-modal CN fission. Investigation of the role of QF is essential for interpreting the so far measured data in sub-Pb region unambiguously and accurately model the excitation energy dependence of microscopic effects. Ignoring this aspect, and directly correlating the deviations from single Gaussian distribution with the microscopic effects may lead to ambiguity in the inferred multi-modal fission in sub-Pb region. Measurement of FF mass distributions for ^{191}Au populated via two very different entrance channels namely ^{16}O+^{175}Lu (Fig. 1.10, green circle) and ^{37}Cl+^{154}Sm (Fig. 1.10, blue circle) will allow us to examine the presence of quasifission and disentangle the role of entrance channel dynamics versus shell effects in FFs.

* By measuring FF mass and TKE distribution for ^{198}Po, we can study the evolution of asymmetric and symmetric components as a function of N and Z of the fissioning system. FF mass distribution data in actinide region displays a predominantly asymmetric fission for neutron *rich* nuclei. However, in the sub-Pb region, experimental data displays an opposite trend. Here, the fission fragment mass distribution is found to be most asymmetric for neutron $deficient$ ^{180}Hg. With Z=84 the element polonium is situated ideally midway between mercury (Z = 80) and traditional actinides (Z$\geq$ 88), over which fragment properties are observed to change fast [31]. Furthermore, isotope

A = 198 is located at the centre of the area studied with the β-delayed and electromagnetic induced approaches, over which the fragment properties were observed to change fast [31, 109]. Information on isotope A = 198 permits us to proceed further along the polonium chain and to map out the balance between asymmetric and symmetric splitting as a function of the fissioning system N and Z.

* A consistent analysis of the experimental information collected so far on asymmetric fragmentation in low-energy fission of neutron-deficient nuclei around lead can help us to get a unified picture of fission process. As discussed in section 1.3, the data from well studied actinide region, also known as "old" island of asymmetric fission suggested that closed shell structure of ^{132}Sn dominate the low energy fission fragment mass split [23]. Later, an extensive set of data from GSI [10], demonstrated the transition from mostly asymmetric fission in the actinides towards symmetric fission as the dominant mode in the light thorium to astatine region. Other studies by Itkis *et al* [22] in the mass region A$\sim$185-215 which showed signatures of asymmetric component also along with the symmetric fission, thought to be supporting this result of primarily symmetric fission in sub-Pb region. These observations outlined a trend from which it was anticipated that ^{180}Hg will undergo symmetric fission populating two semi-magic ^{90}Zr nuclei. An unexpected observation of asymmetric fission of ^{180}Hg opened a whole "new" island of asymmetric fission just a decade ago. This analysis will allow us to seek a connection between this "new" and the "old" islands of asymmetric fission.

1.7 Structure of the thesis

The thesis is organized into seven chapters. The present chapter highlights the importance of understanding fission process and its study in pre-actinide region. Current status of the field and motivation of the present thesis work is also discussed in this chapter. Chapter 2 contains a brief description of various theoretical models used to explain fission in pre-actinide region. Chapter 3 contains the details of present experimental setup and data acquisition system along with a brief description of the Pelletron Linac Facility. The analysis method to separate fission events and deduction of fragment mass and TKE are discussed. Corrections in the fragment mass due to their energy loss in the target and backing on event by event basis are also explained. The results of measurement of FFs mass distribution from ^{191}Au as well as its comparison with various theoretical model prediction are given in chapter 4. Measurement of mass and TKE distribution for ^{28}Si+^{170}Yb forming ^{198}Po is provided in Chapter 5. Chapter 6 contains a systematic study of all available MD measurements for low energy fission in actinide and pre-actinide region, to better understand the process of nuclear fission and get a unified picture. Lastly, the summary of the thesis and future scope of the work are highlighted in Chapter 7.

2

Theoretical Models

The complexity of the process of nuclear fission manifest itself in the fact that several properties of nuclear matter and nuclear dynamics play an important role at different stages of the process. For example, at low excitation energy nuclear internal structure plays key role in deciding final fission fragment distributions whereas it is dissipative dynamics of the process that results in enhancement of intrinsic excitations and rupture of nucleon pairs along the path from the saddle to the scission point [9, 16, 34, 35, 36]. Being many body problem, modeling of this process is extremely challenging. So far, it is beyond the capability of supercomputers to model a single fission event by considering the full coupling between intrinsic and collective degrees of freedom. However, by modeling different steps of the nuclear fusion fission process, one can always make prediction and interpretation of experimental data.

Some of the relevant theoretical models for heavy ion fusion-fission reactions at energies around the Coulomb barrier are discussed in next section.

2.1 Nuclear fusion and formation of compound nucleus

As shown in Fig 1.5, when the relative distance between the two interacting nuclei reduces to $r < R_b$, the system (projectile + target) falls into the pocket of nucleus-nucleus potential. Inside this pocket, nucleon-nucleon interaction becomes prolific due to significant density overlap and cause substantial loss of kinetic energy and angular momentum from the relative motion. As a result, the composite system no longer remains able to escape from the potential well and the whole process leads to fusion of two colliding nuclei. If this composite system gets sufficient time to equilibrate in all degrees of freedom (e.g energy, shape etc.), it will loose all its memory of entrance channel, other than conservation of energy, angular momentum and other relevant good quantum numbers. This process is called complete fusion and the nucleus so formed is called compound nucleus (CN). This excited, rapidly rotating system which is highly unstable, eventually decays into smaller fragments.

In classical picture, the process of nuclear fusion occurs only when the energy of the projectile is greater than the Coulomb barrier and the trajectories for different angular momentum values lie below a certain value (l_{crit}), i.e $E_{c.m} > V_B$ and transmission coefficient,

$$T_l = \begin{cases} 1 & \text{if } l < l_{crit} \\ 0 & \text{if } l > l_{crit} \end{cases} \tag{2.1}$$

Thus, the fusion cross section is given by

$$\sigma_{fus} = \frac{\pi}{k^2}\sum_{l=0}^{\infty}(2l+1)T_l = \frac{\pi}{k^2}\sum_{l=0}^{l_{crit}}(2l+1) \approx \frac{\pi}{k^2}l_{crit}^2 \tag{2.2}$$

substituting

$$l_{crit}\hbar = \sqrt{2\mu\left(E_{c.m} - V_b\right)}R_b \quad \text{and} \quad k\hbar = \sqrt{2\mu E_{c.m}} \tag{2.3}$$

we get, well known classical expression for fusion cross section as

$$\sigma_{fus} = \begin{cases} \pi {R_b}^2 \left(1 - \frac{V_b}{E_{c.m}}\right) & \text{if } E_{c.m} > V_b \\ 0 & \text{if } E_{c.m} < V_b \end{cases} \tag{2.4}$$

In a non-classical and more realistic picture, a nucleus is a many body quantum system. The two interacting nuclei may undergo fusion by quantum mechanical tunnelling through Coulomb barrier, when $E_{c.m} < V_b$. Approximating the Coulomb barrier as an inverted parabola, the corresponding l dependent transmission coefficient can be written in Hill-Wheeler form [37]as,

$$T_l = \frac{1}{1 + exp\left[\frac{2\pi}{\hbar\omega_l}\{V_b(l) - E_{c.m}\}\right]} \tag{2.5}$$

Here, $V_b(l)$ is the barrier height for the l^{th} partial wave and $\hbar\omega_l$ represent the corresponding barrier curvature. Generally, it is assumed that the barrier position and its curvature are independent of the angular momentum, such that,

$$\hbar\omega_l \simeq \hbar\omega_0 \quad \text{and} \quad V_l \cong V_0 + \hbar^2 l(l+1)/2\mu {R_b}^2 \tag{2.6}$$

Since

$$\sigma_{fus} = \frac{\pi}{k^2}\sum_{l=0}^{\infty}(2l+1)T_l \tag{2.7}$$

The sum can be replaced by integration in the above equation to obtain fusion cross section,

$$\sigma_{fus} = \frac{\hbar\omega {R_b}^2}{2E_{c.m}} \ln\left[1 + exp\{\frac{2\pi}{\hbar\omega}(E_{c.m} - V_b)\}\right] \tag{2.8}$$

For $E_{c.m} \gg V_b$, the above equation reduces to the well known classical formulae (Eqn. 2.4) and for $E_{c.m} \ll V_b$, it can be represented as

$$\sigma_{fus} = \frac{\hbar\omega {R_b}^2}{2E_{c.m}} exp\left[\frac{2\pi}{\hbar\omega}(E_{c.m} - V_b)\right] \tag{2.9}$$

The above expression shows that fusion cross section decreases exponentially with decrease in energy below the Coulomb barrier. This model is called One-Dimensional Barrier Penetration Model (1-DBPM), since the radial separation is the only degree of freedom involved in this model.

This prescription could successfully explain the fusion cross sections of reactions involving light nuclei but under predicted the experimental fusion cross sections for heavy ions at near and sub-barrier energies. Unexpected variations among the measured cross sections for sub-barrier fusion in different isotopes of a given element was also observed. It was concluded that, the assumption of inert, spherical nuclei interacting through an effective one-dimensional potential is not adequate [39, 40, 41]. A detailed investigation of other degrees of freedom showed that the coupling of relative motion and intrinsic degrees of freedom has an effect of changing the height of the barrier [42]. For example, let us consider the coupling of nuclear shape degree of freedom for ^{16}O+^{154}Sm reaction, shown in Fig 2.1. Here, the projectile ^{16}O is spherical and the target ^{154}Sm have static prolate ($\beta_2 = 0.27$) deformation. Black dashed line represent the fusion barrier when both the interacting nuclei are considered as sphere.

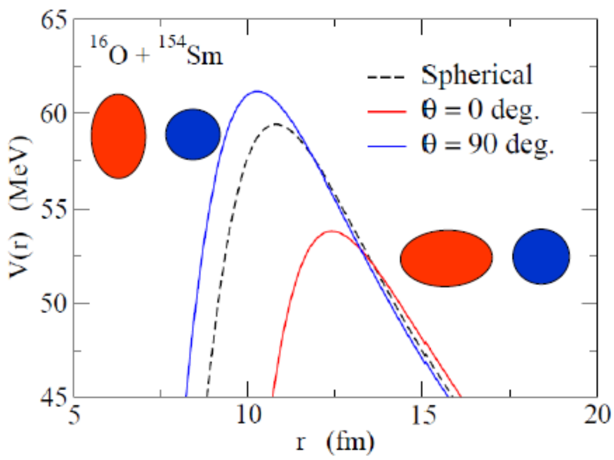

Figure 2.1: Dependence of barrier height on deformation of the target nucleus for the ^{16}O+^{154}Sm reaction [42].

In this case, the interaction barrier will depend on the orientation of the deformed target nucleus relative to the direction of approach of the projectile. When the projectile approach target along the axis of symmetry of the target, the potential barrier is lowered and fusion is enhanced (red solid line). Similarly, when the projectile approach target perpendicular to the axis of symmetry of the target, the potential barrier increases and fusion is reduced (blue solid line). In the same way, a spectrum of barriers will be faced by the incoming flux, depending on the orientation of the target. Since the fusion cross section varies exponentially with respect to the barrier height (Eqn. 2.9), the net effect of the distribution of barriers is to enhance the fusion cross section.

In a similar manner, transfer of nucleons and inelastic excitation etc. also leads to a distribution of barriers, resulting in enhancement of fusion cross section for energies below the one dimensional barrier.

2.1.1 Coupled channel framework

As described earlier, the most successful explanation of sub barrier fusion enhancement came from coupling aided tunnelling. When many channels get coupled in nucleus-nucleus interaction, a spectrum of barriers is generated for the incident flux. Depending upon the coupling mechanism, some of these barriers may lie higher than the uncoupled barrier and some may be lower. The resultant total fusion cross section is thus a weighted sum of fusion through each barrier. This effectively results in enhancement of fusion cross section and broadening in angular momentum (ℓ) distribution.

The coupled channel code CCFULL has been used in the present thesis work [42, 43]. This code solves the coupled channel equations numerically to calculate fusion cross sections and mean angular momenta of compound nucleus. For computing fusion cross section, it exclusively couples the relative motion of the colliding nuclei to the nuclear intrinsic motions like inelastic excitations. In this framework, the total Hamiltonian for the system can be written as a sum of the Hamiltonians of intrinsic motion, $H_0(\zeta)$, relative motion, $K(r) + V(r)$ and the coupling interactions, $V_{coup}(r, \zeta)$, of the relative coordinate with the internal degrees of motion.

$$H(r, \zeta) = H_0(\zeta) + K(r) + V(r) + V_{coup}(r, \zeta) \tag{2.10}$$

for an arbitrary internal degree of freedom α, $H_0(\zeta)\psi_\alpha(\zeta) = \epsilon_\alpha\psi_\alpha(\zeta)$, where,$\epsilon_\alpha$ represents the internal energy of the nucleus. The wave function to describe different possible reaction channels in collision of two nuclei can be written as, $\varphi_\alpha(r, \zeta) = \psi_\alpha(\zeta)\chi_\alpha(r)$. Assuming that for every exit channel, the bare potential $V_{\alpha\alpha}(r)$ (expressed as a sum of the nuclear, Coulomb and centrifugal potential) is same as the entrance channel potential, solving the Schroedinger equation for Hamiltonian of Eqn. 2.10 will give us the coupled channel equation,

$$\left[\epsilon_\alpha + K(r) + V_{\alpha\alpha}(r) - E\right]\chi_\alpha(r) + \sum_{\alpha \neq \alpha'} V_{\alpha\alpha'}(r)\chi_{\alpha'}(r) = 0 \tag{2.11}$$

here, $V_{\alpha\alpha'}(r) = \langle\psi_\alpha|V(r) + V_{coup}(r, \zeta)|\psi_{\alpha'}\rangle$ is the matrix element of the coupling interaction. At a suitable position where the Coulomb pocket has a minimum, CCFULL employs an incoming wave boundary condition (IWBC) that corresponds to strong absorption in the interior region of the barrier, so that the incoming flux never returns. This code then calculates barrier penetrability for each partial wave separately. The code also takes care of vibrational or rotational coupling between the projectile and the target using harmonic limit or coupling with a pure rotor respectively. In the present thesis work, CCFULL has been used to estimate the angular momentum distribution of the fissioning nucleus [42, 43].

2.2 Decay of compound nucleus

Formation of a compound nucleus can be considered as a two step nuclear process. In the first step, the projectile crosses the fusion barrier and combines with the target to form a composite system with total number of protons equal to $Z_p + Z_t$ and total number of neutrons equal to $N_p + N_t$. In the second step, the multiple interaction among these nucleons leads to complete equilibration in all degrees of freedom (shape, mass asymmetry, energy etc.), forming a CN with an excitation energy E^* and angular momentum J. The CN so formed have no memory of its formation and the subsequent evolution of this equilibrated system depends only on conserved quantities.

The decay of an equilibrated, hot, rotating CN can be divided into three main categories: (a) emission of nucleons or clusters (b) γ-ray emission and (c) fission and is successfully described by the Statistical model. Clearly, the number of nucleons are not very large for the applicability of statistical mechanics. However, the number of possible configurations in a very short energy range, E to $E + \Delta E$ are very large and increases exponentially with excitation energy. Even with the lowest excitation energies, there are a number of levels to which a CN can decay in different ways. Thus the complexity of the process necessitates the use of statistical model to describe the decay of CN. Statistical model works on the basic assumption that, all *open* decay channels are equally likely to be populated. Such that, the probability of decay to a particular channel or a group of n channels out of total

N open channels is given by n/N. Here, *Open* channel means a particular final state, specified by all quantum numbers, which can be reached from the initial state without the hindrance of barrier penetration. If a potential barrier is present in some open channel, the probability of decay in that particular channel will be accordingly reduced by the barrier penetration probability.

When the excitation energy of the CN is high, particle evaporation and fission are the dominant decay channels. During evaporation, particles like neutrons, protons, α- particles and some times cluster of nucleons are emitted. Such emission can take place from the CN as well as from the decay products until the excitation energy of the decaying nucleus is greater than particle separation energy. If the excitation energy is greater than the fission barrier, the path of fission decay mode is also probable, where the CN splits up into two fragments of comparable mass. When the decaying nucleus no longer have enough excitation energy to decay through evaporation or fission, the process of gamma emission takes over the decay process. Statistical analysis of all three decays modes can be understood as discussed below.

2.2.1 Emission of nucleons or clusters

Let, there is an ensemble of nuclei in equilibrium with each other such that all nuclei have energies in the range E_i to $E_i + dE_i$ and angular momentum J_i. As soon as a particle τ with kinetic energy ϵ, spin s and angular momentum ℓ is emitted from nuclei, the daughter nuclei with excitation energy E_f to $E_f + dE_f$

and spin J_f will be formed such that the decay width can be estimated as,

$$\Gamma_\tau(E_i, J_i; E_f, J_f, s) = \frac{1}{2\pi} \sum_{S=|J_f-s|}^{J_f+s} \sum_{\ell=|J_i-S|}^{J_i+S} T_\ell(\epsilon) \frac{\rho(E_f, J_f)}{\rho(E_i, J_i)} \tag{2.12}$$

where $S = J_f + s$ is the spin of this τ^{th} decay channel. Final energy of the nucleus after decay, $E_f = E_i - S_\tau - \epsilon$ where S_τ is the separation energy of particle τ. $T_\ell(\epsilon)$ represents the barrier transmission coefficient for the emission of particle τ which is calculated from optical model potential of the emitted particle and the residual nucleus such that in a time reversed reaction $T_\ell(\epsilon)$ represents transmission coefficient for formation of a CN in reaction of the emitted particle and the residue nucleus with excitation energy E_f and spin J_f. The total evaporation probability obtained by integrating over allowed energy range and summing over angular momentum is given as,

$$\Gamma_{eva} = \sum_\tau \sum_{J_f,s} \int_{\epsilon=0}^{E_i-S_\tau} \Gamma_\tau(E_i, J_i; E_i - S_\tau - \epsilon, J_f, s) d\epsilon \tag{2.13}$$

2.2.2 γ-ray decay

Following a similar method described above, the rate of γ-ray emission can be obtained by replacing the transmission coefficient by γ-ray strength function.

$$\Gamma_\lambda(E_i, J_i; E_f, J_f) = C_\lambda(\epsilon_\gamma) {\epsilon_\gamma}^{2\lambda+1} \frac{\rho(E_f, J_f)}{\rho(E_i, J_i)} \tag{2.14}$$

here, ϵ_γ is the energy of the emitted γ radiation and λ is the multipolarity of the transition. $C_\lambda(\epsilon_\gamma)$ represents an average squared intrinsic matrix element that have energy dependence in some cases, like giant dipole and giant quadrupole resonances, when the distribution of radiative strength is not uniform. The factor ${\epsilon_\gamma}^{2\lambda+1}$ comes from the long wavelength limit $\lambda_\gamma / R_{nucl} > 1$. The total γ ray emission width, summed over multipolarity and angular momentum of the final states and integrated over energy is given as,

$$\Gamma_\gamma = \sum_{\lambda} \sum_{J_f} \int_{\epsilon=0}^{E_i} \Gamma_\lambda(E_i, J_i; E_i - \epsilon, J_f) d\epsilon \tag{2.15}$$

2.2.3 Fission decay

As described in the introduction of the present thesis, nuclear fission is an extremely complex process that results in drastic rearrangement of nucleons of a single nucleus into two or more nuclei. Unlike particle evaporation, the process of nuclear fission is governed by multiple macroscopic as well as microscopic phenomenon. For instance, at low excitation energy, the deformation of the fissioning system at scission is decided by the collective motion of nucleons while the final fragment distributions are strongly affected by the shell structure in their energy levels. The fission decay rate of a particular fissioning system depends on the properties of the saddle point configuration, also known as transition state, where the nucleus becomes committed to fission. At this point, energy available for the intrinsic excitation is minimum and most of the energy goes into deforming the system. Let, E_f and J_f represents energy and angular momentum of the fissioning nucleus at the saddle point. The fission decay width for the compound nucleus with excitation energy E_i and angular momentum J_i can be written as,

$$\Gamma_{fis}(E_i, J_i; E_f, J_f) = \frac{1}{2\pi}\frac{\rho(E_f, J_f)}{\rho(E_i, J_i)}T_f(\epsilon) \tag{2.16}$$

with

$$E_f = E_i - B_f(J_i) - \epsilon \tag{2.17}$$

where, $B_f(J_i)$ is the angular momentum dependent fission barrier and ϵ is the kinetic energy at the saddle point. According to the Hill-Wheeler approximation, the transmission coefficients $T_f(\epsilon)$ are taken to be unity if the total available energy is more than the fission barrier and zero otherwise. By integrating over all allowed energies and summing over various allowed angular momenta, the total decay width can be obtained as,

$$\Gamma_{fission} = \sum_{J_f}\int_0^{E_i - B_f(J_i)} \Gamma_{fis}(E_i, J_i; E_i - B_f(J_i) - \epsilon, J_f)d\epsilon \tag{2.18}$$

2.2.4 Total decay rate

The total decay width of CN can now be obtained by simply adding all these three possible decay widths as,

$$\Gamma(E_i, J_i) = \Gamma_{eva} + \Gamma_\gamma + \Gamma_{fission} \tag{2.19}$$

such that the probability of population of any given channel, x becomes,

$$P(E_i, J_i; x) = \frac{\Gamma(E_i, J_i; x)}{\Gamma(E_i, J_i)} \tag{2.20}$$

and corresponding cross section for population of channel x can be obtained as

$$\sigma(x) = \sum_{J_i} \sigma(E_i, J_i) P(E_i, J_i; x) \tag{2.21}$$

where $\sigma(E_i, J_i)$ is the production cross section of the decaying nucleus with excitation energy E_i and angular momentum J_i.

In the present thesis work, we used statistical model code PACE for estimation of pre-fission neutron multiplicity and the effective energy carried by these neutrons before fission takes place [105, 106].

2.3 Nuclear Fission Models

Although an extensive description of the fission process and associated observables is beyond the scope of this thesis work, an overview of different fission models relevant to the work of this thesis is presented in this section.

2.3.1 Scission-Point Model

Scission-Point model is a static model of nuclear fission, developed by B. D. Wilkins *et al* in middle of 1970s [9]. This model calculates the distribution of fission fragments by assuming statistical equilibrium among collective degrees of freedom at the scission point. Neglecting the evolution of the fissioning system prior to the scission point, this model predicts the distribution of fission fragments by calculating the relative potential energies of the complementary nascent fragment pairs at or near scission point. This relative potential energy was calculated by considering the fragment pairs as nearly touching, coaxial spheroids with a tip separation d and deformations β_1 and β_2 respectively. Such that the total potential energy of the system $V(N_1, Z_1, \beta_1, N_2, Z_2, \beta_2, \tau, d)$ can be written as a sum of collective (V_{LDM}) and single-particle terms, i.e shell ($S_{1,2}$) and pairing ($P_{1,2}$) corrections for each spheroid along with mutual Coulomb (V_C) and nuclear potential (V_N) terms (describing the interaction between the spheres) as,

$$\begin{aligned} V(N_1, Z_1, \beta_1, N_2, Z_2, \beta_2, \tau, d) &= V_{LDM}(N_1, Z_1, \beta_1) + V_{LDM}(N_2, Z_2, \beta_2) \\ &+ S_1(N_1, \beta_1, \tau) + S_1(Z_1, \beta_1, \tau) + S_2(N_2, \beta_2, \tau) + S_2(Z_2, \beta_2, \tau) \\ &+ P_1(N_1, \beta_1, \tau) + P_1(Z_1, \beta_1, \tau) + P_2(N_2, \beta_2, \tau) + P_2(Z_2, \beta_2, \tau) \\ &+ V_C(N_1, Z_1, \beta_1, N_2, Z_2, \beta_2, d) + V_N(N_1, Z_1, \beta_1, N_2, Z_2, \beta_2, d) \end{aligned} \tag{2.22}$$

where, τ represents intrinsic single-particle excitations. The coupling among collective degrees of freedom being strong compared to that between collective and single-particle degrees of freedom, the statistical equilibrium among collective states was characterized by a collective temperature T_{coll}. So that, the relative probabilities of formation of complementary fission fragments pairs can be given as,

$$\Omega(N, Z, \tau, d) = \int_{\beta_1=0}^{\beta_{max}} \int_{\beta_2=0}^{\beta_{max}} exp\left[\frac{-V(N, Z, \beta, \tau, d)}{T_{coll}}\right] d\beta_1 d\beta_2 \tag{2.23}$$

This model could successfully reproduce the general trends of two or three humped fission fragments mass distribution for a wide range of nuclide. Yet, it could not explain the position of these mass distributions and also underestimated its width.

2.3.2 Brosa Model

Also known as the Random Neck Rupture Model (RNRM), this model was developed by Ulrich Brosa *et al* in the year 1990 [60]. Unlike scission point model, this prescription could explain the experimentally observed position and width of the fission fragments mass distribution by considering the properties of the fissioning configuration, and not only the fragments themselves.

In this model, the pre-fragments at scission are described as two spheroids connected through a hyperbolic flat neck. As the fissioning system proceeds towards scission, a dent is developed in the neck region which gets further deepened by the capillary force, finally leading to fission. Since the dent can develop at any position in the neck, the larger the neck, the higher the number of possible mass split, and hence, the wider the distribution of fragments.

Instead of calculating the full potential landscape as a function of the deformation parameters, this model assumes different bifurcation points in the potential of fissioning system. At each bifurcation point, the nucleus can choose between different paths to disintegrate and each path corresponds to a separate fission channel. The five fission channels considered in this model are:

1. Superlong channel: This channel corresponds to symmetric valley of the potential energy surface. Assuming large deformation in both fragments,

this channel produces a wider fragment mass distribution around $A_{cn}/2$ with low total kinetic energy and high neutron evaporation.

2. Standard I channel: Derived by magic nucleus ^{132}Sn, this channel produce asymmetric fission fragment mass distribution with one peak centred around $A \sim 135$ and $Z \sim 52$. This channel predicts a highly deformed light fragment along with a nearly spherical heavier partner. Also, as a consequence of high deformation energy in the lighter fragment its neutron evaporation is higher than the heavier one. Assuming a compact shape at scission, this channel predicts high total kinetic energy.

3. Standard II channel: Similar to standard I, this channel produce asymmetric fission fragment mass distribution with one peak centred around $A \sim 140$ and $Z \sim 54$. It predicts, a highly deformed heavier fragment along with a nearly spherical light partner and hence the scission shape in this channel is less compact than standard I, leading to larger total neutron evaporation and lower total kinetic energy.

4. Supershort channel: Observed only in nuclei heavier than ^{252}Cf, this channel predicts a narrow fission fragment mass distribution around $A_{cn}/2$. By considering two fragments of almost spherical shape, this channel produce negligible neutron evaporation and high total kinetic energy.

5. Super-asymmetric channel: This channel is rarely presents and predicts a highly asymmetric mass distribution.

2.3.3 A semi-empirical approach towards understanding fission

As discussed earlier in this chapter, so far, it is beyond the capability of supercomputers to simulate a single fission event by considering all macroscopic as well as microscopic aspects of nuclear fission. In this scenario, the computer code GEF (GEneral description of Fission observables) is a tool that describes nearly exhaustive list of fission observables in a mutually consistent way. Developed by K.-H. Schmidt and B. Jurado, this code works by combining the physical concepts from quantum mechanics, nuclear dynamics and statistical mechanics with the empirical information [2, 61, 62]. The code bypasses the complex microscopic calculations by making use of the regularities observed in experimental data over a wide set of fissioning systems and fission quantities [63].

GEF describes the fragment distributions by calculating the potential energy surface based on the separability principle [64]. According to this principle the macroscopic potential depends on the properties of the compound nucleus, while the microscopic potential is fully determined by the numbers of neutrons and protons in the nascent fragments. An extensive investigation of data by Mosel and Schmitt showed that, the final mass split largely reflects the asymmetric properties of the valley(s) behind the outer saddle(s) [65]. This early manifestation of fragment shells is incorporated in the code using two-center shell model, where, the wave functions in a slightly necked-in potential are found to be already essentially localized in the two parts of the system.

To estimate the pre neutron fragment partition at scission, the code connects fission channels (described in sec. 2.3.2) with the statistical population of quantum oscillators in the mass-asymmetry degree of freedom that form the fission valleys. Each fission valley has an associated potential well characterized by its position, depth, and curvature that can be traced back to the macroscopic and microscopic (shells in the fragment proton or neutron subsystem) potential. It is the superposition of different shells in the two fission partners and its interference with the macroscopic potential that create different mass distributions for different fissioning systems. The code also introduces effective potential which account for the influence of dynamical effects from saddle to scission. This works on the fact that, dynamical effects (influence of dissipation and inertial forces) induce a kind of memory on the fission trajectory. Each collective degree of freedom have a characteristic time during which the potential energy surface affects the final observable distribution. Being a stochastic process, this induces a broadening in the final distributions. By adjusting the parameters to reproduce the final broadened distribution, the effective potential energy is calculated. This approach provides a consistent description of all available experimental observables over a wide range of fissioning systems. The accuracy of this code in terms of fission fragment distributions motivates the comparison performed in this work between the experimental data and the GEF code predictions.

2.3.4 Di-Nuclear System (DNS) Model

Since last four decades, QF has been a topic of intense research primarily because this non compound nuclear process severely inhibits the formation of super-heavy elements. A detailed description of experimental and theoretical development to understand this non-equilibrated process can be found in Refs. [50, 59, 91, 92, 93, 94, 95] and references therein. As discussed in section 1.5, the primary difference between fusion fission and quasifission mechanism is that in the later case the compact compound nucleus is not formed and system breaks into fission like fragments from the elongated shape itself. DNS model predicts the quasifission contribution for given system by considering fusion alone as a two step process [66, 67]. In the first stage, projectile overcomes the Coulomb barrier in its motion along the axis connecting the nuclear centres during collision and get captured with the target nuclei in nucleus-nucleus potential, forming a molecule like nuclear composite called di-nuclear shape (DNS). In the second stage, this system of two touching nuclei exchange nucleons by transfer until a CN is formed. If the system reseparates before completion of this second stage, it is called quasifission. Since the change of nuclear shape of the two touching nuclei is not large and overlap region is very small it is assumed that the shell structure of the interacting nuclei is retained during second step. Further this model predicts the formation of quasifission products by calculating the diffusion of these touching nuclei in the coordinates of mass and charge asymmetries and relative distance.

2.3.5 Hartree-Fock method

Since discovery of nuclear fission different types of energy density functionals (EDF) have been proposed to explain the process of nuclear splitting. In this method, the Fock-space Hamiltonian is replaced by an EDF defined through one-body densities or density matrices. Hartree-Fock (HF) method is one such microscopic approach where, Schrodinger equation for many interacting particles is solved in an approximate way, since the exact solution cannot be found. According to the HF method, one can find the corresponding wave function in a form of a determinant consisting of the single-particle wave functions by variation so that it would minimize the expectation values of a given Hamiltonian. Once the mean-field potential of the nuclei is obtained by calculating the expectation value of the Hamiltonian in the Slater determinant, the orbitals are calculated as eigenstates of this one-body mean-field potential. When the pairing correlations are included in the calculation, it is called Hartree-Fock-Bogoliubov (HFB) approximation **??**. In both these methods, wave functions representing different nuclear shapes are constructed by constraining the single particle density matrix. Immediately before scission, the fragment neutron and proton contents are determined by the proton and neutron densities on each side of the neck.

3

Experimental Aspects

Continuous research and development in various fields of engineering and technology have greatly improved the experimental tools and techniques required to study fission process. As we know, measurement of fission observables as a function of properties of the fissioning nuclei like A, N/Z, E^* etc. are crucial to understand fission dynamics. It is only due to these developed accelerator and detection technology, several fissionable nuclei are now accessible. Diverse types of beams provided by accelerator facilities made it possible to study fission of nuclei away from β stability lines. There are four basic techniques to study fission dynamics in exotic nuclei.

1. β delayed fission(βDF): As discussed earlier, β delayed fission is a two step process. In the first step, a parent nucleus undergoes β^+/β^- decay (depending on whether it is neutron deficient or neutron rich), populating the daughter nuclide in excited state(s). In the second step, if the excitation

energy of this daughter nuclei is greater than its fission barrier, the daughter nuclei decays through fission.

2. Electromagnetic induced fission: In this technique, a secondary beam of projectiles is formed using a spectrometer after fragmentation of a relativistic primary beam (1 A GeV ^{238}U, see Ref. [10, 15, 70]). Interacting electromagnetically with heavy secondary target (^{208}Pb), the nuclei in this secondary projectile beam fissions due to induced excitations (mostly resonances).

3. Transfer induced fission: This is a method of a direct few-nucleon transfer-induced fission e.g. (d,pf), (^{3}He,pf) or (^{6}Li,df) reactions. By measuring the type, energy and scattering angle of the outgoing ejectile, a specific fissioning nuclei can be studied in this technique [71].

4. Heavy-ion induced fusion fission: Heavy ion induced fusion reactions are characterized by the formation of a fully equilibrated compound nucleus where the initial relative kinetic energy and angular momentum of the projectile is converted into the intrinsic excitation energy and spin of the fused system.

As discussed earlier in section 1.3, even though the low excitation energy required for studying asymmetric fission of neutron-deficient pre-actinides nuclei can be ideally reached in β-delayed and electromagnetic-induced fission, due to stringent conditions like non zero β branching ratio, very long beam time etc., the number of systems accessible to these approaches are currently limited. The transfer induced fission measurements is not feasible for present study as one cannot populate a neutron *deficient* nuclei using this approach. Even for the case of relatively neutron rich nuclei a typical fission barrier of around 10 to 20 MeV along with very low fissility makes it very challenging to do transfer induced fission study in the pre-actinide region as it will require months of beam time to accumulate sufficient data.

Hence, we used heavy ion induced fusion fission method to measure fission fragment mass distributions for different measurements reported in this work. A brief review of tools utilized for production and detection of the fission fragment is provided in this chapter.

3.1 Accelerator Facilities

Measurements for fission fragment mass distribution of ^{191}Au have been carried out at Pelletron Linac Facility (PLF), Mumbai. It has a 14 UD Pelletron tandem accelerator procured from NEC, USA and an indigenously developed superconducting linear accelerator (LINAC) based on lead plated copper quarter wave resonators. The SNICS ion source, situated at the top of the accelerator tower, generates negative ions from cesium sputtering. These ions are initially accelerated to low energies (150-250 keV) in a short horizontal section and then pass through a magnet (injector magnet) for mass analysis and bending of the path of ions through 90° to inject it into the vertical accelerator column. After injection, these negative ions get accelerated towards the positively charged high voltage terminal situated in the middle. Due to this acceleration, negative ions gain an energy of V_T MeV, where V_T is the terminal voltage in MV (million volts). For the present accelerator, the maximum terminal voltage is 14 MV. This high electric potential at the terminal is achieved by a continuous transfer of charge to the terminal by means of the chain of steel pellets separated by insulators. Inside the terminal, the ions pass through a thin carbon foil ($\sim 5\ \mu g/cm^2$) or small volume of gas, where they lose several electrons producing a distribution of positively charged ions.

This distribution depends on the type and velocity of the ions. These positively charged ions at the terminal get repelled by the positive voltage at the terminal and are therefore accelerated towards ground potential. This results in an energy gain of qV_T MeV for an ion with charge q and the total energy gain of the ions becomes $E = (q+1)V_T$ MeV. At the end of the accelerating tube, an analyzing magnet is placed for charge and energy selection of the ions according to the relation $B = 720.76\frac{\sqrt{AE}}{q}$. Where, B is the magnetic field in Gauss and E is the energy in MeV. This analyzed beam of ions is then transported to the LINAC with the help of switching magnet. The LINAC consists of seven modular cryostats, each housing four lead plated quarter wave resonators (QWR). In LINAC, beam is boosted according to kinematical requirement of the reaction to be studied using these QWR. There are three beam lines 15°, 30°, and 45° in LINAC Hall-1, and three beam lines 15°, 30°, and 45° in LINAC Hall-2. The measurement of fragment mass distribution have been carried out at 30° beam line in LINAC Hall-1 using a 1.5 meter general purpose scattering chamber.

Measurements for fission fragment mass distribution of ^{198}Po have been carried out using the 15UD Pelletron LINAC accelerator at IUAC, New Delhi. The working principle of this accelerator is same as described above for PLF Mumbai, with maximum attainable voltage of 15 MV.

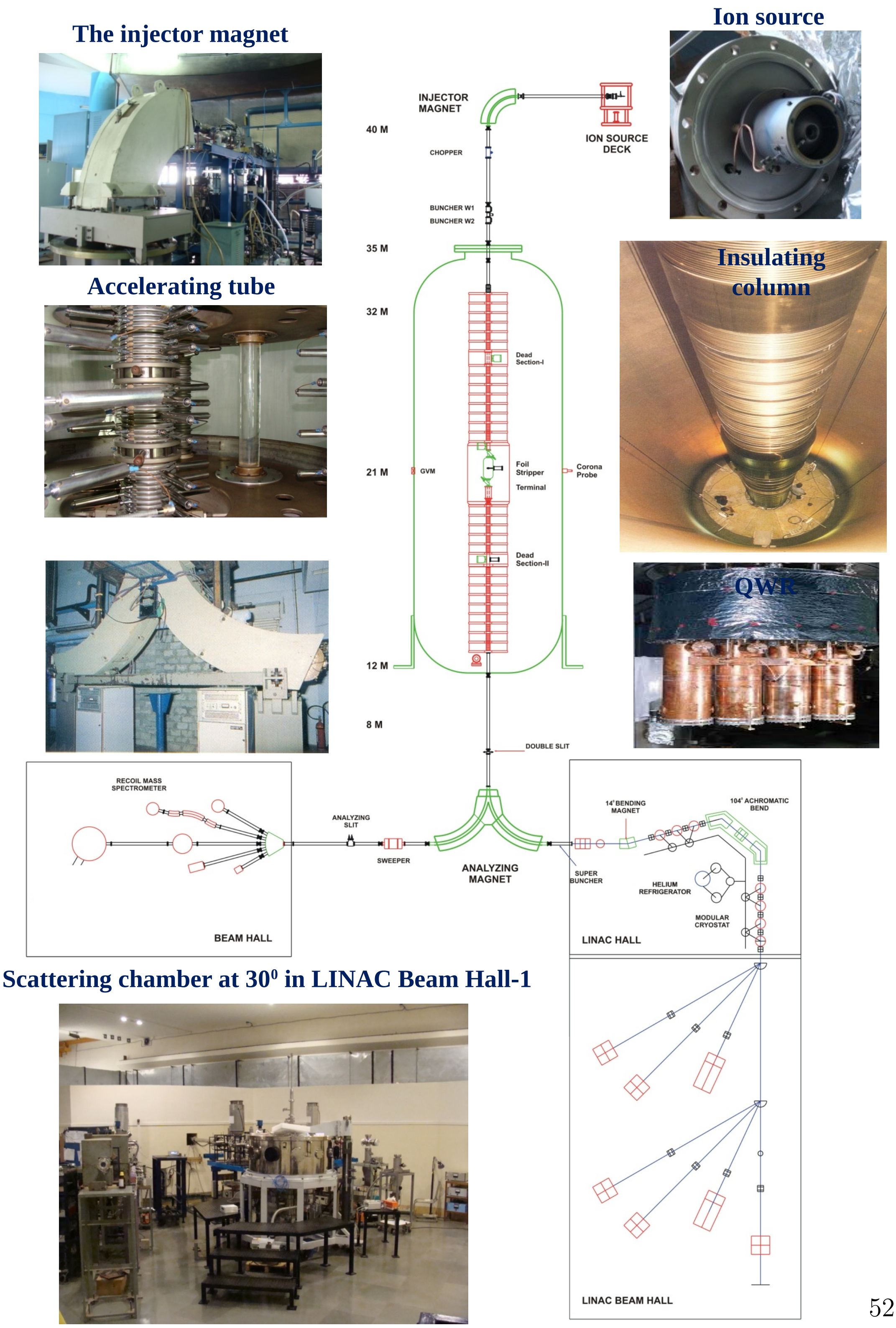

Figure 3.1: A schematic layout of Mumbai Pelletron Linac Facility.

3.2 Scattering chamber

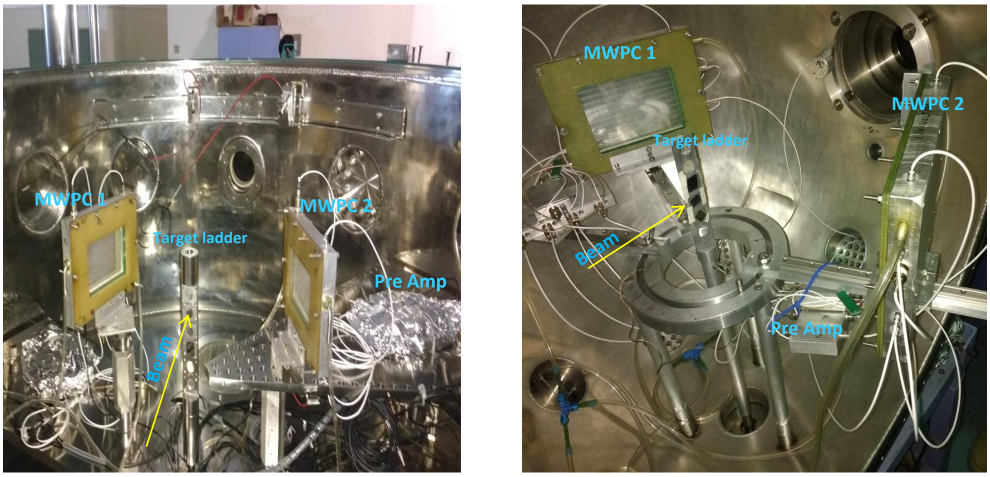

Figure 3.2: (Left)Inside view of scattering chamber at 30° beam line in LINAC Hall-1 PLF, Mumbai and (Right) NAND facility IUAC, Delhi.

The measurements, to detect the fission fragments in coincidence in reactions ^{16}O+^{175}Lu and ^{37}Cl+^{154}Sm, have been carried out in a 1.5 meter diameter general purpose scattering chamber. This scattering chamber has been installed in 30^o beam line of LINAC Hall-1, PLF Mumbai. This chamber has a target ladder (with the provision to mount 6 targets) and two independently rotatable arms to mount detectors. Facility of rotation as well as height adjustment of target ladder along with rotation of the detectors arms from a remote location without interrupting beam using ferrofluidic seals and PLC (Programmable Logic Controller) are available. The measurement for ^{28}Si+^{170}Yb was performed at NAND facility of IUAC, Delhi. This facility consist of a thin walled spherical scattering chamber of 1 m diameter surrounded by 100 liquid scintillators at distance of 1.75 m on a semi-spherical dome (geodesic) structure. An inside view of both scattering chambers is shown in Fig 3.2

3.3 Detection and measurement techniques

The details of technique applied for the detection of fission fragments and measurement of its mass is discussed in the following sections.

3.3.1 Multiwire Proportional Counters for fission fragment detection

First fabricated by G. Charpak at CERN in the year 1968, use of multiwire proportional counter (MWPC) detectors are well established in nuclear physics experiments [72]. Working in proportional region, these detectors exploit the phenomena of ionization when a charged particle passes through a volume of gas. The main principle of operation of these detectors is the collection of the ionized charges across an electric field configuration. Contrary to conventionally available silicon detectors, MWPCs are easier to fabricate with large sizes, unlikely to suffer radiation damage and are exceptionally good for detecting heavy charged particles like fission fragments. Apart from this, MWPCs have higher count rate handling capability along with providing very good timing and position resolutions. Although energy resolution of the MWPC detector is very poor, it provides a clear distinction between light and heavy charged particles. Also, it can be made transparent to unwanted light particles and sensitive only to heavier particles such as fission fragments by adjusting the operating parameters such as gas pressures and voltages on electrodes. An MWPC can be fabricated using three, four or five plane geometry. A detailed working of these different configurations can be found in Refs. [73, 74]. Although, MWPC with four or five plane geometry provide high gain, a three-electrode MWPC provides better timing due to more uniform field. For all the experimental work performed for the present thesis work, a three-electrode geometry MWPC have been used [75]. A schematic diagram of the detector is given in Fig 3.3.

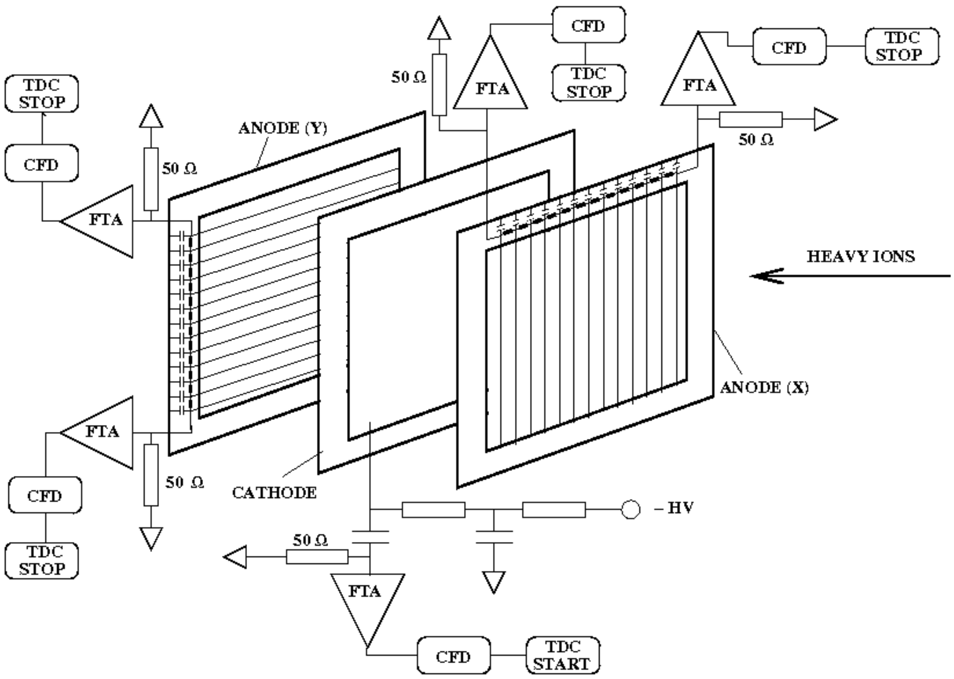

Figure 3.3: Schematic diagram of multi-wire proportional counter used for the detection of the fragments in coincidence [75].

In this geometry, a cathode plane is sandwiched between two position-sensitive anode (X and Y) planes. Placed symmetrically between the two anode (3.2 mm apart), cathode plane is made of a 2μm thick Mylar foil aluminized on both surfaces. The X plane is made of 200 (10μm diameter) gold plated tungsten wires, stretched parallely on a 2.4 mm^2 thick PCB with an active area of 125$\times$75 mm^2. Interwire spacing is 0.63 mm. The Y-plane consists of 30 tin-plated copper strips (perpendicular to the wires of X-plane), 2.2 mm wide with a step of 2.54 mm, made on a printed circuit board. A 1 μm thick Mylar foil at the entrance of the detector is used to isolate the MWPC from chamber vacuum(10^{-6} Torr).This foil is supported by nylon wire. This detector is operated in continuous flow mode with iso-butane gas at $\sim$3-4 Torr pressure. While the position frames are kept at ground potential by terminating both ends of delay lines through 50 Ω resistors, cathode was kept at -420 V to form an uniform electric field for charge multiplication. Position information from X and Y frames are extracted using commercially available rhombus delay line integrated chips (model TZB12-5). In X plane, four wires are shorted and connected to one tap of delay line chip. End to end delay in X and Y-position frames are 100 and 60 ns, respectively. Both X and Y frames have two connections for extracting signals. Using these (X_{left}, X_{right}, Y_{top} and Y_{bottom}) information, the (x,y) position of an event was calculated. The fast timing signals from cathode of both, MWPC1 and MWPC2 were used to obtain the TOF of the fragments with respect to the beam pulse.

3.3.2 Silicon surface barrier detector for beam monitoring

A simple semiconductor detector works as a reverse biased pn junction diode. Since, in a reverse biased p-n junction diode the depletion region is heavily exhausted of charge carriers, any radiation impinging on the detector will result in generation of electron-hole pair giving an electrical signal. A typical surface barrier detector is formed using n-type silicon (semiconductor) with gold (metal). As the Fermi levels of these materials are different, a contact emf arises when the two are put together. This leads to lowering of the band level in semiconductor and thus extension of depletion region entirely into the semiconductor material. By virtue of its good energy resolution, fast timing response, compact geometry and application in charge particle spectroscopy, the use of semiconductor detectors is well known in the field of nuclear and particle physics. In the present thesis work two SSB detectors were used for beam monitoring during the experiment. In each run the total number of counts in the two detectors placed at $\pm 20^{\circ}$ were recorded to check the centrality of the beam.

3.4 Target details

For our experimental measurements, we have used three targets ^{154}Sm, ^{175}Lu and ^{170}Yb which were made in the following ways:-

1. The target of ^{154}Sm (>99%) having thickness 200 μg/cm^2 was electrodeposited on a 550μg/cm^2 thick Al.

2. The target of ^{175}Lu (97.41%) of thickness 280 μg/cm^2 with 150 μg/cm^2 thick Al backing was prepared by vacuum evaporation technique.

3. The target of ^{170}Yb (83.2%) of thickness 200 μg/cm^2 was vacuum deposited on 30 μg/cm^2 C using quartz crystal for thickness monitoring.

These targets were then mounted on the target ladder of scattering chamber.

3.5 Experimental setup

The details of two different experimental layouts utilized in the present work is described in this section.

1. Experiments for measurement of fission fragments mass distribution of ^{191}Au populated via two different entrance channels namely, ^{16}O+^{175}Lu and ^{37}Cl + ^{154}Sm were performed at the BARC-TIFR Pelletron-Linac Facility, Mumbai. Pulsed beams of ^{16}O and ^{37}Cl were bombarded on a 280 μg/cm^2 thick ^{175}Lu (97.41% enriched) target with 150 μg/cm^2 thick Al backing and a 200 μg/cm^2 thick ^{154}Sm ($>$ 99% enriched) target on a 550 μg/cm^2 thick Al backing, respectively. Three beam energies of 83, 80, 72 MeV for ^{16}O and 174, 159, 153 MeV for ^{37}Cl were used for measurement. Effective beam energy at the centre of the target along with other relevant details are given in Table 4.1. Fission fragments were detected using two large area (12.5×7.5 cm^2) position sensitive MWPCs kept at a distance of 24 cm from the target, covering an angle of 30° each, on two separately movable arms of the 1.5 m diameter scattering chamber. To detect both the fragments in coincidence, detectors

were placed around beam axis at θ_1 = -50°, θ_2 = 107° for $^{16}O+^{175}Lu$ with target facing the beam and at $\theta_{1,2}$= ±64° for ^{37}Cl induced reaction with backing facing the beam. To minimize energy loss of the fission fragments and shadowing of detectors, the target was rotated by 30° with respect to beam axis in case of $^{16}O+^{175}Lu$ reaction.

2. Measurement of fission fragments mass distribution of ^{198}Po was carried out at 15UD Pelletron LINAC accelerator facility of IUAC, New Delhi, by bombarding a 200 $\mu g/cm^2$ thick, isotopically enriched (83.2%) ^{170}Yb target, evaporated onto a 22 $\mu g/cm^2$ thick C backing, with ^{28}Si beam of energies 119, 122 and 130 MeV. Effective beam energy at the centre of the target along with other relevant details for this measurement are given in Table 5.1. Using similar experimental setup as described above for ^{191}Au measurement, the fission fragments in coincidence were detected using two large-area (16×11 cm^2) MWPCs located at a distance of 30 cm from the target and at 70° on each side of the beam. At the lowest energy, the beam pulsing was switched off to maximize the current, and thus only the time difference $\Delta T=T_1-T_2$, instead of individual time-of-flights, was recorded.

3.6 Electronics and data acquisition for fission fragment mass distribution

The signals from MWPCs were given to custom made, vacuum compatible pre-amplifiers. These pre-amplifiers are current sensitive, providing very short pulse

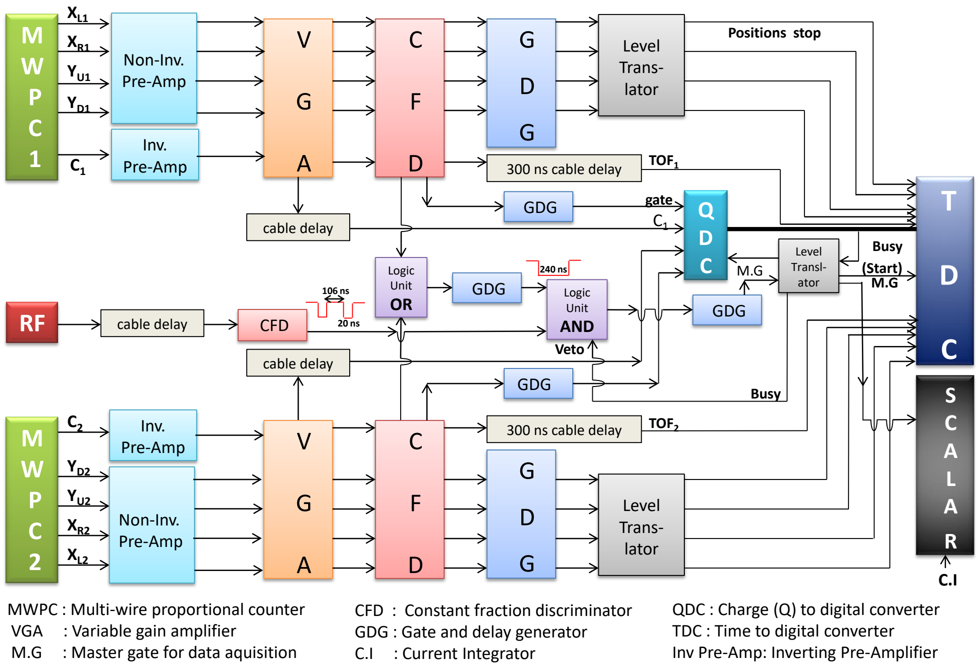

Figure 3.4: Schematic of electronic setup for detection of fission fragments in coincidence.

with rise time of ∼2 ns, required for good timing information. The output of the pre-amplifiers were given to variable gain amplifiers for further amplification and shaping of the signals. Master gate was generated by making logic AND between RF (beam) and OR of both cathod signals. Individual positions and timing signals were delayed using GDG to measure time of arrival and position of the detected fragments with respect to beam. The energy loss of the fragments inside the detector volume (ΔE1, ΔE2) were also obtained using charge to digital converter (QDC). A schematic diagram of electronic setup for detection of fission fragments in coincidence is shown in Fig. 3.4.

For timing calibration of cathode signal, a time calibrator was used to determine the slope of the TDCs and the offset were obtained from the elastic peak. The position signals were calibrated using known dimensions of active area of the MWPC detectors and 2D plots of X and Y positions. These calibrated position and timing informations were further used to obtain the values of scattering angle (θ), azimuthal angle (ϕ), and to calculate the fragment velocity vector (v) on event-by-event basis.

3.6.1 Folding angle calculation

In case of the spontaneous fission, in order to conserve the total angular momentum, emission of fission fragments takes place at 180° with respect to each other. In the event of fusion fission process, where target is at rest and there is partial or complete transfer of momentum from projectile into the target, fragments are emitted at a certain angle ($<$180° in lab frame) with respect to each other. This relative angle between the two fragments is called folding angle (θ_1+θ_2). Where, $\theta_{1,2}$ are the emission angles of first and second fragment respectively. As the momentum transfer from projectile to the CN increases, the angle between the two emitted fission fragments decreases. Considering the energetics, two MWPCs were kept at folding angle in each measurement to detect the fragments in coincidence. However the competing process, namely the direct reaction process can also result in the fission even before formation of a compound nucleus. The fissionable nuclei produced in the direct reaction have very small linear momentum component along the beam axis. Hence, fission fragments following direct processes will move along a nearly collinear axis($\sim$ 180°). A correlation plot between folding angle and azimuthal angle ($\phi_1+\phi_2$) is an efficient tool to separate the fission events originating from these two competing processes [52].

3.6.2 Measurement of fission fragment mass distribution

The kinematics of a heavy ion induced complete fusion fission process is shown in Fig. 3.5. There are two methods for the measurement of fragment masses. In case of pulsed beam, one can measure the velocity of the detected fragments (v_1,v_2) separately. By calculating the corresponding velocity vectors in the centre of mass frame (V_1,V_2) the mass split can be determined as $M_R=V_1/(V_1+V_2)$. Here, M_R is ratio of second fragment mass to the sum of both fragment masses. This method has been called the kinematic coincidence method [76]. Contrary to pulsed beam, in case of a continuous projectile beam, it is not possible to measure the fragment time of flight separately. For this case, the fragment masses can be determined from the time difference between the MWPC detector signals. This is called the Time of flight difference method [77]. A detailed mathematical analysis of both the methods is described below.

1. Kinematic coincidence method

The position calibrations for both the detectors were performed using the known positions of the edges of the illuminated areas of the detectors during the experiment. The calibrated positions (x and y) were then converted to polar angles θ and ϕ. For time calibration, while slope was obtained using time calibrator, corresponding offsets were calculated using elastic peak positions and kinematics. Fragment velocities in the laboratory frame ($v_{1,2}$) were re-constructed using these

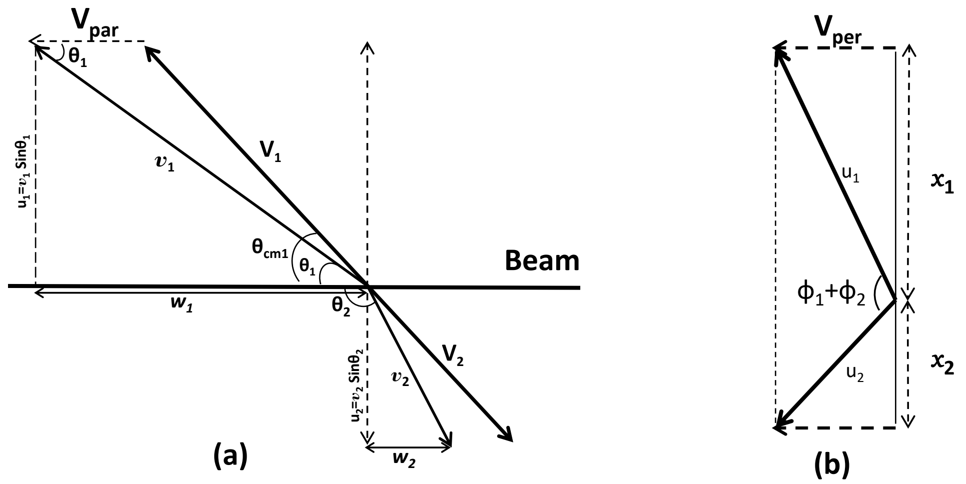

Figure 3.5: Kinematic diagram for heavy ion induced fusion fission process.

time of flight, θ and ϕ informations. Considering that the two velocity vectors and the beam axis are coplanar as shown in Fig 3.5 (a), the measured velocity vectors can be decomposed into two components, one parallel and other perpendicular to the beam axis. The former is given by $\mathrm{w}_i = v_i \cos\theta_i$, the latter by $\mathrm{u}_i = v_i \sin\theta_i$. Prescission particle evaporation will negligibly effect the velocity vector due to its isotropic nature. Thus the two fragments are taken as colinear in the center-of-mass frame with velocity given by V_i. Using Fig 3.5 (a),

$$\mathrm{w}_1 - \mathrm{V}_{\mathrm{par}} = \mathrm{V}_1 \cos\theta_{\mathrm{cm1}} \tag{3.1}$$

Since, $V_1 \sin\theta_{cm1} = u_1$

$$\mathrm{w}_1 - \mathrm{V}_{\mathrm{par}} = \frac{\mathrm{u}_1}{\sin\theta_{\mathrm{cm1}}} \cos\theta_{\mathrm{cm1}} \tag{3.2}$$

Similarly,

$$\mathrm{w_2 - V_{par}} = \frac{-\mathrm{u_2}}{\mathrm{sin}\theta_{\mathrm{cm1}}}\mathrm{cos}\theta_{\mathrm{cm1}} \tag{3.3}$$

$$\frac{\mathrm{w_1 - V_{par}}}{\mathrm{w_2 - V_{par}}} = -\frac{u_1}{u_2} \tag{3.4}$$

which leads to

$$V_{par} = \frac{u_1\mathrm{w_2} + \mathrm{u_2 w_1}}{u_1 + u_2} \tag{3.5}$$

from Fig 3.5 (b),

$$(x_1 + x_2)^2 = {u_1}^2 + {u_2}^2 - 2u_1u_2cos(\phi_1 + \phi_2) \tag{3.6}$$

As, ${x_1}^2 = {u_1}^2 - {V_{per}}^2$ and ${x_2}^2 = {u_2}^2 - {V_{per}}^2$ substituting these values of $x_{1,2}$ in above equation, one can obtain

$$V_{per} = \pm\frac{u_1u_2sin(\phi_1 + \phi_2)}{\sqrt{{u_1}^2 + {u_2}^2 - 2u_1u_2cos(\phi_1 + \phi_2)}} \tag{3.7}$$

In principle, V$_{par}$ should be equal to the calculated center-of-mass velocity for the collision V$_{c.m}$ if fission is taking place after complete absorption of the projectile by the target i.e when the full momentum of the projectile is transferred. However, deviations from binary kinematics due to emission of light particles perturbs the fission fragment vectors, resulting in a significant spread in V$_{par}$. To avoid this problem, the fragment velocities in the center-of-mass frame V$_i$ were evaluated taking V$_{par}$ to be fixed at the value expected for complete fusion V$_{c.m}$.

$$V_i = \sqrt{{v_i}^2 + {V_{c.m}}^2 - 2v_iV_{c.m}cos(\theta_i)} \tag{3.8}$$

where,

$$V_{c.m} = \sqrt{\frac{A_p}{A_{cn}^2} E_p} \tag{3.9}$$

if A_1 and A_2 are the masses of detected fission fragments, then from momentum conservation

$$A_1 V_1 = A_2 V_2 \tag{3.10}$$

This leads to

$$\frac{A_2}{A_1 + A_2} = \mathrm{M_R} = \frac{\mathrm{V_1}}{\mathrm{V_1} + \mathrm{V_2}} \tag{3.11}$$

The kinetic energy of the fragments were calculated as,

$$E_i = \frac{1}{2} A_i V_i^2. \tag{3.12}$$

As described in ref [52], for fission fragments originating from direct transfer reactions i.e after partial transfer of linear momentum from projectile to the target, the $\mathrm{V}_{par}/\mathrm{V}_{c.m}$ will be either greater than 1 or less than 1 depending upon the beam energy. This makes direct reaction events easily separable from full momentum transfer events using a correlation plot between $\mathrm{V}_{par}/\mathrm{V}_{c.m}$ versus V_{per}. Therefore, for each measured data in the present thesis work, this correlation has also been utilized to investigate the presence of non full momentum transfer events.

2. Time of flight difference method

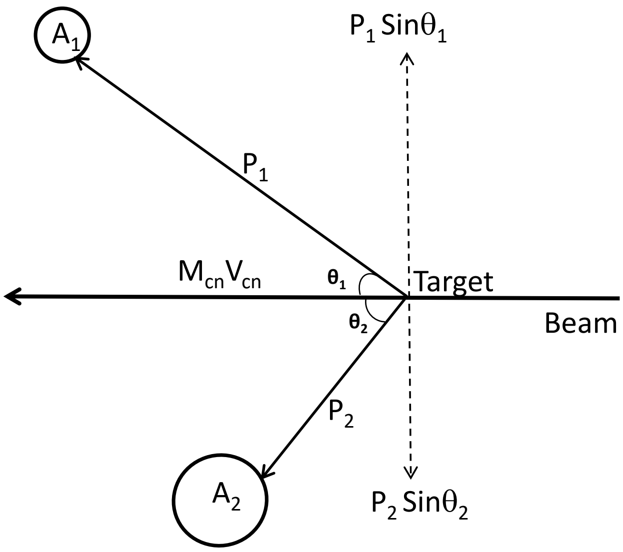

Figure 3.6: Diagram representing the fusion-fission kinematics.

Fig 3.6 shows another simplistic kinematic presentation for fusion fission process. Let T_1 and T_2 are flight times of the fragments for the distances d_1 and d_2 respectively such that P_1 and P_2 are their corresponding linear momenta in the laboratory frame. According to conservation of linear momentum,

$$P_1 cos\theta_1 + P_2 cos\theta_2 = M_{cn}V_{cn} \tag{3.13}$$

$$P_1 sin\theta_1 = P_2 sin\theta_2 \tag{3.14}$$

leading to,

$$P_1 = \frac{M_{cn}V_{cn}}{cos\theta_1 + sin\theta_1 cot\theta_2} \tag{3.15}$$

and

$$P_2 = \frac{P_1 sin\theta_1}{sin\theta_2} \tag{3.16}$$

As,

$$T_1 - T_2 = \frac{d_1}{v_1} - \frac{d_2}{v_2} = \frac{d_1 A_1}{P_1} - \frac{d_2(M_{cn} - A_1)}{P_2} \tag{3.17}$$

resulting in,

$$A_1 = \frac{(T_1 - T_2) + \delta t_0 + M_{cn}\frac{d_2}{P_2}}{\frac{d_1}{P_1} + \frac{d_2}{P_2}} \tag{3.18}$$

and

$$A_2 = M_{cn} - A_1 \tag{3.19}$$

Here, δt_0 is the electronic time delay between the two timing signals. Since, energy of the detected fragment can be obtained as

$$E_i = P_i^2/2A_i \tag{3.20}$$

In this technique, time of flight of the fragments can be calculated as,

$$T_i = \frac{d_i}{\sqrt{2E_i/A_i}} \tag{3.21}$$

3.7 Energy loss of fission fragments inside the target material

In fission measurements, the velocity and energy information of the fission fragments (FFs) must be precise in order to get correct estimation of FFs mass and kinetic energy distribution. In the experiments where nuclear reactions are studied using lighter projectile beam with E_p<10 MeV/u on stable and heavier target, the reaction products loose substantial amount of energy while passing through various stopping materials before its detection. The precision of such measurements is limited by the uncertainty of corrections for energy loss of the particles in target material,detector window etc. Among these reaction products, FFs desire special attention because of its remarkably high energy loss even in very thin layers of any solid material. In our measurements, as described in section 3.4, the typical thickness of target and backing lied in the range of 30 μg/cm^2 to 550 μg/cm^2 and thus the materials like backing of the target and target itself became a source of significant energy loss for the fission fragments. In the present thesis work, we used SRIM code for estimation of energy loss of the fission fragments inside target and backing materials [32, 33].

The classical expression that describes the electronic stopping power of an ion with charge Z_1 and velocity v is

$$-\frac{dE}{dx} = \frac{4\pi e^4 {Z_1}^2}{m_e v^2} N Z_2 L \tag{3.22}$$

where N and Z_2 are the density and atomic number of target atoms and L is the stopping number [87].

As the range of the fragment inside the stopping material is decided by its dE/dx behaviour. In the present work, E/A versus range characteristic of the fragments is exploited to estimate the energy loss of the fragments inside the stopping material. Primarily, the characteristic E/A versus range curve was obtained for each possible fragment Z value using SRIM. According to the kinematical requirements, a broad range of fragment initial energy i.e 10 MeV to 170 MeV is

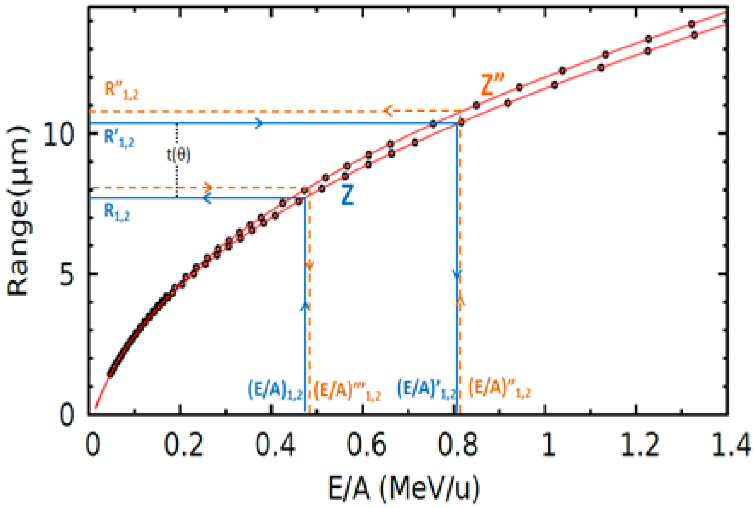

Figure 3.7: Energy per nucleon versus range characteristic obtained using SRIM for two heavy elements with charge Z and Z".

considered for the SRIM calculations. Fig. 3.7 shows E/A versus range behaviour for two different elements with charge Z and Z". The range values (R) were then fitted using a function (shown by red line) defined as,

$$R = \left(a \left(\frac{E}{A} \right)^b + c \left(\frac{E}{A} \right)^d + e \right)^f \tag{3.23}$$

For each element, all coefficients, a,b,c,d,e,f were recorded for purpose of interpolation. Using this function, for each Z, an E/A versus R and R versus E/A table was also constructed in steps of fine intervals of 0.03 MeV/u and 0.01 μm respectively.

A typical experimental setup for measuring heavy ion induced fusion fission reaction is shown in Fig 3.8(a). As shown in Fig. 3.8(b), assuming that the reaction took place at the centre of the target, the distance travelled by the fragment inside the target material before reaching the MWPC can be obtained as t(θ)=0.5T/cosθ. where, T is thickness of the target. Let, E_0 represents the energy of the fragment with which it was originated after the fission reaction occured at the centre of the target. E is the energy of the fragment after coming out of the target material and measured using calibrated time of flight and position informations as,

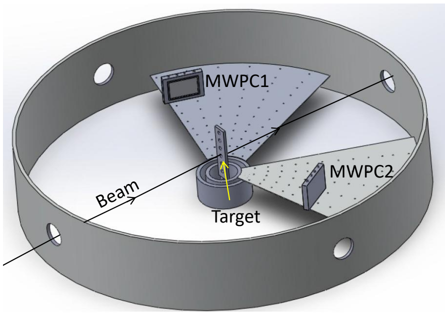

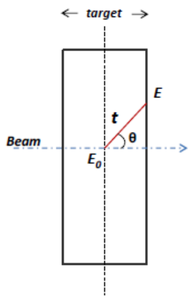

Figure 3.8: (a)A typical experimental setup for measuring heavy ion induced fusion fission reaction and (b) A sketch to explain the path traveled by the fragment inside the target material (red line) and its energy at point of nuclear interaction (E_0) and after coming out of the target (E).

$$E_i = \frac{1}{2} A_i {v_i}^2 \,, \qquad E_i = P_i^2/2A_i \,, \tag{3.24}$$

for kinematical coincidence method and time of flight difference method respectively.

Thus, as shown in Fig. 3.7, E/A is the first measured uncorrected velocity information of the fragment. The charge of the fragments, Z_i is deduced by applying unchanged charge density assumption (UCD) as,

$$Z_i = \frac{Z_{cn}}{A_{cn}} A_i \tag{3.25}$$

where, Z_{cn} and A_{cn} are charge and mass of the fissioning nucleus. For this fractional Z value and E/A, the range of the fragment R, shown in Fig. 3.7 was obtained by applying two dimensional interpolation between the characteristic curves obtained for Z+1 and Z-1. As the fragment have traversed a distance of t(θ) inside the target material, its actual range before loosing energy inside the target is R'= R+t(θ). Thus, by again using E/A versus R and R versus E/A tables and performing two dimensional interpolation between the characteristic curves obtained for Z+1 and Z-1, the first corrected velocity of the detected fragment (E/A)' was obtained. This process is shown by blue continuous line in Fig. 3.7.

Using this corrected lab velocity (E/A)', the calculation for corresponding corrected velocity in the centre of mass frame V was performed. Further, this corrected V was used to get our first estimation of correct mass of the fragment A', as explained in Eq. 3.11. The resulting velocity of the fragment becomes (E/A)". Associated Z' for this corrected estimation of fragment mass was again obtained using UCD assumption described earlier.

In order to check the accuracy of the applied correction, the transmitted (E/A)"' for incident (E/A)" was back calculated in the same way. This process is shown by orange continuous line in Fig. 3.7. If the difference between the previous estimation and back calculated value of E/A exceeds 0.1%, the entire process was repeated by adding the difference in previous estimation i.e (E/A)". A flow chart, explaining the process of energy loss correction when fragment masses are calculated using kinematical coincidence method is shown in Fig. 3.9.

In the time of flight difference method, the calculated fragment mass prin-

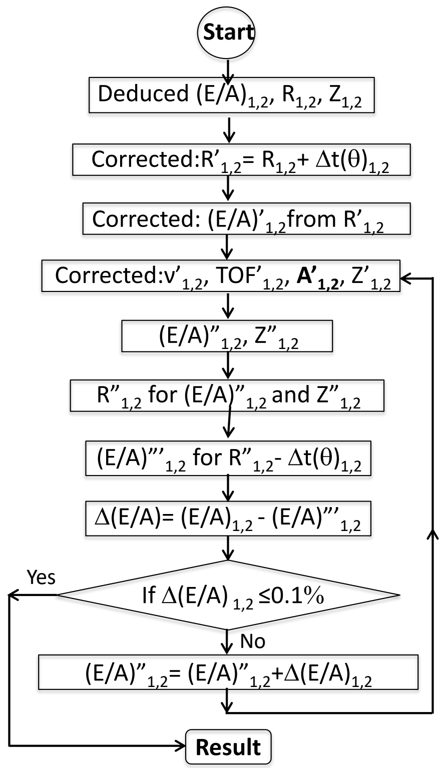

Figure 3.9: Flow chart for energy loss correction when mass is deduced using kinematical coincidence method.

cipally depend on the difference between time of arrival of the two fragment in detector. Hence, in this case, the change in *time of flight difference* between the fragments (ToF_d') was calculated by correcting individual time of flight of the fragments (T_i obtained using Eq. 3.21), as described earlier. By comparing the fragment mass obtained after this correction with the previous estimated value, the correct fission fragment mass was obtained in an iterative way. Flow chart, explaining the process of energy loss correction, when fragment mass is calculated using time of flight difference method is shown in Fig. 3.10.

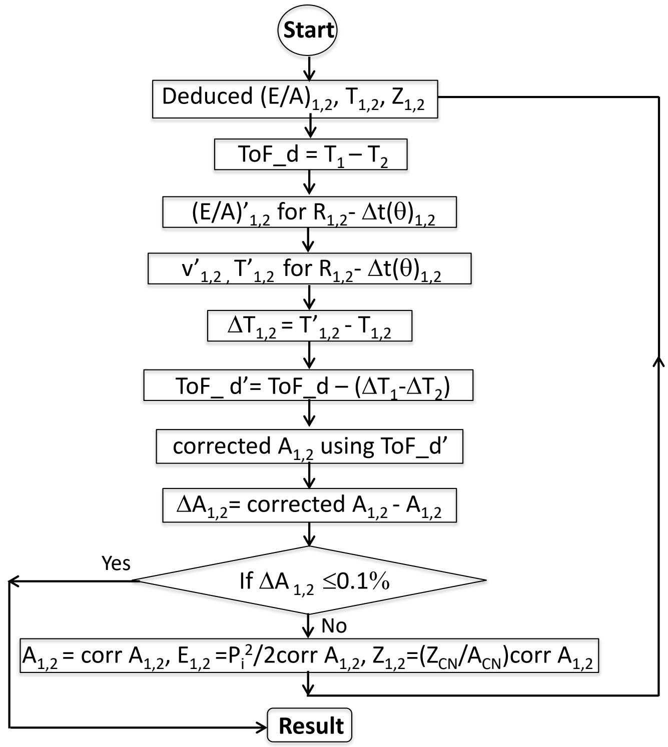

Figure 3.10: Flow chart for energy loss correction when mass is deduced using time of flight difference method.

As the ion pass through an absorber, there is increase in the peak width of the transmitted ions in comparison to that of incident ions due to the associated straggling. Fig. 3.11 shows energy loss corrected and uncorrected fission fragment mass distributions obtained for 130 MeV ^{28}Si beam on ^{170}Yb target, using kinematical coincidence method and time of flight difference method respectively. Both the correction techniques are in agreement with each other and results in $\sim$2% reduction in mass distribution width after correction. This small amount of correction was expected in this measurement as the target was thin (200 μg/cm^2). In both the techniques, as the maximum number of iterations remains three, a fast convergence is observed.

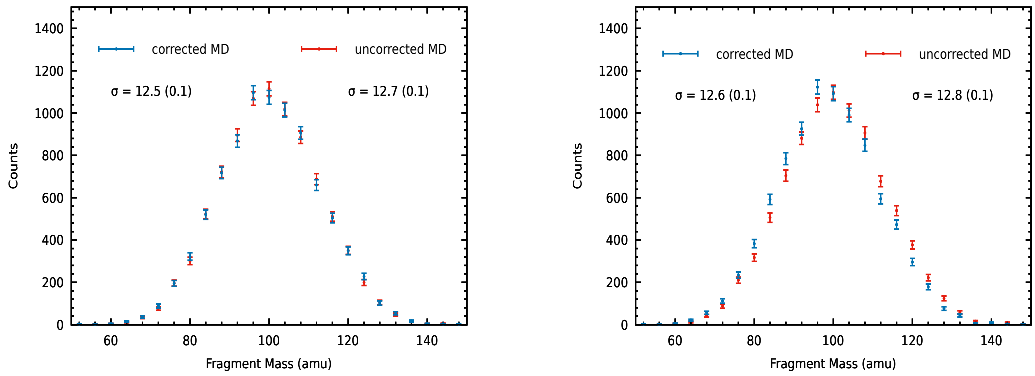

Figure 3.11: (Left) Energy loss corrected and uncorrected FFs mass distributions obtained for 130 MeV ^{28}Si beam on ^{170}Yb target, in case of kinematical coincidence method and (Right) time of flight difference method.

4

Investigation of entrance channel dependence

4.1 Introduction

Although β-delayed fission and electromagnetic-induced fission are the best approaches to attain low excitation energy required for studying fragment shell effects on fission dynamics, the associated experimental requirements with these methods are extremely challenging. Number of fissioning systems accessible from β delayed fission are limited due to primary requirement of non zero β decay branching ratio along with the condition of $Q_\beta > B_f$ [18]. Electromagnetic-induced fission can remove this problem of limited accessible systems, however, pre-actinide nuclei, being in the region of extremely low fissility systems call for very long beam time. Under this scenario, the route of heavy ion induced fusion fission reactions has been exploited to study the mass-asymmetric fission for neutron deficient nuclei in the sub-Pb region.

Heavy-ion induced fusion fission reactions are advantageous in terms of providing the data to study evolution of fragment mass distribution with excitation energy. Also, it gives an opportunity to study the link between the pre-actinide and the actinide region. However, use of heavy-ion beams not only brings in higher excitation energy and angular momentum (l), it also opens the possibility of quasi-fission (QF), which might complicate the interpretation of the experimental observations substantially. As discussed briefly in section 1.5, QF is a non-compound (non-equilibrated) nuclear process that strongly depends on the entrance channel parameters like charge product (Z_pZ_t), deformation of the colliding nuclei, shell closure and neutron excess in addition to the compound nucleus fissility. Since the mass of reaction products coming from this non-equilibrated process can severely overlap with the mass of fragments originating from complete fusion fission, in many cases, depending on entrance channel properties QF can mimic the presence of multi-modal CN fission. Investigation of the role of QF is thus essential for interpreting the sub-Pb data unambiguously and accurately model the excitation energy dependence of microscopic effects. Ignoring this aspect, and directly correlating the deviations from single Gaussian distribution with the microscopic effects may lead to ambiguity in the inferred multi-modal fission in sub-Pb region.

In the present work, we measured the fission fragment mass distribution of ^{191}Au, populated using two different entrance channel ^{16}O+^{175}Lu (α=0.832, Z_pZ_t= 568) and ^{37}Cl+^{154}Sm (α=0.612, Z_pZ_t=1054) having mass asymmetry (α) on either side of Businaro-Gallone point (α_{BG} =0.823) to disentangle the role of shell effects and dynamics in the entrance channel [32].

4.2 Data analysis & Results

The fission events were selected by putting two dimensional gates in the TOF difference vs. energy loss spectra shown in Fig. 4.1(a-b).

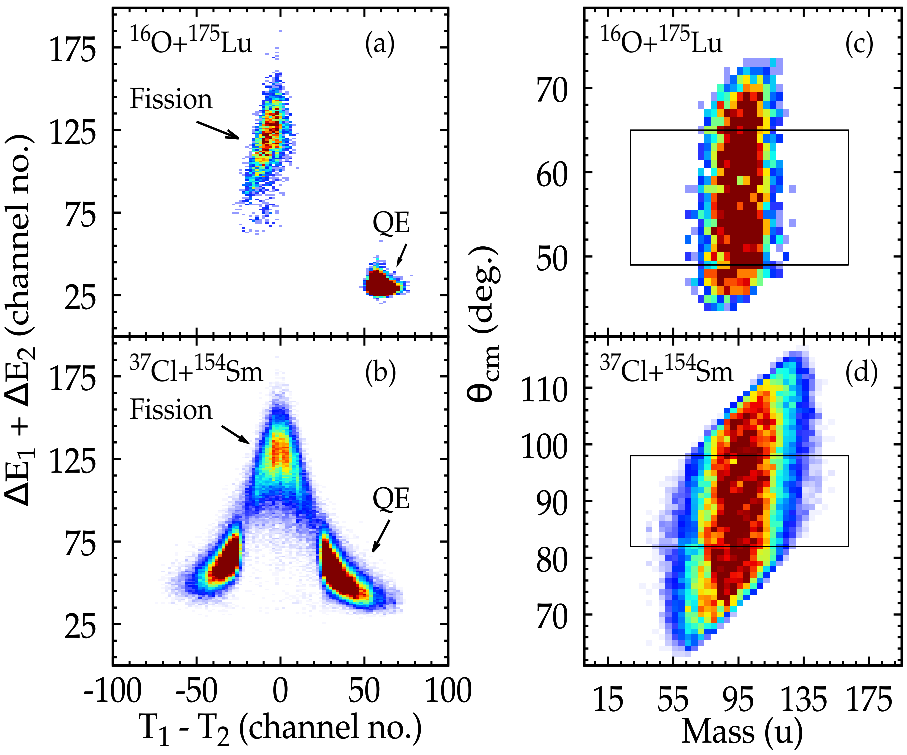

Figure 4.1: Time of flight difference ($T_1 - T_2$) vs energy loss ($\Delta E_1 + \Delta E_2$) spectra used to separate fission from quasi-elastic (QE) events for (a)$^{16}O+^{175}Lu$ at $E_{lab.}$=82.8 MeV and (b)$^{37}Cl+^{154}Sm$ reaction at $E_{lab.}$=166.4 MeV. The corresponding mass-angle distributions along with the angular cut (rectangular box) used to obtain the mass distributions are shown in (c) and (d), respectively.

The correlations between the folding and azimuthal angles as well as between parallel and perpendicular components of the velocity onto the beam axis for the selected fission events, shown in Fig. 4.2, confirmed the absence of transfer induced (incomplete momentum transfer) events at all measured energies.

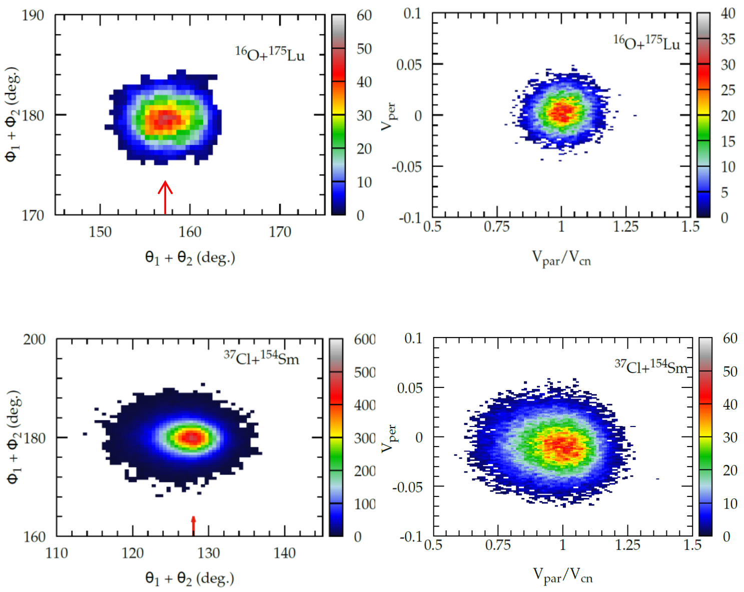

Figure 4.2: A typical correlation plot of the folding angle (θ_1+θ_2) vs. azimuthal angle (ϕ_1+ϕ_2) as well as of V_{par}/V_{cn} vs. V_{per} for the selected fission fragments for (a)^{16}O+^{175}Lu at E_b=82.8 MeV and (b)^{37}Cl+^{154}Sm reaction at E_b=166.4 MeV. The position of folding angle is marked with arrow.

Fragment mass distributions were deduced using the TOF difference method discussed in section. 3.6.2. The mass resolution (σ) was estimated from the elastic peak to be 2.8 u. As discussed in section. 3.7, small corrections in the fragment mass due to their energy loss in the target and backing were obtained on an event-by-event basis in an iterative manner, taking the energy loss information from SRIM [79] for all the possible fragments. Change in the mass distribution widths after energy loss corrections were found to be about 4.5% for ^{16}O+^{175}Lu and 2% for ^{37}Cl+^{154}Sm reactions. Typical mass-angle correlation plots for the two systems are shown in Fig. 4.1(c-d). No significant mass angle correlation has been observed for both the systems at all energies studied. Mass angle correlation was also not expected as the entrance channel mass asymmetry (or Z_pZ_t) of the present systems are below the experimentally determined threshold only above which mass angle correlation is observed [50]. In order to remove the bias due to geometrical acceptance of the detection setup, the fission fragment mass distributions were obtained by projecting the mass angle correlations with angular cut of $\theta_{1,cm}$ from 49° to 65° for ^{16}O+^{175}Lu system and $\theta_{1,cm}$ from 81° to 99° for ^{37}Cl+^{154}Sm system (shown as rectangular box in Fig. 4.1(c-d)).

4.3 Mass Distributions

The experimental mass distributions measured for ^{16}O+^{175}Lu and ^{37}Cl+^{154}Sm reactions are shown in Fig. 4.3 and Fig. 4.4 respectively.

As discussed in section 1.2, for a purely macroscopic potential energy surface, the fragment mass distribution of CN fission is expected to be a Gaussian in shape. Even though the overall mass distribution could be fitted well with a Gaussian (black dash dot line), deviations were observed at the middle of the distribution in all cases. To investigate the possible presence of microscopic effects, GEF [61] (described in section. 2.3.3) calculations were performed at all measured energies. This model calculates the observables of spontaneous fission as well as CN fission for a given excitation energy (E^*_{CN}) and average angular momentum ($\langle\ell\rangle$). The $\langle\ell\rangle$ values for both the systems were calculated using the coupled channels code

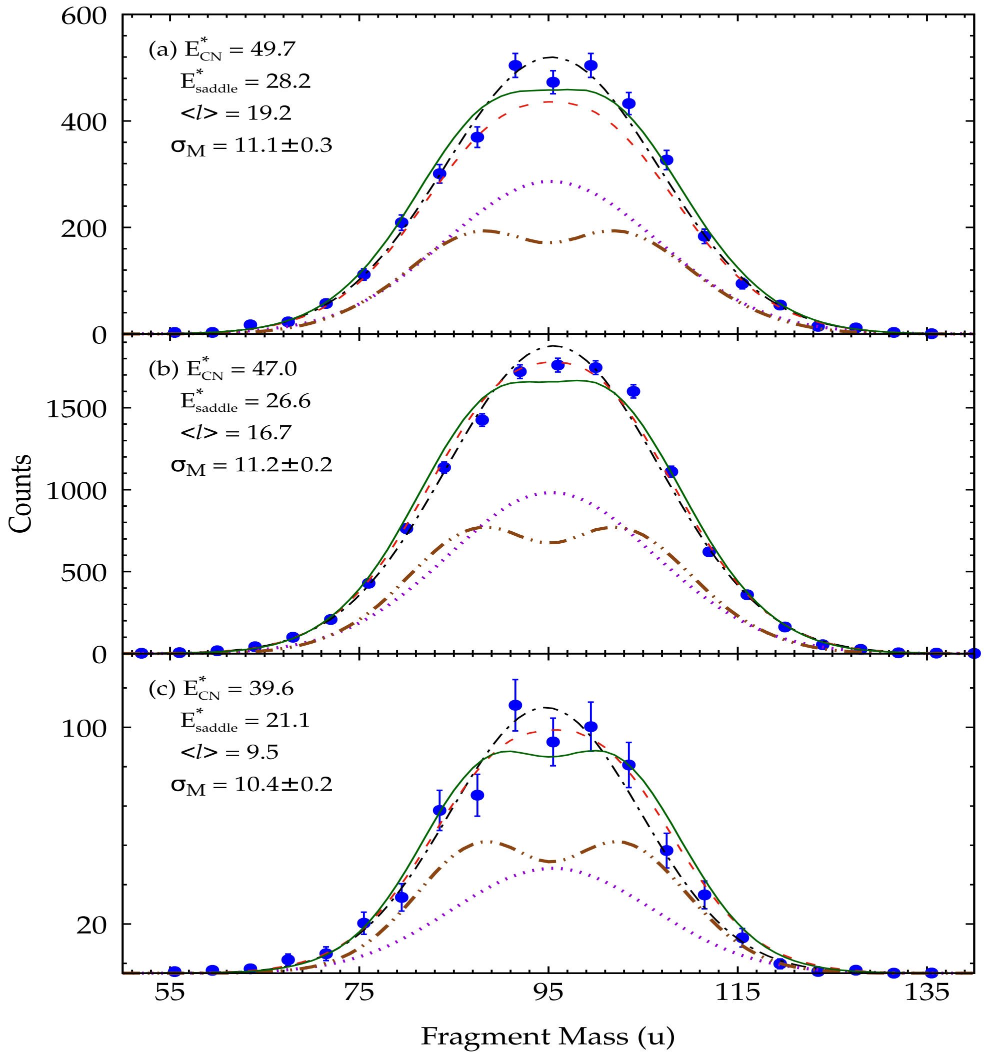

Figure 4.3: The experimental fission fragment mass distributions (blue filled circles) for reaction $^{16}O+^{175}Lu$ reaction at different excitation energies are compared with the predictions of total (green continuous line) along with the symmetric (purple dotted) and asymmetric (brown dot-dot-dash) components of GEF code [61]. The sum of 25% asymmetric and 75% symmetric components are shown in red dashed line. The black dash-dotted lines are the single Gaussian fits. The excitation energy of the compound nucleus (E^*_{CN}) and the effective excitation energy above the fission barrier ($E^*_{B_f}$) (see text) in MeV are noted along with the estimated average angular momentum ($\langle l \rangle \hbar$) and width (σ_M) of the single Gaussian fits. For $^{37}Cl+^{154}Sm$ reaction, the differences between the measured distributions and the GEF predictions are also shown as filled triangle along with sum of two Gaussian fits (green dashed lines).

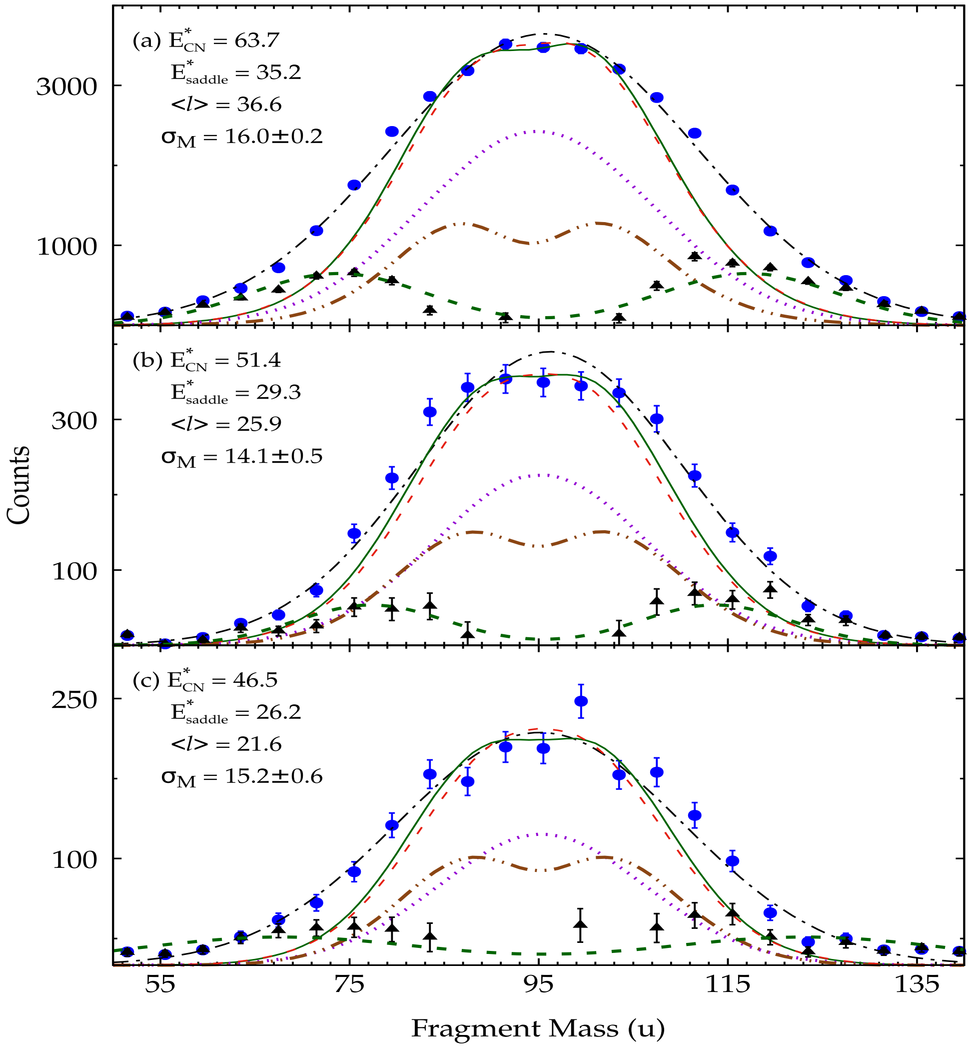

Figure 4.4: Same as Fig 4.3 except for ^{37}Cl+^{154}Sm reaction. The differences between the measured distributions and the GEF predictions are also shown as filled triangle along with sum of two Gaussian fits (green dashed lines).

CCFULL [42] (described in section. 2.1.1). The fusion excitation functions for reactions measured in the present work are not available. To estimate the $\langle \ell \rangle$ for ^{16}O+^{175}Lu reaction, the fusion data for similar system, ^{16}O+^{176}Yb [96] was scaled according to Coulomb parameter $Z_p Z_t/(A_p^{1/3} + A_t^{1/3})$. Analogous calculation was done in case of ^{37}Cl+^{154}Sm with the reference fusion data of ^{40}Ar+^{154}Sm [97]. In the CCFULL calculations to reproduce these scaled data, the vibrational states of projectile were coupled with the rotational states of target in both the reactions. The estimated values of $\langle \ell \rangle$ are given in Table 4.1.

Table 4.1: Effective beam energies at the centre of the target in the laboratory frame ($E_{lab.}$), centre of mass energy (E_{cm}), excitation energy of compound nucleus (E^*_{CN}), estimated average angular momentum ($\langle \ell \rangle$), mean square angular momentum ($\langle \ell^2 \rangle$), temperature at saddle point (T) and the width of the experimental mass distributions relative to the CN mass ($\sigma^{expt.}_{M_R}$) for both the reactions studied.

$E_{lab.}$ (MeV)	E_{cm}	E^*_{CN}	$\langle \ell \rangle$ ($\hbar$)	$\langle \ell^2 \rangle$	T (MeV)	$\sigma^{expt.}_{M_R}$
^{16}O+^{175}Lu(V_B=68.7 MeV)						
71.7	65.7	39.6	9.5	119.5	0.984	$0.0540 \pm 0.13 \times 10^{-2}$
79.8	73.1	47.0	16.7	338.2	1.086	$0.0586 \pm 0.08 \times 10^{-2}$
82.8	75.8	49.7	19.2	436.9	1.111	$0.0582 \pm 0.15 \times 10^{-2}$
^{37}Cl+^{154}Sm(V_B=121.6 MeV)						
145.0	116.9	46.5	21.6	553.6	1.055	$0.083 \pm 0.13 \times 10^{-2}$
151.1	121.8	51.4	25.9	784.5	1.100	$0.074 \pm 0.15 \times 10^{-2}$
166.4	134.2	63.7	36.6	1561.5	1.150	$0.084 \pm 0.06 \times 10^{-2}$

A good agreement between the measured mass distributions and the model predictions were observed for the system ^{16}O+^{175}Lu (see Fig. 4.3). Particularly, the observed deviation from a Gaussian shape at the middle of the distribution is also reproduced well by the model, in which microscopic corrections are already incorporated empirically. The GEF predicts 60%, 49% and 45% of asymmetric

compound nuclear contributions for E^*_{CN} = 39.6, 47.0 and 49.7 MeV, respectively. The experimental data is found to be less sensitive to the relative weight of the asymmetric to symmetric component. This might be due to the similar overall widths of the predicted symmetric (purple dotted line) and asymmetric (brown dot-dot-dash line) components. Use of 25% asymmetric and 75% symmetric (red dashed line) contributions, best fitted the ^{16}O+^{175}Lu data by reducing the χ^2 by only a factor of 2 as compared to the GEF predicted percentages.
In case of ^{37}Cl+^{154}Sm reaction, Fig. 4.4, apart from showing similar deviations from Gaussian shapes at the middle, the mass distributions were found to be broader than those for the more asymmetric combination ^{16}O+^{175}Lu. The obtained mass distribution widths (relative to CN mass, σ_{MR}) plotted with respect to CN excitation energy E^*_{CN} for ^{16}O+^{175}Lu and ^{37}Cl+^{154}Sm reactions are shown in Fig. 4.5.

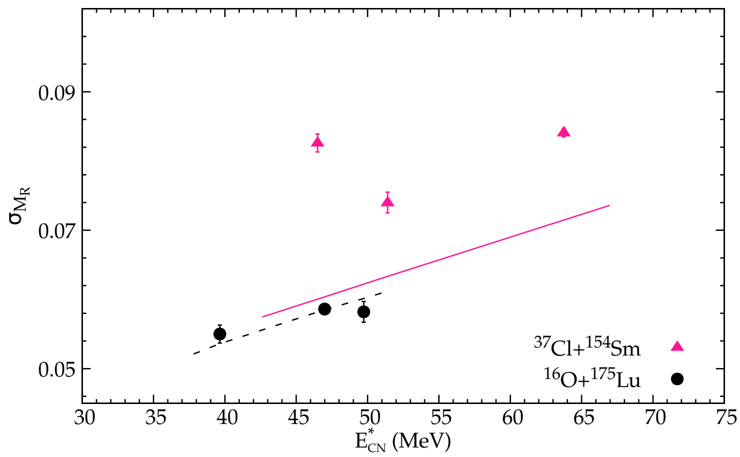

Figure 4.5: Variation of experimental mass distribution widths (relative to CN mass, σ_{MR}) with respect to excitation energy of compound nucleus, E^*_{CN} for ^{16}O+^{175}Lu and ^{37}Cl+^{154}Sm reactions. The dashed line is the fit using the Eq. 4.1 to the data for ^{16}O+^{175}Lu system assuming compound nucleus fission only and the solid line is the estimated widths for ^{37}Cl+^{154}Sm system using the same parameters.

Such enhancement in fragment mass distribution width can be due to larger angular momentum involved in the case of heavier projectile as well as due to the presence of QF component. When compared at similar excitation energy, the estimated $\langle \ell \rangle$ values for ^{37}Cl induced reactions are found to be $\sim 6\hbar$ higher than those for ^{16}O induced reactions. For ^{16}O+^{175}Lu system, with a variation of 10 MeV in E^*_{CN} and $10\hbar$ in $\langle \ell \rangle$, there is only 6.5% change in the measured mass width. Hence, the observed increase in mass distribution width for ^{37}Cl induced reactions ($\sim$30%) cannot come from $\sim 6\hbar$ difference in angular momentum. This observation ruled out a significant role of ℓ in increasing the width for ^{37}Cl+^{154}Sm as compared to ^{16}O+^{175}Lu system at similar E^*_{CN} and revealed the presence of QF in the former case. Also, the measured mass distributions for ^{37}Cl induced reactions are found to be much broader than the distributions predicted by GEF. GEF code, which inherently takes care of $\langle \ell \rangle$ of the fissioning system while calculating fission fragment mass distribution, explained the measured distributions for ^{16}O induced reactions but failed to reproduce the distributions for ^{37}Cl induced reactions. This discrepancy confirmed the presence of QF in case of heavier projectile. The difference between the measured distributions and the GEF predictions for ^{37}Cl+^{154}Sm reactions were also calculated to estimate the extent of QF contributions. The GEF predictions were normalized to experimental data around the center of the distributions, assuming no QF contributions for those fragments. These differences, plotted as filled triangle along with sum of two Gaussian fits (green dashed lines) in Fig. 4.4 found to contribute about 20% of the total counts at all three energies and peak around fragments of mass 74±1 u and 117±1 u. For most of its parts, area under the green dash curves were found to lie well within the green continuous curve. Hence, according to GEF, the fragments from QF process significantly overlap with the CN contributions. As described earlier, the mass distributions in case of ^{16}O+^{175}Lu system are well reproduced by GEF. This code has been observed to be successful in explaining nearly all low energy fission data in the sub-Pb region [2, 33]. Also, this code do not consider any non-compound fission process while calculating the fragment distributions. Thus, it can be considered that fragment mass distributions observed in case of ^{16}O+^{175}Lu system are from CN fission only. Assuming that the process of QF is not producing fragments around mass $A_{CN}/2$, the amount of QF contribution was estimated using experimental data also. The difference between fragment mass distributions for both the systems at similar E^*_{CN}, shown in Fig. 4.6, also predicted 20% QF contribution.

The distributions for ^{16}O+^{175}Lu reaction at E^*_{CN}=49.7 MeV and ^{37}Cl+^{154}Sm reaction at E^*_{CN}=51.4 MeV were also calculated using 4D Langevin dynamical model of CN evolution ([98, 99],and references therein). The calculated distributions do not show any significant difference between the two systems with similar E^*_{CN}. This observation gave another evidence of presence of QF in case of ^{37}Cl+^{154}Sm reaction.

To get a deeper insight of QF process observed in case of ^{37}Cl+^{154}Sm reaction, the distribution of the QF products were calculated in the framework of the dinuclear system (DNS) model [66, 100]. The DNS model predictions of 22% qasifission for ^{37}Cl+^{154}Sm reaction and negligibly small QF contribution for ^{16}O+^{175}Lu reaction are in good agreement with the experimental observations. The calculated distribution of the QF products for the ^{37}Cl+^{154}Sm (E^*_{CN}=51.4MeV) reaction is also in good agreement with the experimentally obtained distribution as shown

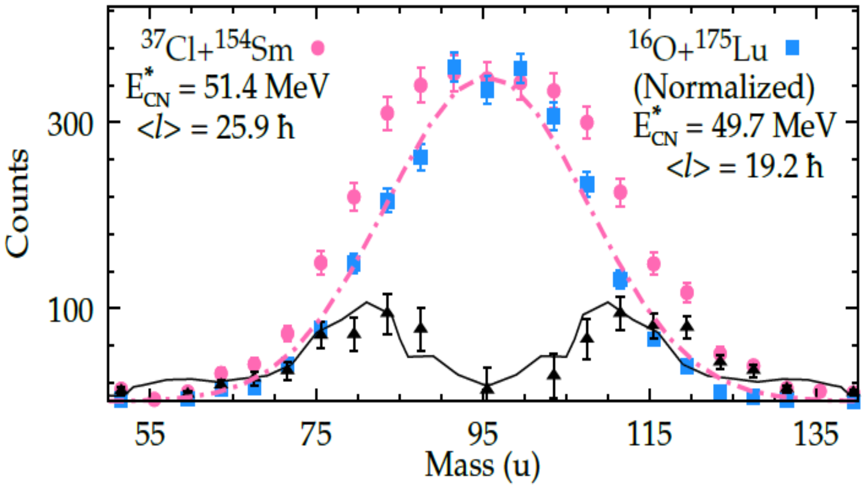

Figure 4.6: The difference (filled triangles) between the measured mass distributions for the two reactions (filled circles and squares) at similar E^*_{CN} and $\langle \ell \rangle$ is compared with the result of the dinuclear system (DNS) model calculation (continuous line) for QF in ^{37}Cl+^{154}Sm system. The dot-dashed line is the expected distribution from the statistical relation (Eq. 4.1) for the ^{37}Cl+^{154}Sm system.

in Fig. 4.6. Shell effects in the emerging light fragments (Z=32-34 and N=46-48) of the dinuclear system were found to persist at these energies and influence the outcome.

4.4 Mass distribution width (σ_{MR})

Since the deviations from single Gaussians were observed to be small, the widths of the fitted Gaussian were also examined to study the role of the entrance channel dynamics. Statistically, it is expected for an equilibrated CN that the variance of the fission fragment mass distribution σ^2_{MR} varies with temperature T and the mean square angular momentum $\langle \ell^2 \rangle$ as [101]:

$$\sigma^2_{\mathrm{MR}} = \lambda T + \kappa \langle \ell^2 \rangle \tag{4.1}$$

Unlike heavy nuclei, in light compound systems ($A \sim 200$), the descent time from saddle point to scission point is short and the temperatures are very similar [102]. So, for above calculation, the temperature of the fissioning nuclei was calculated as,

$$T = \sqrt{\frac{\mathrm{E}^*_{\mathrm{B}_f}}{a}} \tag{4.2}$$

Using effective excitation energy above barrier,

$$\mathrm{E}^*_{\mathrm{B}_f} = \mathrm{E}^*_{\mathrm{CN}} - B_f(\langle \ell \rangle) - E_{pre} - E_{rot} \tag{4.3}$$

here, $B_f(\langle \ell \rangle)$, E_{pre} and E_{rot} are the fission barrier at $\langle \ell \rangle$, average energy removed by the pre-saddle neutrons and rotational energy of the CN respectively. The angular momentum dependent barrier heights were calculated as,

$$B_f(\langle \ell \rangle) = B_{f,0} - \Delta B_{f,\langle \ell \rangle} \tag{4.4}$$

where, $B_{f,0}$ is the predicted barrier height [103] and $\Delta B_{f,\langle \ell \rangle}$ is the reduction of the barrier height due to nuclear rotation. The value of the level density parameter, a in equation 4.2 was taken as $\mathrm{A_{CN}}/9$. The rotating finite range model (RFRM) [104] was used to calculate E_{rot} and $\Delta B_{f,\langle \ell \rangle}$. The E_{pre} values were estimated using the statistical model code PACE [105, 106].

Assuming that the statistical description is valid for the more asymmetric system, the experimental widths for the ^{16}O+^{175}Lu system were fitted (black dashed line in Fig. 4.5) to obtain the coefficients, λ and κ of the equation 4.1. The mean square values of angular momentum ($\langle \ell^2 \rangle$) were obtained from CCFULL calculation as discussed in section. 4.3. The T and $\langle \ell^2 \rangle$ range of the present measurement were not sufficient to constrain both the coefficients simultaneously. The value of κ was kept same ($(1.23 \pm 0.24) \times 10^{-6}$) as used for the near by system ^{16}O+^{186}W [102]. The best fit could be obtained with $\lambda = (2.77 \pm 0.08) \times 10^{-3}$. The value of λ and κ are in good agreement with the systematics [107]. As can be seen in Fig. 4.5, the calculated values of σ_{MR} (pink solid line) using the same coefficients for ^{37}Cl+^{154}Sm system were found to be much smaller than the experimentally obtained widths. The observed mass widths could not be reproduced by reasonable variation of the parameters and estimated $\langle \ell^2 \rangle$. This observation further confirmed the significant presence of QF in case of ^{37}Cl+^{154}Sm reactions.

4.4.1 Systematic Comparision

A systematic comparison of mass distribution widths (σ_{MR}) for nearly all the heavy ion fusion fission data in sub-Pb region was also performed. To analyse different reaction channels in an energy independent way, the fitted mass distribution widths for all systems were plotted as a function of centre of mass energy with respect to the Coulomb barrier ($\mathrm{E_{cm}/V_B}$), as shown in Fig. 4.7.

In case of present measurement, while the experimental mass widths for

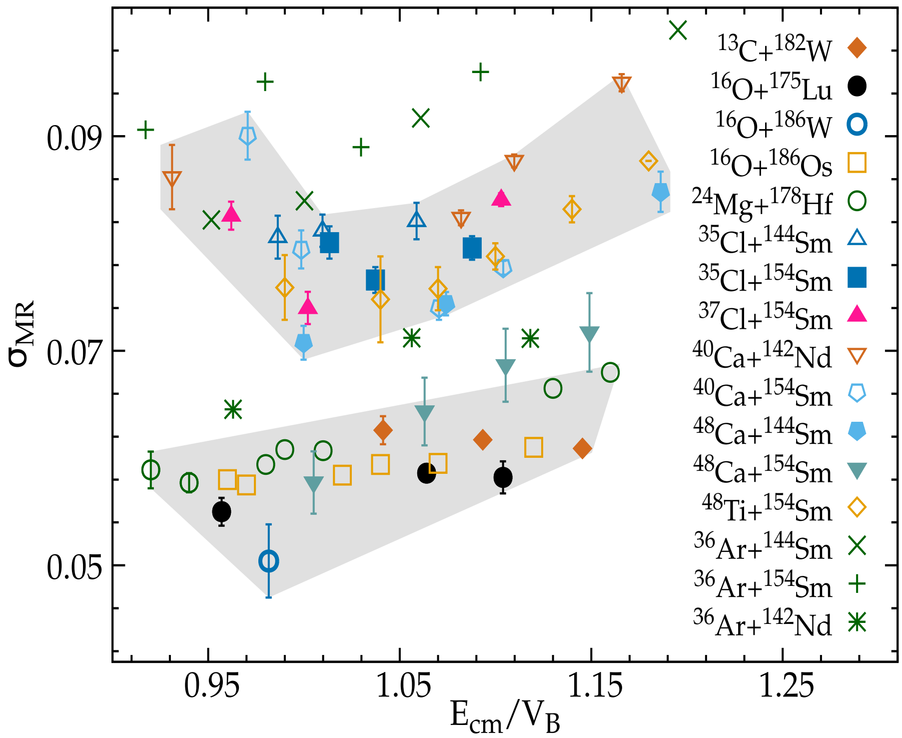

Figure 4.7: Experimental mass widths relative to CN mass (σ_{MR}) for nuclei in heavy-ion induced reactions [55, 56, 57, 58, 95, 102]. The region of C, O, Mg induced reactions and Cl, Ca (except ^{48}Ca+^{154}Sm, see text) induced reactions are shaded separately to highlight the difference among them.

^{16}O+^{175}Lu system were found to increase monotonically with increasing energy, the mass width shows a increase with decreasing energy below the Coulomb barrier for ^{37}Cl+^{154}Sm, characteristic to QF involving deformed targets [93].

Overall, the fitted mass widths for most of the heavier projectile (^{35,37}Cl, ^{40,48}Ca and ^{48}Ti) induced and lighter projectile (^{13}C, ^{16}O and ^{24}Mg) induced reactions demonstrated distinctly different behavior as shown by the shaded regions. In general, Cl, Ca and Ti induced reactions involving both spherical as well as deformed targets exhibit significantly larger widths as compared to C-Mg induced reactions. Further, all the systems involving ^{154}Sm (deformed) target with heavy beams appeared to show an increase in the width with decreasing energy below the Coulomb barrier. In case of neutron rich ^{48}Ca+^{154}Sm system [102], the QF exhibits signature of fast time scale, i.e., observation of mass-angle correlation in asymmetric splits, which were clearly separated from the fusion-fission (symmetric) products. The widths of the symmetric distributions were found to be comparable to those of lighter ion induced reactions, thus having no significant contribution from QF in the symmetric region. While no such distinctly separate QF contribution were observed for ^{48}Ca+^{144}Sm and ^{40}Ca+^{154}Sm [102], widths of the symmetric distributions for these systems were found to be larger as compared to those for ^{48}Ca+^{154}Sm system and other lighter ion induced reactions, indicating the presence of slow QF in these neutron deficient combinations. This also suggested a strong role of N/Z on the nature of QF. In case of ^{36}Ar+^{142}Nd, ^{144,154}Sm [55, 58], the measured mass distributions displayed large deviation from a single Gaussian distribution hence we plotted the square root of the variance, $\sigma_m^2 = \frac{1}{\sum_i n_i} \sum_i n_i \times (\mathrm{M}_i - \overline{\mathrm{M}})^2$, for these systems. Where, n_i is the counts for the mass M_i and $\overline{\mathrm{M}}$ is the mean mass. While the data for ^{36}Ar+^{142}Nd lies below the shaded region for heavier projectiles and are in agreement with GEF prediction [33], the data for ^{36}Ar+^{144,154}Sm were found to be much higher. The above comparisons indicated that most of the systems involving heavier projectile are having contribution from the quasi-fission process.

4.5 Chapter summary

The fragment mass distributions in fission of ^{191}Au, formed via two different entrance channels ^{16}O+^{175}Lu (α=0.832, Z_pZ_t=568) and ^{37}Cl+^{154}Sm (α=0.612, Z_pZ_t=1054) having mass asymmetries α on either side of Businaro-Gallone point (α_{BG}) have been measured down to excitation energy of ≈20 MeV above the fission barrier. The experimental mass distributions for ^{37}Cl+^{154}Sm system were found to be much (∼30%) broader than those for ^{16}O+^{175}Lu system at similar E^*_{CN} and $\langle \ell \rangle$. Such a difference is not expected in the decay of compound nucleus, according to the statistical relation (Eq.(4.1)), semi-empirical code GEF as well as the 4D Langevin dynamical model. The mass width for ^{37}Cl+^{154}Sm system were found to increase with decreasing energy below the Coulomb barrier. These results provide conclusive evidence of substantial presence of QF for the more symmetric entrance channel. The Dinuclear system (DNS) model calculation, which reproduces the observed QF probability and its distribution, revealed the persistence of shell effects in the emerging light fragments of the dinuclear system.

A systematic analysis of the available experimental data demonstrated significant presence of QF whenever heavier projectiles (Z≥17) were used with spherical or deformed targets to investigate fission of neutron deficient sub-Pb nuclei. This observation gave a clear indication that not only the shell effects, but the dynamics in the entrance channel also have a significant role in influencing the fission of nuclei in the newly identified island of mass asymmetry and both these aspects needs to be considered to interpret heavy-ion data unambiguously.

5

Evolution of multimodal fission

5.1 Introduction

The importance of shell effects in the nascent fragments, emerging close to the outer saddle, is well-established for low-energy fission of actinides. However, the origin of asymmetric fission in the neutron-deficient lead region is still not clear [1, 2]. State-of-the-art models, explaining the experimental data in this "new" region of asymmetric fission yielded contradictive interpretation regarding the role of shell effects, at either saddle or scission and nuclear dynamics [25, 26, 27, 28, 108]. Recently, elaborate but *different* model calculations demonstrated that the common origin of favoured asymmetric fragmentation in the two regions are coupling between deformed shells of the emerging fragments [17, 29]. In the microscopic calculations by T. Ichikawa and P. Moller [17], it is reported that the coupling between levels of type [40ΛΩ] and [51ΛΩ] in actinide region and [30ΛΩ] and [41ΛΩ] in pre actinide region are responsible for lowering the fission saddle for mass-asymmetric shapes after which these asymmetric shapes decided at *saddle*, remains preserved until scission. On the other hand, the microscopic calculations by G. Scamps and C. Simenel [16, 29] displayed that since correlation between certain deformed shells of the fragments induces pear shape, shortly before scission when the fragments are connected by a neck, each fragment have a pear shape, this enhances the production of nuclei which can exhibit octupole shapes for no or little cost in energy instead of spherical closed shell nuclei which are hard to deform. Accurate modeling of fission is still a challenge for nuclear theory [2]. While a qualitative (static) description can be achieved by quantum-mechanical models [112], a quantitative (dynamical) description is missing in most cases.

5.1.1 Multimodal fission

The data set collected so far also brought to light a strong influence of N/Z of the fissioning system on the fragment asymmetry properties [10]. For instance, along the Thorium isotopic chain, a pre dominantly asymmetric fission fragment mass distribution for neutron rich ^{232}Th changes towards symmetric fission for neutron deficient ^{220}Th, with a triple-humped distribution in case of ^{224,226,228}Th. Such distributions arises in the presence of multiple modes of fission (multiple valleys and ridges, as described in section 1.3). When the total potential energy surface has valleys in the space of elongation and mass asymmetry, the nuclei do not see one fission barrier (single or double humped) but a system of them. This provides several different paths (modes) to the nucleus for fission, resulting in distribution with peaks for mass symmetric as well as asymmetric split. More experimental information is clearly necessary before a consistent understanding of the physical mechanism at play can be extracted.

5.1.2 Why ^{198}Po?

Fission fragment mass distribution data in the actinide region displays a predominantly asymmetric fission for neutron *rich* nuclei. However, in the sub-Pb region, experimental data displays an opposite trend with highly asymmetric mass distribution for neutron *deficient* nuclei. With Z = 84, the element polonium is ideally situated midway between mercury (Z=80) and actinides (Z$\geq$88 or so). It is thus *a priori* particularly suited to search for a connection between preactinide and actinide asymmetric fission. Furthermore, isotope A = 198 is located at the centre of the area studied with the β-delayed and electromagnetic induced approaches, over which the fragment properties were observed to change fast [31, 109]. Information on isotope A = 198 permits us to proceed further along the polonium chain and to map out the balance between asymmetric and symmetric splitting as a function of the fissioning system N and Z.

As discussed in section 4.1, the ideal way to attain low excitation energy required for studying fragment shell effects on fission dynamics are β delayed fission and electromagnetic-induced fission, but the number of fissioning systems accessible and associated experimental requirements with these techniques are extremely challenging. Hence, in the present work, we investigated fission of ^{198}Po using heavy ion induced fusion-fission reaction in ^{28}Si+^{170}Yb system at sub barrier energies [33].

5.2 Data Analysis & Results

Fusion-fission events were separated from other reaction channels by applying a software gate on the correlation between ΔT and (ΔE_1+ΔE_2) as shown in Fig 5.1. To investigate the possible influence of target contaminants (namely, 10.3% of ^{171}Yb, 2.67% of ^{172}Yb, 1.36% of^{173}Yb, and 1.96% of ^{174}Yb), statistical-model code PACE (with input ℓ distribution calculated from CCFULL) was used. All indicated that more than 90% of the collected fission events are due to the ^{198}Po compound nucleus.

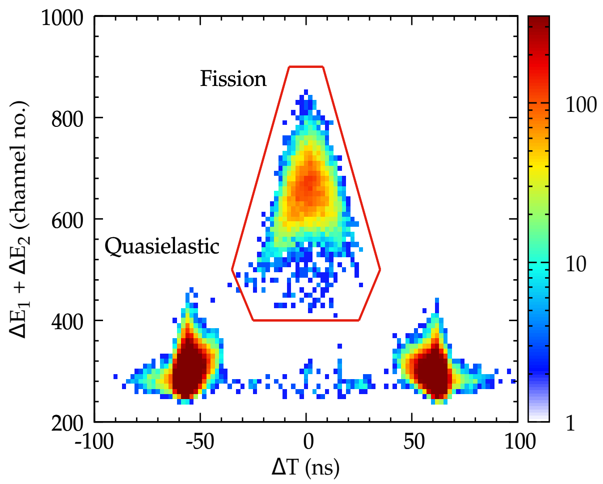

Figure 5.1: Time of flight difference ($T_1 - T_2$) vs energy loss ($\Delta E_1 + \Delta E_2$) spectra used to separate fission from quasi-elastic (QE) events for ^{28}Si+^{170}Yb at $E_{lab.}$=129.2 MeV. The thick contour delineates the region attributed to fission.

The correlations between the folding and azimuthal angles as well as between parallel and perpendicular components of the velocity onto the beam axis for the

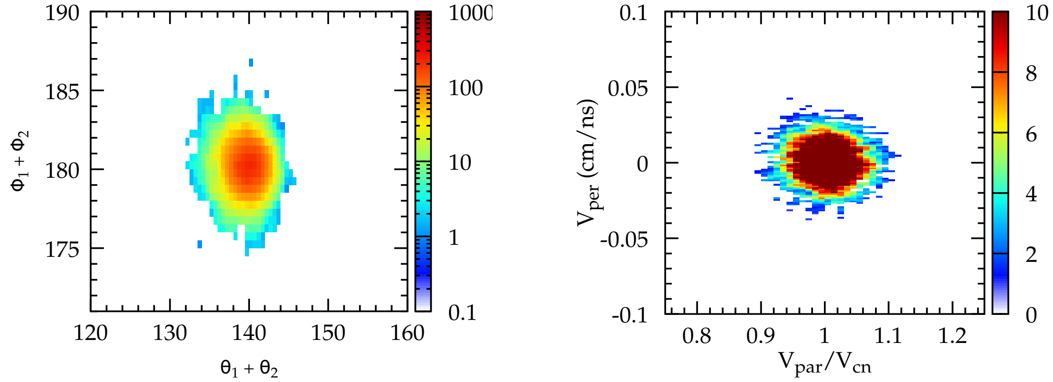

Figure 5.2: A typical correlation plot of the folding angle ($\theta_1+\theta_2$) vs. azimuthal angle ($\phi_1+\phi_2$) and V_{par}/V_{cn} vs. V_{per} for the selected fission fragments for ^{28}Si+^{170}Yb at $E_{\mathrm{lab.}}$=129.2 MeV.

selected fission events, shown in Fig. 5.2, confirmed the absence of transfer induced (incomplete momentum transfer) events at all measured energies. Fragment mass distributions were deduced using the TOF difference method as discussed in section. 3.6.2. The total kinetic energies (TKE) were obtained using the deduced masses and linear momenta. Experimental resolution, obtained from the elastic peak, was 4.9 amu (full width at half maximum) for mass and 8% for TKE.

Measured correlations between the fragment mass and the emission angle θ_{cm} are shown in Fig. 5.3. As can be seen from this plot, no mass-angle correlations were observed at all measured energies, suggesting the absence of fast quasifission. According to our systematic study of mass distribution widths (section. 4.4.1) also, no quasifission is expected for measured system as Z_p is less than 17.

In order to remove the bias due to geometrical acceptance of the detection setup, the fission fragment mass and total kinetic energy distributions were obtained by projecting the mass angle correlations with angular cut of $\theta_{1,cm}$ from

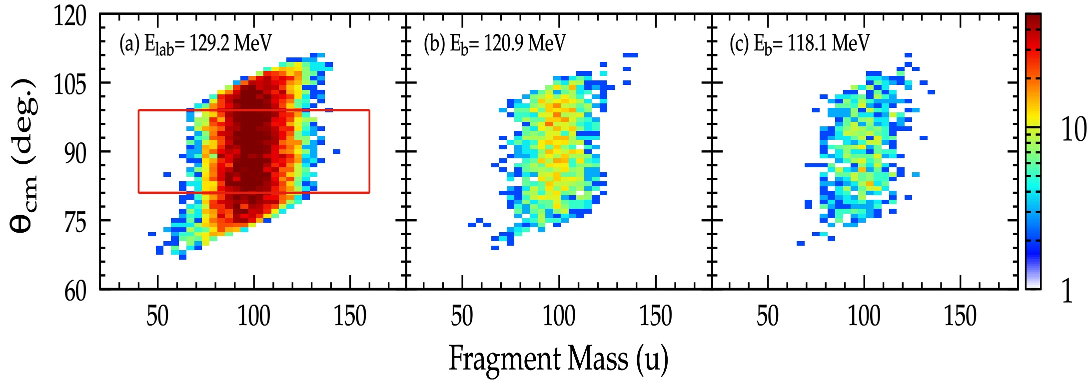

Figure 5.3: Experimentally obtained mass-angle correlation plot for selected fission fragments in reaction ^{28}Si+^{170}Yb at three beam energies of 129.2, 120.9 and 118.1 MeV respectively. The typical angular cut used to obtain the mass and total kinetic energy distributions is shown as rectangular box for highest measured energy.

81° to 99° at all measured energies (shown as rectangular box in Fig. 5.3). The deduced fission fragment mass distributions for ^{28}Si+^{170}Yb reaction corresponding to three different CN excitation energies of 44.1, 37.0 and 34.5 MeV is shown in Fig. 5.4. The corresponding effective excitation energies above fission barrier $E^{*}_{B_f}$ (discussed in section. 4.4, Eqn.(4.3)) is also shown. At all three measured energies the deduced fission fragment mass distributions were well approximated with a Gaussian function (solid black lines in the figure), suggesting the absence of shell effects in present measurement. However, recent theoretical calculations have predicted a significant presence of shell effect in the pre actinide region for measured excitation energy range [111]. A contribution from asymmetric fission was therefore expected. The evidence of the presence of an asymmetric contribution in a fragment-mass distribution can be hard to detect with increasing excitation energy if the distribution is triple humped at low E^{*}_{CN}. As the shallow dips between the asymmetric and symmetric components gets more and more filled up with raising

E^*_{CN}, unambiguous interpretation of the data becomes difficult. Anticipated fair balance between symmetric and asymmetric partitions for ^{198}Po at low E^*_{CN}, from the β-delayed measurements of nearby nuclei, is expected to make its signal at higher E^*_{CN} difficult to evidence.

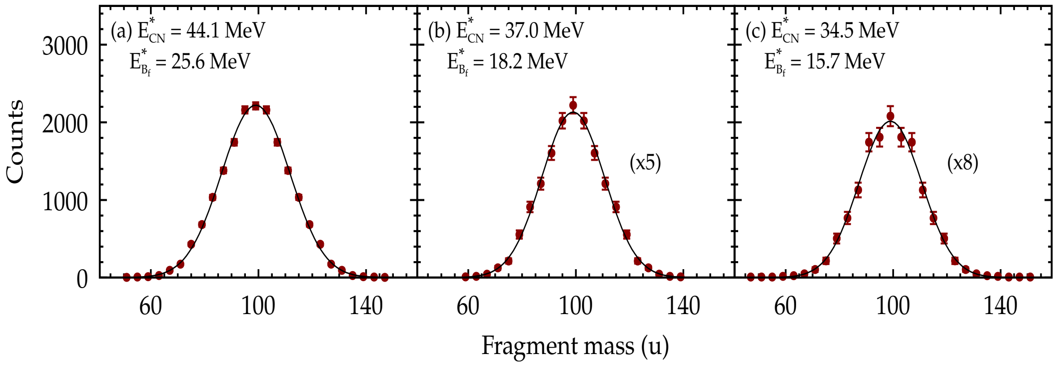

Figure 5.4: Fragment mass distributions from fission of ^{198}Po at different compound nucleus excitation (E^*_{CN}) obtained in the ^{28}Si+^{170}Yb reaction. The effective excitation energies above fission barrier ($E^*_{B_f}$) is also indicated. At lower two energies (b-c), the acquired statistics was low hence the yields are scaled to show different energies in a single plot. The scaling factors used are shown in parentheses.

As a common practice in low-energy fission to investigate the contribution of different so-called fission modes [1], a multifit analysis of the measured mass distributions was performed. Several such studies in the sub-Pb region [17, 31, 55, 57, 58] have led to various interpretations, with the presence of exclusively symmetric fission, exclusively asymmetric fission, or the coexistence of symmetric and asymmetric fission. Since, no obvious structure was visible in the measured fragment mass distributions, we used the available nearby ^{196}Po [31] isotope data to guide a physics based adjustment. According to shell effects observed in very low energy ($E^*_{B_f}$≈B_f) fission of ^{196}Po [31], the light (heavy) fragment peak of the asymmetric mode, if any remain, is expected to be located around $A_{l(h)}$=84-88 (110-114). A good three Gaussian fit description of the measurement was indeed achieved with a constraint in the range A = 86-112 as shown in Fig 5.5, upper panel. However, the single Gaussian distribution shown in Fig. 5.4 yielded an equally good description (Fig. 5.5, lower panel).

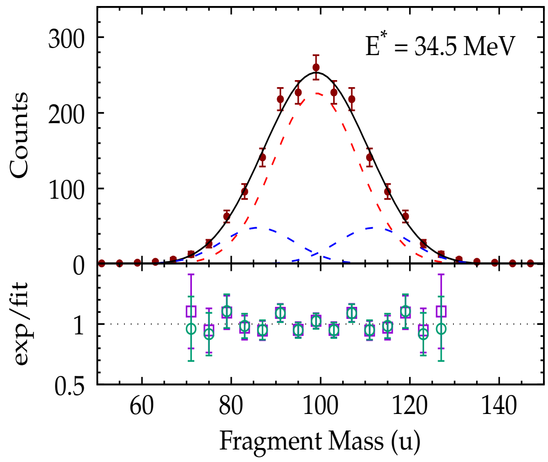

Figure 5.5: Outcome of the multifit analysis. Upper panel: Adjustment of the experimental mass distribution for E^*_{CN}=34.5 MeV with a sum of three Gaussians (dashed lines show the contribution of symmetric fission and asymmetric fission separately, and the solid line is their sum). Bottom panel: Ratio between the experimental and the adjusted distributions, assuming a single Gaussian (violet squares) or a three Gaussian (green circles) fit.

We further looked for evidence of asymmetric fission in the measured total kinetic energy (TKE) distributions, which is established to be a relevant observable to discriminate between various fission modes in the actinides. As discussed in section. 1.3, shell effects in emerging fission fragments creates various valleys in the potential energy surface which are responsible for different modes of fission. Since separate modes of fission corresponds to different paths followed by fissioning nuclei along mass asymmetry degree of freedom, the corresponding different shapes of the fissioning system at scission associated with these modes/paths, can give rise to multiple peaks in TKE distribution (see section. 2.3.2). That is, an elongated shape of the fissioning system at scission with large deformation in both the emerging fragments will give low TKE, while a compact shape with nearly spherical fragment will result in high TKE. Recently in sub-Pb region, this phenomenon has been utilized to separate asymmetric and symmetric fission modes for ^{178}Pt [58] and ^{194,196}Po [31] fissioning systems. In fission study of ^{178}Pt [58], it was demonstrated that the asymmetric mode is associated with larger TKE values than the symmetric mode. However in case of ^{194,196}Po [31], a lower (than average value) TKE gated mass spectra was observed to give asymmetric component of the total fission fragment mass distribution.

The deduced total kinetic energy distributions for ^{198}Po in the present study is shown in Fig. 5.6. In our measurement, we could not draw any conclusive answer by studying either mass-gated TKE distributions or TKE-gated mass distributions.

The measured correlations between the fragment mass and the total kinetic energy in the present work is also shown in Fig. 5.7. The evolution of the mean TKE with fragment mass, displayed as open white circles on top of the (A, TKE) correlations followed reasonably well the parabolic trend expected in the macroscopic liquid-drop-based systematics [9] at highest E^*_{CN}. However, some departure from this trend was observed with decreasing E^*_{CN}. The experimental TKE(A) tendency seems to get flatten as E^*_{CN} decreased.

In the absence of any clear indication from mass and TKE distributions, we further analysed the width (σ_A) of the fragment-mass distributions to probe the

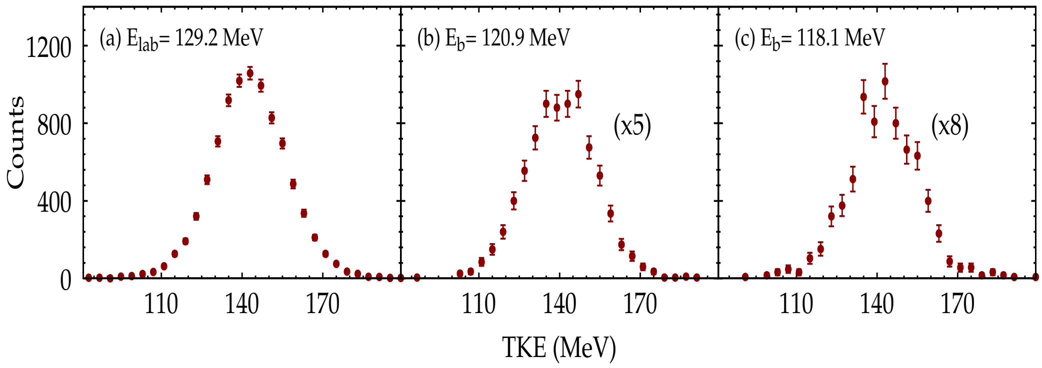

Figure 5.6: Deduced total kinetic energy distributions of fission fragments from ^{198}Po in reaction ^{28}Si+^{170}Yb at three beam energies of 129.2, 120.9 and 118.1 MeV respectively.

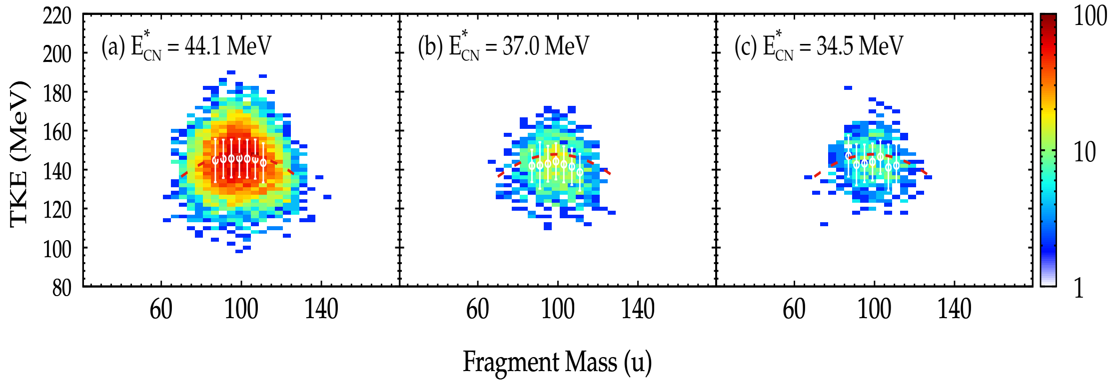

Figure 5.7: Measured correlations between the fragment mass and the total kinetic energy at three compound nucleus excitation energies (E^*_{CN}) of 44.1, 37.0 and 34.5 MeV respectively. The mean TKE as a function of fragment mass is shown as open white circles. The dashed curve represents the TKE from macroscopic parametrization [9].

presence of asymmetric fission if any. As discussed in section. 4.4, in the sole presence of liquid-drop-driven (symmetric) fission, the mass distribution width can be described by the statistical relation $\sigma_A^2 = \lambda T + \kappa\langle\ell^2\rangle$ [101]. That is, as the temperature (T) and mean square angular momentum $\langle\ell^2\rangle$ of a fissioning system decreases, the width of the final fission fragment mass distributions also decreases. For a complete fusion fission reaction, any deviation from this trend, namely larger σ_A value at lower energy signals the contribution from additional asymmetric partitioning. The $\langle \ell \rangle$ and $\langle \ell^2 \rangle$ values required for this statistical calculation were obtained using the coupled channels code CCFULL [42] (described in section. 2.1.1). The fusion excitation function for ^{28}Si+^{170}Yb was not available. So, the fusion data for similar system, ^{28}Si+^{170}Er [110] was scaled according to Coulomb parameter $Z_p Z_t/(A_p^{1/3} + A_t^{1/3})$ for CCFULL calculations. Since both, the projectile (β_2=-0.363) as well as the target (β_2=0.287) are highly deformed in ^{28}Si+^{170}Yb reaction, the coupling between the projectile and the target rotational states were used in CCFULL calculations to reproduce the scaled data. All other required parameters, $B_f(\langle \ell \rangle)$, E_{pre} and E_{rot} etc. were calculated using same approach as discribed in section. 4.4 and the estimated values for present measurement of ^{28}Si+^{170}Yb reaction are given in Table 5.1.

Table 5.1: Effective beam energies at the centre of the target in the laboratory frame (E$_{lab.}$), centre of mass energy (E$_{cm}$), excitation energy of compound nucleus (E$^*_{\rm CN}$), estimated average angular momentum ($\langle \ell \rangle$), effective excitation energy above barrier (E$^*_{\rm B_f}$), mean square angular momentum ($\langle \ell^2 \rangle$), temperature at saddle point (T) and the width of the experimental mass distributions relative to the CN mass ($\sigma^{expt.}_{\rm M_R}$) of present measurement.

E$_{lab.}$ (MeV)	E$_{cm}$	E$^*_{CN}$	$\langle \ell \rangle (\hbar)$	E$^*_{\rm B_f}$	$\langle \ell^2 \rangle$	T (MeV)	$\sigma^{expt.}_{M_R}$
^{28}Si+^{170}Yb(V$_{\rm B}$=114.8 MeV)							
118.1	101.4	34.5	9.5	15.7	116.3	0.832	0.0588±0.74×10^{-3}
120.9	103.8	37.0	10.7	18.2	145.5	0.897	0.0588±0.64×10^{-3}
129.2	110.9	44.1	20.5	25.6	500.0	1.064	0.0640±0.52×10^{-3}

Assuming that the shell effects are vanished at highest measured CN excitation energy of 44.1 MeV, we calculated the temperature dependence (λ) for present system by fixing κ at $((1.23{\pm}0.24){\times}10^{-6})$, as used for the near by ^{34}S+^{168}Er system forming ^{202}Po [95]. The corresponding calculated value of $\lambda = (2.77 \pm 0.08) \times 10^{-3}$ is in good agreement with measurement of Ref. [95]. The σ_A data for the present measurement along with statistically expected value are displayed in Fig. 5.8 as a function of ^{198}Po excitation energy. The deviation of the experimental mass width from the expectation of the statistical relation at the lowest energy also suggested the increasing presence of asymmetric fission towards lower excitation energy.

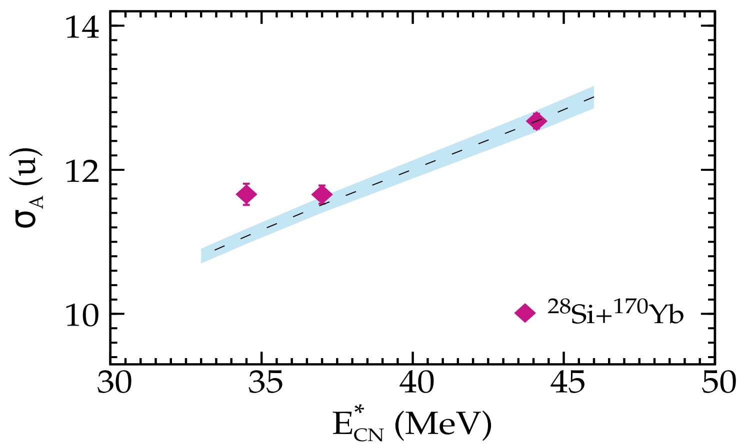

Figure 5.8: Experimental (symbols) fragment-mass width (σ_A) as a function of ^{198}Po excitation energy. The dashed line represents the parametrized expectation for symmetric fission. The shaded band indicates the uncertainty range of the parameters.

5.3 Fission along the polonium chain

According to recent theory proposed by Scamps and Simenel (briefly discussed in section. 5.1), the low-energy fission of ^{198}Po is expected to be asymmetric. Driven by a stabilized elongated octupole proton configuration in the light fragment, the expected mean asymmetric mass split is $A_l(h)$=87(111) according to this calculation. These values are consistent with the aforementioned possible three-Gaussian adjustment. Unfortunately, no theoretical mass distribution could be obtained yet within this model, and namely not at finite excitation energy. Only mean positions of the main fission channels were provided to us by the authors in a private communication.

To get further insight into the ^{198}Po measurement and how it falls within so-far available information in the region, we used the semiempirical GEF model [61] (described in section. 2.3.3). Since GEF is well parametrised to reproduce fission data in actinide region and only four data points were used to parametrise it for data in sub-Pb region [2], we investigate the accuracy of its achievement in our region of interest before interpreting our measurement. A comparison of calculation with experimental data from β-delayed [panels (a)-(d)] and heavy-ion fusion-induced [panels (e)-(h)] fission for representative cases [18, 31, 32, 58, 113] are shown in Fig. 5.9. In addition to the integral distributions (red solid lines), the decomposition into symmetric and asymmetric modes as predicted by GEF (blue dash-dotted lines) is also shown in the figure. For β-delayed fission, the calculation was performed assuming that the initial excitation energy is equal to the fission barrier.

An overview of Fig. 5.9 showed that GEF is able to give a reasonable description of the experimental results, as a function of the fissioning system A and Z, on one side (low energy fission data from β delayed fission), and as a function of E^*, on the other side (heavy ion induced fission data). We also note that the decomposition into various modes by the model (which was a prediction at the

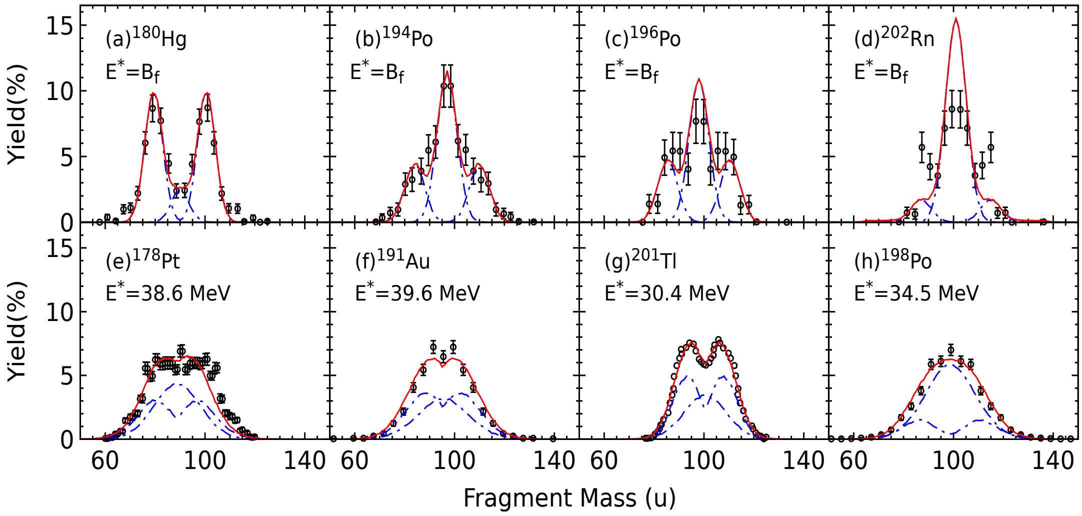

Figure 5.9: Comparison between experimental fragment mass distributions (symbols) with GEF calculations (red solid lines) for various fissioning systems. The symmetric and asymmetric components of the calculated distributions are shown as well (blue dash-dotted lines). The upper and lower rows refer to β-delayed and heavy-ion fusion-induced fission, respectively.

time of its development) is in good agreement with the experimental interpretation of Ref. [58] for ^{178}Pt. We therefore estimated that a GEF -based approach is valid for our purpose.

As can be seen from Fig. 5.9, GEF provided a good description of the fragment-mass distribution for ^{198}Po measured at E*= 34.5 MeV in present study. According to the calculation, the obtained integral mass distribution is the superposition of symmetric and asymmetric fission, with 75% and 25% weight, respectively. We found that these GEF prediction are consistent with three-Gaussian deconvolution shown in Fig. 5.5. The very origin of the observed substantial asymmetric contribution at such E* (still 25% at E*=34.5 MeV) was further investigated. The possibility that it does not all originate from ^{198}Po fission, but has sizable contributions from later-fission chances, i.e. fission after neutron evaporation by ^{198}Po, was tested. According to GEF, the mean prescission neutron multiplicity for ^{198}Po at E*=34.5 MeV amounts to 0.42. The calculations then suggested that fission of ^{198}Po at E*=34.5 MeV is made of 64% first chance and 36% later chance (with second chance dominating). The asymmetric component due to both these contributions is displayed in Fig. 5.10. Since lower excitation energy results in larger peak to valley ratio, the calculated mass distribution is more asymmetric in second chance fission. However, first-chance fission was observed to be responsible for about half of the asymmetric component in Fig. 5.9(h) (reported again in Fig. 5.10 as a black solid line).

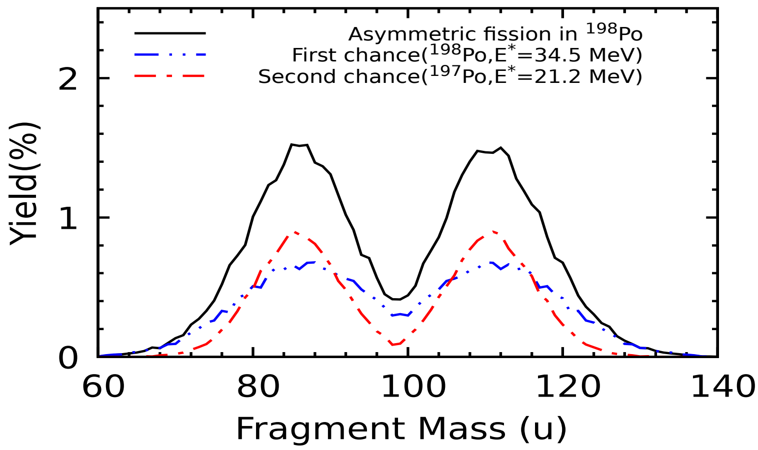

Figure 5.10: Calculated asymmetric contribution from first (blue dash-double-dotted line) and second (red dash-dotted line) chance fission, and their sum (black solid line) weighted by the corresponding fission probability.

According to these calculations and their description of the experimental findings, we therefore concluded that fission retains a non-negligible degree of asymmetry for ^{198}Po at E*=34.5 MeV, which is slightly enhanced by later-chance fission.

At E*=37.0 and 44.1 MeV, an asymmetric first chance fission component still persists, but its contribution (as well as its peak-to-valley ratio) decreases, to the advantage of an increasing contribution from second and third chance fission.

Based on above observed consistency of GEF in reproducing the measured data in sub-Pb region, we implicitly trusted its calculated excitation energy dependence to infer the fission properties of ^{198}Po close to the barrier. The outcome is shown in Fig. 5.11. It suggests $A_{l(h)}$ to be located at 87 (111), which is observed to be consistent with the microscopic model prediction. The associated weight amounts to 46%, which is comparable to that observed for ^{196}Po.

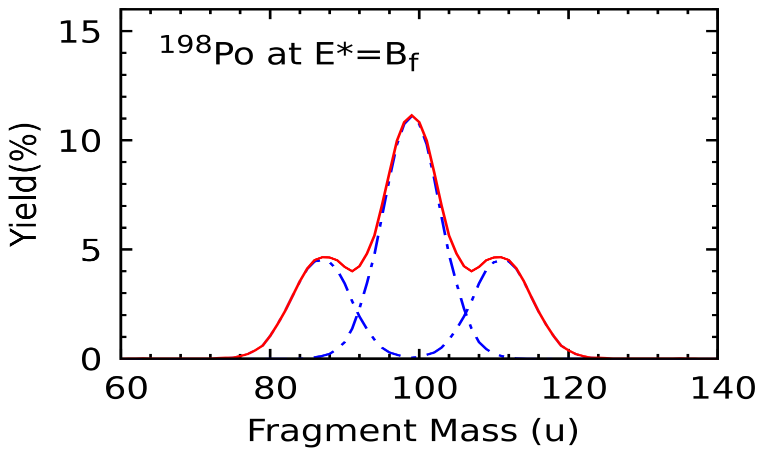

Figure 5.11: Fragment A distribution as predicted by GEF for ^{198}Po close to the barrier along with the symmetric and asymmetric components.

5.4 Chapter summary

The fragment mass and total kinetic energy properties for fission of ^{198}Po produced in the ^{28}Si+^{170}Yb reaction have been measured for initial excitation energy of 34.5, 37.0 and 44.1 MeV. Being situated midway between two regions of dominantly asymmetric fission at low excitation energy, isotope ^{198}Po have a pivotal position on the nuclear chart. No clear structure, which would be an irrefutable signature of asymmetric fission, was exhibited by the mass distribution. The presence of asymmetric partitions was suggested by a weak flattening of TKE with mass, and the non-monotonic evolution of the fragment-mass distribution width with excitation energy.

The experimental indication of asymmetric partitions, up to a few tens of MeV above the fission barrier is found in agreement with the analysis of the experimental mass distribution by calculations within the semi-empirical GEF model. According to the good description achieved by the code for representative measurements in the region, the calculation was used to trace back the fission properties of ^{198}Po close to threshold. The so obtained mass distribution is triple humped and contributes in establishing the gradual evolution along the polonium chain. The extracted asymmetric fragment properties are found consistent with most recent microscopic calculations.

6

Systematic study of asymmetric fission

6.1 Introduction

In the earlier studies of fission dynamics, which consists of low energy fission data in actinide region [8, 88, 89], the dominance of asymmetric fission over symmetric fission was explained by combining macroscopic (liquid drop model predicted smoothly evolving potential of CN) and microscopic (shells in the emerging fission fragments) effects [90]. As discussed in section 1.3, these studies suggested that the stabilization in nascent fragment *neutron shells* are main cause of asymmetric fission fragment mass split and explained the robustly sitting structure around $A_{\mathrm{H}}\sim140$ as a combination of S1 mode with N=82 (spherical shell) derived $A_{\mathrm{H}}\sim134$ stability and S2 mode with N=88 (deformation dependent shell correction at scission) derived $A_{\mathrm{H}}\sim144$ stability [60].

Later, an extensive set of data from GSI [10] demonstrated that under the broad peak of constant A, it is actually the constant Z of the heavier fragment which is stable at Z=52 and Z=55 for the S1 and S2 mode respectively with no preferential population of known neutron shells [12]. It was observed that the events around Z=52 have a high TKE, a low neutron multiplicity for the heavy partner, and its yield increases with N_{CN}/Z_{CN} approaching that ^{132}Sn. This observation led to the conclusion that this S1 mode is primarily driven by the Z = 50 shell aided by N = 82 which was further supported by the abrupt transition from asymmetric to symmetric fission while approaching ^{264}Fm [114, 115]. An interpretation for the Z=55 mode was proposed recently only, in terms of the favoured formation of a stabilized octupole configuration [16].

Although there was an observation of asymmetric fission in light-ion induced fission measurement of ^{201}Tl by Itkis *et al* [22, 101], formerly, following the trend observed in actinide region, it was anticipated that a nuclei in pre-actinide region will undergo symmetric fission. From this previous understanding of well studied data in actinide region, also known as "old" island of asymmetric fission it was expected that neutron deficient ^{180}Hg will undergo symmetric fission producing two semi-magic ^{90}Zr. However, an observation of almost exclusively asymmetric fission of ^{180}Hg opened a whole "new" island of asymmetric fission just a decade ago. Later, measurements of additional systems [31, 55, 57, 58, 116] ascertained this occurrence of asymmetric fission over an enlarged domain around lead.

Since quantum effects are a property of the nucleus, if the nuclear structure of the nascent fragments indeed plays a key role, analogous stabilizations must be at play in both "new" and "old" island of asymmetric fission. Still, a consistent understanding of the fragment properties running from the "old" (actinide) to the "new" (sub-lead) region of asymmetric fission is missing. In the present work, we did a detailed analysis of experimental information collected during the last few years in the neutron-deficient region around lead with the aim to elucidate its asymmetric fission properties, address the question of its origin, and seek a connection between the "old" and the "new" islands of asymmetric fission.

6.2 Systematic study in sub-lead region

To get a deeper insight of fission mechanism, we analysed all the experimental information collected so far in sub-lead region using various approaches in a common framework and investigated the variation of fragment neutron and proton content with respect to fissioning system composition. Since the asymmetric components were clearly visible in the β-delayed and electromagnetic induced FFs mass distribution measurements, we deduced the mean position of the light and heavy partners, in mass $A_{L,H}$ for β-delayed and charge $Z_{L,H}$ for electromagnetic induced fission measurements, from the measured fragment A and Z distributions respectively. As discussed earlier in section 4.1, due to the complications associated with β-delayed and electromagnetic induced fission measurements, recently the route of heavy ion induced fusion fission reactions has been exploited to study the mass-asymmetric fission for neutron deficient nuclei in the sub-Pb region. In case of this fusion induced fission approach, the location of the asymmetric peaks were determined in the corresponding references [32, 33, 55, 57, 58] based on the adjustment of the mass distribution by a superposition of Gaussian functions. The observed variation of mean mass of the light and heavy fragment as a function of mass of the fissioning system A_{CN} is shown in Fig. 6.1. Overall, the mean mass of both the fragments were observed to increase linearly with increase in mass of the fissioning system. However, the rate of increase of mass for the lighter fragment group A_L was slower than that for heavier fragment group A_H.

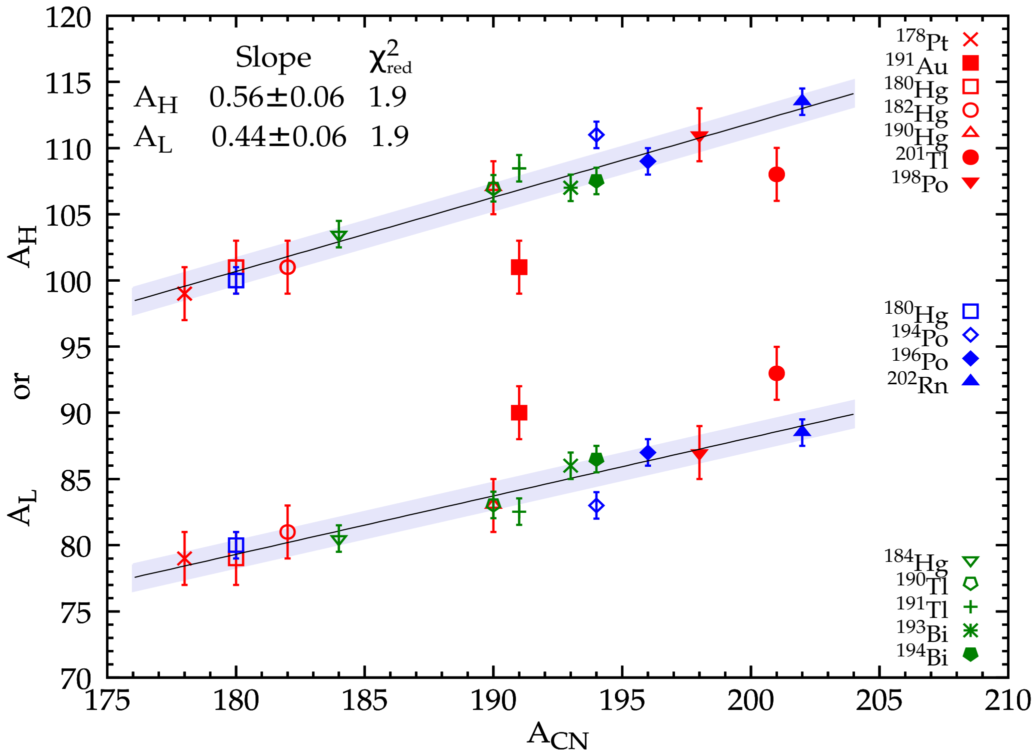

Figure 6.1: Mean mass of the light and heavy fragment as a function of mass of the fissioning system A_{CN}, from fusion induced fission [22, 32, 33, 55, 57, 58] (red), β-delayed fission (blue) [31] and electromagnetic-induced fission (green) [116].

We then deduced the mean proton and neutron numbers of the fission partners using the Unchanged-Charge-Density (UCD) assumption [117]. The obtained plot of deduced $Z_{L,H}$ and $N_{L,H}$ as a function of the total number of available protons (Z_{CN}) and neutrons (N_{CN}) respectively in the fissioning system are shown in Fig. 6.2

and Fig. 6.3. Distinctly different behaviours, in the way the neutrons and protons are shared can be seen in these figures. Interestingly, the light-fragment charge Z_L was observed to be confined within a narrow range around 36. On the contrary, the heavy-fragment charge Z_H showed a much stronger dependence on Z_{CN} with almost twice the slope observed for Z_L free fit. Both N_L and N_H were observed to increase monotonically as the number of neutrons N_{CN} to be shared increased.

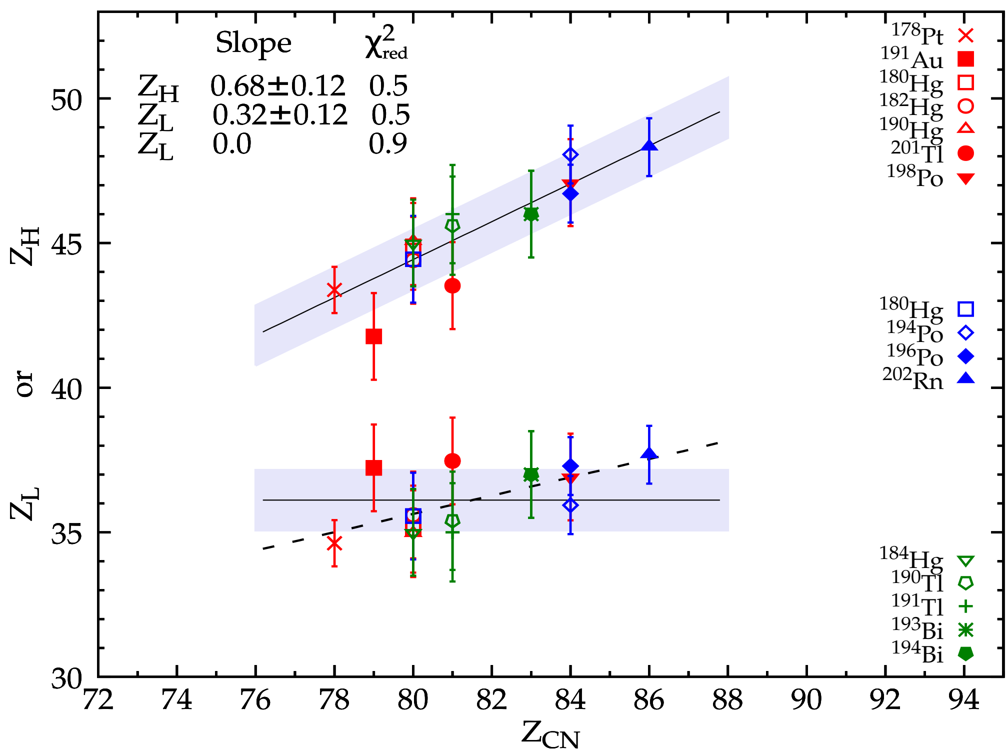

Figure 6.2: Mean proton, $Z_{L(H)}$ numbers of the light and heavy fragment as a function of fissioning system Z_{CN}, for the data shown in Fig 6.1.

Even though no preference for specific neutron sharing was evident in Fig. 6.2, we observed that the Z_L values for $N_L \geq 50$ were consistently higher (≈ 37) than those for $N_L \leq 50$ (≈ 35). This is the primary reason for the observed small slope

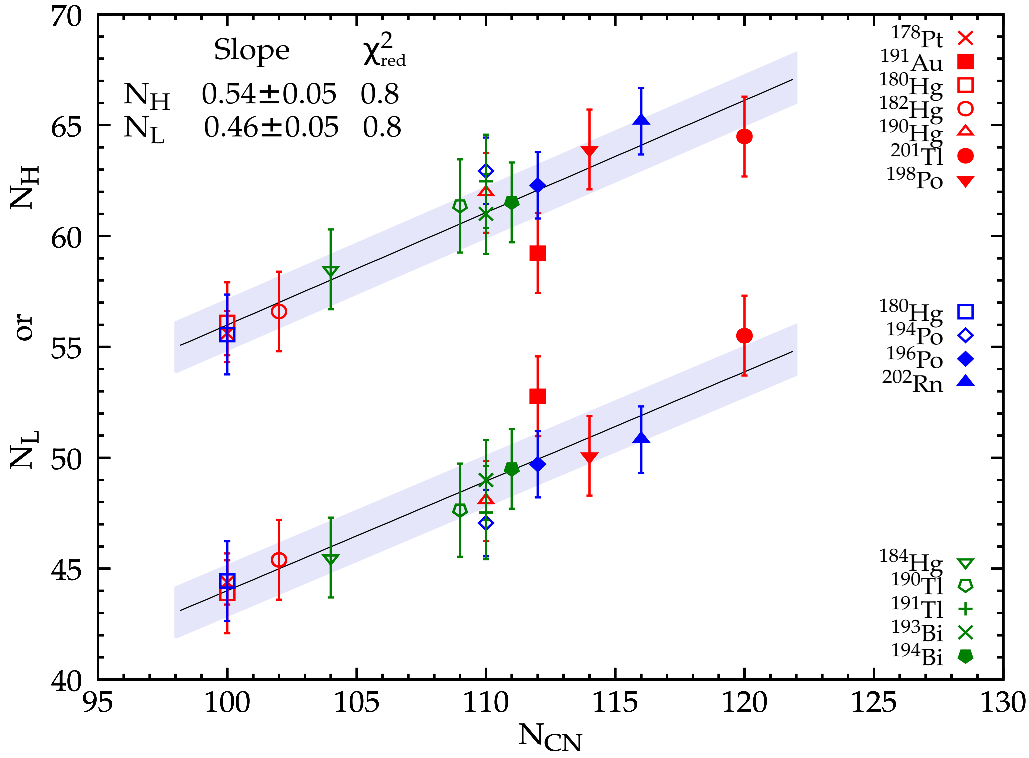

Figure 6.3: Corresponding mean neutron $N_{L(H)}$ numbers of the light and heavy fragment as a function of fissioning system N_{CN} for the data shown in Fig. 6.2.

in Z_L as a function of Z_{CN}. This phenomenon of higher proton number in case of $N_L \geq 50$ is probably due to the influence of the macroscopic restoring force that tends to equilibrate the charge and mass of the two fragments, and the protons coming from the neck [2, 113, 118]. Evidently a rather stable location of Z_L when compared for a diverse set of A_{CN} and N_{CN} implies that the light-fragment proton configuration plays the leading role in governing asymmetric fission of neutron-deficient nuclei around lead. This observation is at variance with previous interpretation which suggested that the leading role is played by neutrons [17, 29].

6.3 Fission-fragment mass distributions over the nuclear chart

In search for connection between "old" and "new" islands of asymmetric fission and to see how the mass distribution evolve in low energy fission across the nuclear chart we plotted measured FFs mass distribution of isotopes between platinium (Z_{CN} =78) and rutherfordium (Z_{CN} =104), as shown in Fig. 6.4. To cover an as wide as possible domain, the results from various experimental methods were included. This inevitably resulted in some spread in the initial excitation energy of the fissioning system. However as the shell effects are observed to be sustaining up to high $E^*_{B_f}$ [32, 55], the magnitude of the change of the distribution due to the spread in E^* of the systems plotted does not impact the present discussion.

As can be clearly seen in the Fig. 6.4, for nuclei in actinide region, asymmetric fission component starts to be visible for A_{CN} above $\approx$ 224, and persists up to A_{CN} $\approx$ 256. Beyond ^{256}Fm the appearance of symmetric fission is due to the summing-up of shell effects in the population of two fragments around ^{132}Sn in the heaviest transfermiums. On the other side, i.e for nuclei from radon to radium, symmetric fission again prevails for the lightest actinides due to the dominant influence of the macroscopic potential which outweighs the Z_H quantum effect that governs S1 and S2. In the newly identified island of asymmetric fission i.e in the sub-lead region, asymmetric fragmentation abounds again apparently due to observed leading role of light fragment proton number (Z_L $\approx$36). In the absence of calculation by a fundamental theory for this plotted wide domain of fissioning systems, we compared these experimentally obtained mass distributions with the prediction of semi-empirical model GEF (described in section 2.3.3) [61] (shown as red continuous line in Fig. 6.4). As discussed earlier, GEF code was initially developed and parametrised to reproduce data in well studied actinide region. Later, in a preliminary survey by Schmidt *et al* [2] based on four data points, it was observed that Z_L indeed plays a specially intriguing role. These data points, namely ^{180}Hg [18], ^{196}Po,^{202}Rn [31] and ^{201}Tl [101] were then further used for parametrization of GEF to reproduce data in pre-actinide region. So, overall the model performs impressively well for nuclei in neutron-deficient pre-actinides, heavy actinides and the fermium region. However, this code failed to reproduce the experimental observations in region of most neutron-deficient radium to thorium. This indicates that the competition between the structural effect(s) at play in a specific region and the macroscopic restoring force is not fully understood yet.

In earlier studies by Itkis *et al* [54], a weak persistence of the S1 and S2 modes in pre-actinides between ^{205}Bi and ^{213}At was observed with a tendency to die out when neutron deficiency increased. However, the observation of sizeable asymmetric components more close to symmetric split in ^{201}Tl was attributed to neutron shells [113]. Since according to the outcome of our investigation, the asymmetric fragment mass split in pre-actinide region is due to Z_L stabilization aided by specific N configurations with increasing N_{CN} [9, 113], we tried to understand ^{210}Po [54] data, which is ideally situated at the crossroads of the old and new islands, using all stabilization effects identified till now. As can be seen clearly in the inset of Fig. 6.4, FFs mass distribution for ^{210}Po can be nicely explained as a sum of macroscopic fission mode around $A_{CN}/2$, S1, S2 and this newly identified stabilization

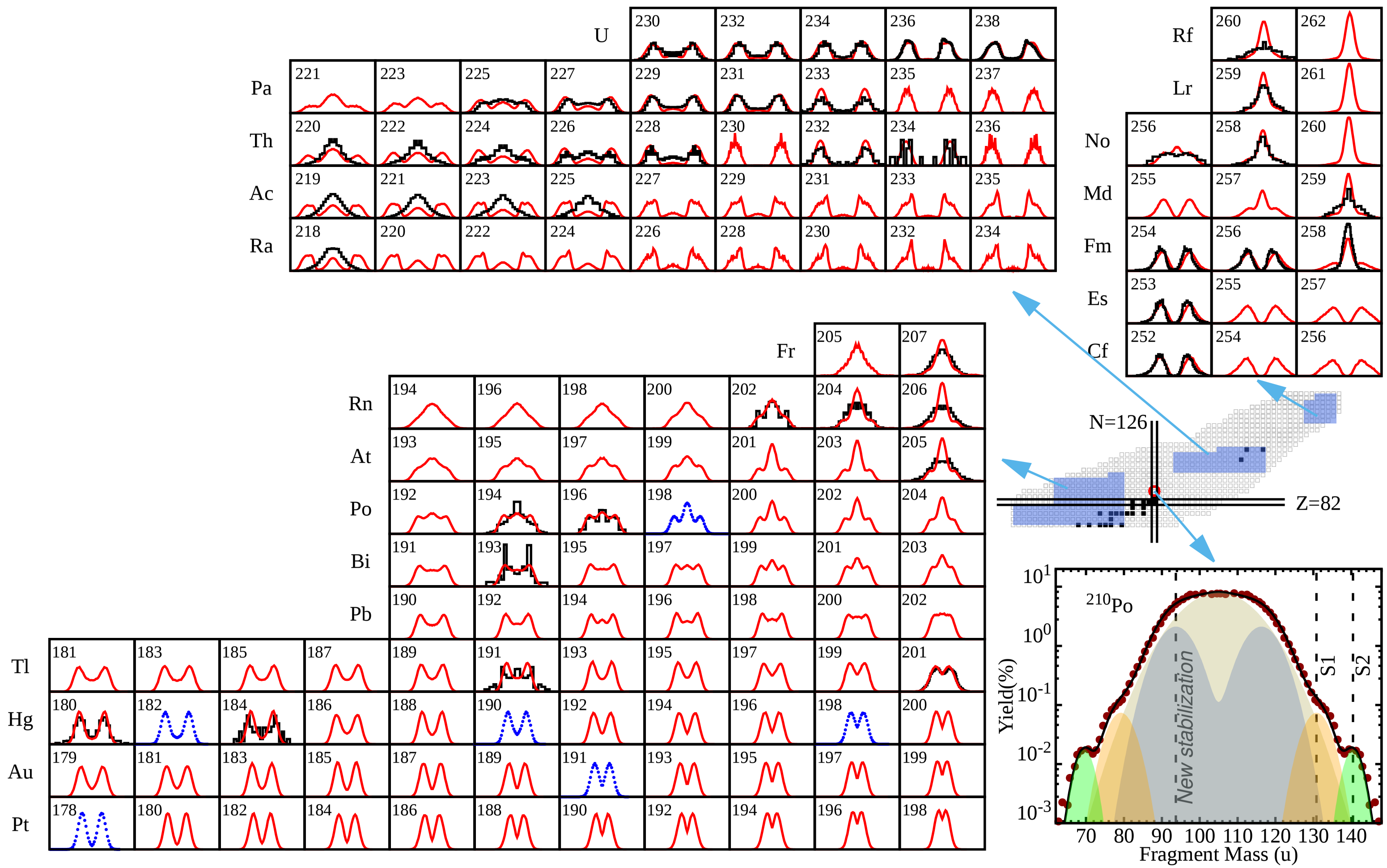

Figure 6.4: Fragment mass distribution of various systems across the nuclear chart from β-delayed fission [18, 31], heavy ion fusion induced fission [32, 33, 55, 57, 58], electromagnetic induced fission [10, 116], and multi-nucleon transfer induced fission [119], as well as spontaneous fission [120]. For legibility, only even-N systems are shown. Wherever the fragment Z was measured, mass was obtained under the UCD assumption. The experimental distributions (black histograms) are compared with calculations by the GEF model (red full lines) done at the actual E^* for each case. For fusion-fission, the GEF result obtained at low energy is shown (blue full dots), extrapolated from the good description by the model of measurements done at intermediate energy [33]. The inset shows the distribution of ^{210}Po at an excitation energy 9.5 MeV above the fission barrier [101] fitted using the "old" and "new" fission modes, see the text.

of $Z_L \approx 36$.

6.4 Unified description

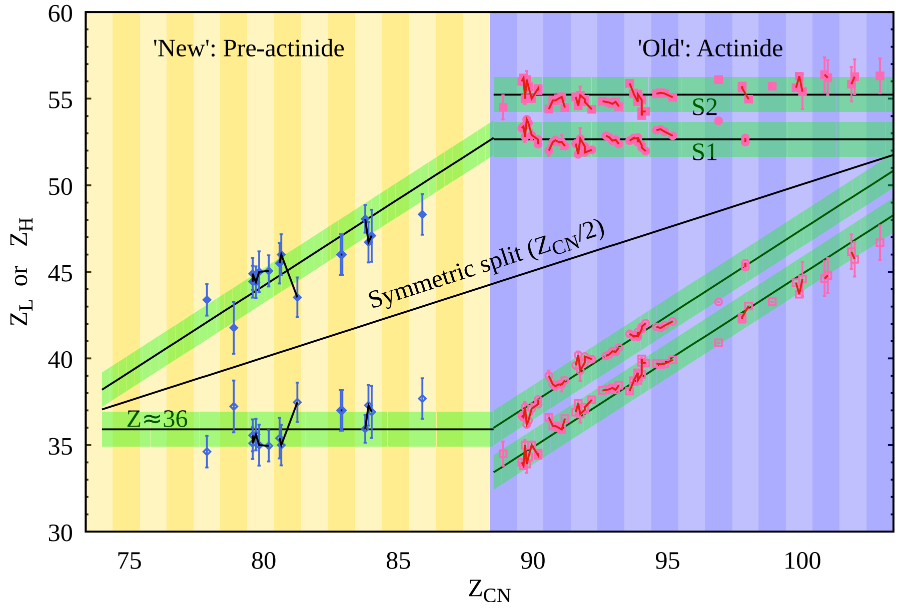

Figure 6.5: Evolution of the average $Z_{L(H)}$ positions for the asymmetric fission channel as a function of Z_{CN} from above rare earth to very heavy elements. For clarity, isotopes of a same element are shifted in the shaded region according to the mass. The points are from references [11, 17, 18, 31, 32, 33, 54, 55, 57, 114, 115, 116].

Interestingly, a complete description of the evolution of fragment mass distribution can be understood by plotting $Z_{L(H)}$ peak positions with respect to Z_{CN} all the way from above rare-earth to very heavy elements. As shown in Fig. 6.5, certainly there is a natural connection between the "old" (actinide) and "new" (pre-actinide) islands of asymmetric fission. As observed in the present work, in the pre-actinide region the light fragment position remains fixed at $Z_L \approx 36$ and the heavy fragment charge increases. However, after an interesting role reversal at the boundary (Z=88-89) of two islands, in the actinide region S1 and S2 modes of fission starts to dominate, forcing the light fragment to increase its charge with Z_{CN}. This observed geometric connection between these two islands established the general dominance of proton shells in low-energy fission.

6.5 Chapter summary

Present systematic analysis of the experimental information on fission of neutron-deficient nuclei in sub-lead region revealed the leading role played by the light fragment proton number $Z_L \approx 36$ in deciding fragment mass distribution. This result is in contrast with previous predictions where neutron shells were considered to be dominant for theoretical modelling of fission in pre-actinide region [17, 29]. This systematic analysis also allowed us to seek a connection between the "new" and the "old" islands of asymmetric fission. Combined with the previously established leading effects in the actinide region, this analysis demonstrated in an essentially "simple" way the general dominance of proton shells in low-energy fission for the first time. However, failure of semi- empirical code to reproduce the experimental observations in region of most neutron-deficient radium to thorium suggests a major deficiency in current understanding of the complex and quantitative interference of the various operating forces.

7

Summary & Outlook

The crucial investigations performed in the present thesis work helped us in getting an improved understanding of role of shell effects in deciding fission fragment mass distribution around A$\sim$200. A brief description of this research work highlighting the essential observations is given below.

In our measurement of fragment mass distribution in fission of ^{191}Au, formed via two very different entrance channels, ^{16}O+^{175}Lu and ^{37}Cl+^{154}Sm with E^*_{CN} $\sim$39-50 MeV and 46-64 MeV respectively, we observed significantly ($\sim$30%) broader mass distribution in case of ^{37}Cl+^{154}Sm system than those for ^{16}O+^{175}Lu at similar E^*_{CN} and $\langle \ell \rangle$. Failure of statistical relation (Eq.(4.1)), semi-empirical code GEF as well as the 4D Langevin dynamical model in explaining this enhanced width of the observed mass distribution in case of heavier projectile gave us conclusive evidence of substantial presence of quasifission for the more symmetric entrance channel. The Dinuclear system (DNS) model prediction of

22% quasifission in case of ^{37}Cl+^{154}Sm system was also found to be in good agreement with the experimental observation. Also, a systematic analysis of the available experimental data demonstrated significant presence of quasifission whenever heavier projectiles (Z≥17) were used with spherical or deformed targets to investigate fission of neutron deficient sub-Pb nuclei. These observations gave us a clear indication that not only the shell effects, but the dynamics in the entrance channel also have a significant role in influencing the fission of nuclei around A∼200. Hence, both these aspects, shell effects in the emerging fragments as well as dynamics in the entrance channel needs to be necessarily considered for interpreting the heavy-ion data unambiguously. Present work illustrates that for systems involving heavy projectiles (Z≥17), quasifission contribution should be taken care correctly while studying asymmetric CN fission in the mass region A∼200.

In our measurement of fragment mass and total kinetic energy properties for fission of ^{198}Po produced via ^{28}Si+^{170}Yb reaction with E^*_{CN} = 34.5, 37.0 and 44.1 MeV, we investigated the presence of multimodal fission along Po chain. In the analysis of this measurement we inferred the presence of asymmetric partitions by observing a weak flattening of TKE with mass, and the non-monotonic evolution of the fragment-mass distribution width with excitation energy. Considering the good description achieved by the GEF code for different measurements in the pre-actinide region as well as for our measurement of ^{198}Po with $E^*_{B_f}$=15.7 MeV, we did GEF calculation to trace back the fission properties of ^{198}Po close to fission barrier. The so obtained mass distribution is triple humped and contributes in establishing the gradual evolution along the polonium chain.

In a systematic analysis of the experimental information on fission of neutron-deficient nuclei in sub-lead region, we observed that the leading role in deciding fragment mass distribution is primarily played by the light fragment proton number $Z_L \approx 36$ (see Fig. 6.5). This result is in contrast with previous predictions where neutron shells were considered to be dominant for theoretical modelling of fission in pre-actinide region [17, 29]. Combined with the previously established leading effects in the actinide region, we can conclusively say that in general its the fragment proton shell that is primarily responsible for asymmetric fission. In the actinide region its proton shell of the heavier fragment while in pre-actinide nuclei its proton shell of the lighter fragment that is basically responsible for asymmetric mass split.

Future outlook:

From present study we conclude that even though the fusion-fission approach seems to be a feasible route to study asymmetric fission in pre-actinide region due to the restrictions associated with β-delayed and electromagnetic induced fission, an unambiguous interpretation of the heavy ion data for neutron deficient nuclei around A$\sim$ 200 calls for careful investigation of presence of quasifission. Understanding the process of quasifission on this side of extremely low fissility region will also be advantageous for its theoretical development. Our systematic analysis of heavy-ion data in pre-actinide region (discussed in section 4.4.1) also demonstrated a significant presence of quasifission whenever heavier projectiles (Z≥17) have been used to investigate fission of neutron deficient sub-Pb nuclei. Hence, use of heavier projectiles (Z≥17) should be avoided to investigate fission of neutron deficient sub-Pb nuclei. In this scenario, route of transfer induced fission and electromagnetic induced fission provides us a better opportunity to explore asymmetric fission in the sub-lead region.

As shown in Fig. 6.5, in our systematic analysis of extensive set of asymmetric fission data, we have observed that in general it is the fragment proton shell that is primarily responsible for asymmetric fission. However, more experimental data is clearly necessary around both, near the reversal boundary around Z_{CN}=88-89 and in the limits of $103 \leq Z_{CN} \leq 78$.

* On the lighter Z_{CN} side, the strength and cause of this newly identified $Z_L \approx 36$ stabilization is yet to be explored. More measurement of fission fragment mass distribution for neutron deficient nuclei in the region from Z_{CN}=80 (highly asymmetric, as already observed in β-delayed fission of ^{180}Hg) to Z_{CN}=72 (highly symmetric, according to the prediction of Fig. 6.5) is required to get a deeper insight of this $Z_L \approx 36$ stabilization.

* An extensive set of low energy fission measurement with high resolution, similar to the work done by Schmidt *et. al.* at GSI in the actinide region [10] (discussed in section. 1.3), needs to be performed in the pre-actinide region as well. By selecting appropriate pre-actinide projectile and a light target combination and using inverse kinematics, a secondary beam of nuclei with $Z_{CN} < 88$ can be generated which can further decay via electromagnetic

induced fission in presence of a heavy secondary target. Such a single experiment can answer many questions like, is the observed Z_L stabilization is coming from $Z_L \approx 36$ only or its a combined effect of two different stabilizations, say Z_L=34 and Z_L=38. How fast is this Z_L stabilization is vanishing with increase in N_{CN}/Z_{CN} etc.

* On the heavier side i.e for $Z_{CN} > 104$, linear continuity observed in Fig. 6.5 $Z_{L,H}$ behaviour suggests another role reversal, the light fragment formation this time being driven by the standard (S1 and S2) fission modes. A recent macroscopic-microscopic prescission point model indeed support this observation [121]. This region of fission in superheavy nuclei is yet to be explored experimentally.

* All these observations also give a crucial input and a new direction for theoretical modelling of the fission process where until now neutron shells are observed to play dominant role in deciding fragment mass split. The basic physics mechanism behind this observed phenomenon of dominant proton shells over neutron is yet to be investigated completely.

Bibliography

[1] A.N. Andreyev, et al., Rep. Prog. Phys. 81 016301 (2018), and references therein.

[2] K.-H. Schmidt, B. Jurado, Rep. Prog. Phys. **81** 106301 (2018), and references therein.

[3] O. Hahn and F. Strassmann, Naturwiss., 27, 11, 89, and 163 (1939).

[4] L. Meitner, O. R. Frisch, Nature **143**, 239 (1939).

[5] N. Bohr, J.R. Wheeler, Phys. Rev. **56**, 426 (1939).

[6] C. Weizsacker, Zeitschrift fur Physik **96**, pp.431-458 (1935).

[7] V. M. Strutinsky, Nucl. Phys. A **95**, 420-442 (1967).

[8] K.F. Flynn et al., Phys. Rev. C **5**, 1725 (1975).

[9] B. D. Wilkins *et al*, Phys. Rev. C **14**, 1832 (1976).

[10] K.-H. Schmidt *et al*, Nucl. Phys. A **665**, 221 (2000).

[11] C. Boeckstiegel et al., Nucl. Phys. A 802, 12(2008).

[12] C. Boeckstiegel *et al*, International Journal of Modern Physics E **18**, 873 (2009).

[13] M. Caamaño *et al*, Phys.Rev. C **88**, 024605 (2013).

[14] D. Ramos *et al*, Phys.Rev. C **99**, 024615 (2019).

[15] E. Pellereau *et al*, Phys.Rev. C **95**, 054603 (2017).

[16] G. Scamps and C. Simenell, Nature (London) **564**, 382 (2018).

[17] T. Ichikawa and P. Moller, Phys. Lett. B **789**, 679 (2019).

[18] A. N. Andreyev *et al*, Phys. Rev. Lett **105**, 252502 (2010).

[19] J. P. Unik *et al*, *Proc. Symp. on the Physics and Chemistry of Fission (Rochester 1973) vol 2* (Vienna:IAEA) p 19 (1974).

[20] H. W. Schmitt *et al*, Phys. Rev. **137**, B837 (1965).

[21] J. Elseviers *et al*, Phys. Rev. C **88**, 044321 (2013).

[22] M. G. Itkis *et al*, Sov. J. Nucl. Phys. **41**, 544 (1985); **43**, 1125 (1986); **47**, 4 (1988); **52**, 601 (1990); **53**, 757 (1991).

[23] P. Moller *et al*, Nature (London) **409**, 785 (2001).

[24] P. Moller *et al*, Phys. Rev. C **79**, 064304 (2009).

[25] M. Warda *et al*, Phys. Rev. C **86**, 024601 (2012).

[26] J. D. McDonnell *et al*, Phys. Rev. C **90**, 021302(R) (2014).

[27] S. Panebianco *et al*, Phys. Rev. C **86**, 064601 (2012).

[28] A. V. Andreev *et al*, Phys. Rev. C **93**, 034620 (2016).

[29] G. Scamps and C. Simenell, Phys. Rev. C **100**, 041602(R) (2019).

[30] W. U. Schroder and J. R. Huizenga, "Treatise on heavy-ion science, damped nuclear reactions," p. 115 (1984).

[31] L. Ghys *et al*, Phys. Rev. C **90**, 041301 (2014).

[32] Shilpi Gupta *et al*, Phys. Lett. B **803**, 135297 (2020).

[33] Shilpi Gupta *et al*, Phys. Rev. C **100**, 064608 (2019).

[34] F. Rejmund, *et al*, Nucl. Phys. A **678**, 215 (2000).

[35] M. Caamaño *et al*, J. Phys. G: Nucl. Part. Phys. **38**, 035101 (2011).

[36] D. Ramos *et al*, Phys. Rev.C **101**, 034609 (2020).

[37] D. L. Hill and J. A. Wheeler, Phys. Rev. **89**, 1102 (1953).

[38] C.Y.Wong, Phys. Rev. Lett. **31**, 766 (1973).

[39] M. Beckerman, Rep. Prog. Phys. **51**, 1047 (1988).

[40] W. Reisdorf, J. Phys. G: Nucl. Part. Phys. **20**, 1297 (1994).

[41] M. Dasgupta, D. J. Hinde, N. Rowley and A. M. Stefanini, Ann. Rev. Nucl. Part. Sci. **48**, 401 (1998).

[42] K. Hagino and Noboru Takigawa, Progress of Theoretical Physics, **128** 6(2012).

[43] K. Hagino, N. Rowley and A. T. Kruppa, Comput. Phys. Commun., **123** 143-152 (1999).

[44] R. Stokstad, "Treatise on Heavy-Ion Science", edited by D. A. Bromley, **3** 83 (Plenum, New York, 1985).

[45] W. J. Swiatecki, Phys. Scr. **24**, 113 (1981).

[46] S. Bjornholm and W. J. Swiatecki, Nucl. Phys. A **391**, 471 (1982).

[47] J. P. Blocki, H. Feldmeier, and W. J. Swiatecki, Nucl. Phys A **459**, 145 (1986).

[48] U. L. Businaro and S. Gallone, Nuovo Climento **5**, 315 (1957).

[49] M. Abe, KEK Report No. 86-26 **KEK TH-28** (1986).

[50] R. du Rietz *et al*, Phys. Rev. C **88**, 054618 (2013).

[51] D. J. Hinde *et al*, Phys. Rev. Lett. **74**, 1295 (1995).

[52] D. J. Hinde *et al*, Phys. Rev. C **53**, 1290 (1996).

[53] C. Simenel *et al*, Phys. Lett. B **710**, 607 (2012).

[54] M.G. Itkis, *et al*, Nucl. Phys. A **502**, 243c (1998).

[55] K. Nishio *et al*, Phys. Lett. B **89**, 748 (2015).

[56] R. Tripathi *et al*, Phys. Rev. C **92**, 024610 (2015).

[57] E.Prasad *et al*, Phys. Rev. C **91**, 064605 (2015).

[58] I. Tsekhanovich *et al*, Phys. Lett. B **790**, 583 (2019).

[59] K. Banerjee, *et al*, Phys. Rev. Lett. **122**, 232503 (2019).

[60] Ulrich Brosa, Siegfried Grossmann and Andreas Muller, "Nuclear Scission", Phys. Rep., **197** 167-262, (1990).

[61] The GEF code from www.cenbg.in2p3.fr/GEF.

[62] K.-H. Schmidt *et al*, Nucl. Data Sheets **131**, 107 (2016).

[63] C. Schmitt, K.-H. Schmidt and B. Jurado, Phys. Rev.C **98**, 044605 (2018).

[64] K.-H. Schmidt et al., Europhys. Lett. **83**, 32001 (2008).

[65] U Mosel and H. W. Schmitt, Phys. Rev. C **4**, 2185 (1971).

[66] A. Nasirov *et al*, Nucl. Phys. A **759**, (3) 342 (2005).

[67] G. G. Adamian *et al*, Phys. Part. Nucl. **47**, 1-48 (2016).

[68] B. Reusch *et al*, Z. Phys. A **288**, 391 (1978).

[69] B. B. Back, J. Phys. Conf. Ser. **282**, 012003 (2011).

[70] J. F. Martin *et al*, Eur. Phys. J **51**, 174 (2015).

[71] J. E. Escher *et al*, Rev. Mod. Phys. **84**, 353-97 (2012).

[72] G. Charpak *et al*, Nuclear Instruments and Methods, **62**, 262-268 (1968).

[73] A. Breskin *et al*, Nucl. Instrum. Methods A **221**, 363 (1984).

[74] S. Beghini *et al*, Nucl. Instrum. Methods A **362**, 526 (1995).

[75] Akhil Jhingan, Pramana **85**, 483 (2015).

[76] J. Toke *et al*, Nucl. Phys. A **440**, 327 (1985).

[77] R.K Choudhury *et al*, Phys. Rev. C **60**, 054609 (1999).

[78] J. Lindhardt *et al*, Math. Fys. Meed. Dan. Vid. Sels. **33**, 14 (1963).

[79] James F. Ziegler *et al*, Nucl. Instrum. Methods Phys. Res. B **268**, 1818 (2010); and references therein.

[80] N. Bohr, Phys. Rev. **58**, 654 (1940).

[81] Willis E. Lamb, Jr.,Phys. Rev. **58**, 696 (1940).

[82] Enrico Fermi, Phys. Rev. **57**, 485 (1940).

[83] Julian Knipp, E. Teller, Phys. Rev. **59**, 659 (1941).

[84] J. Lindhard, M. Scharff, H.E. Schiott, Math. Fys. Meed. Dan. Vid. Sels. **33**, 14 (1963).

[85] G.N. Knyazheva *et al*, Nucl. Instrum. Methods Phys. Res. B **248**, 7-15 (2006).

[86] P. Baldez *et al*, Nucl. Instrum. Methods Phys. Res. B **456**, 142-147 (2019).

[87] N. Bohr, B. R. Mottelson, Mat.-Fys. Medd. **18**, 8 (1948).

[88] H. L. Hall and D. C. Hoffman,J. Radiol. Nucl. Chem.142,53 (1990).

[89] F. Gonnenwein, in Nuclear Fission Process, edited by C.Wagemans (CRC Press, Boca Raton, FL, 1991).

[90] P. Moller and S. G. Nilsson, Phys. Lett. B, **31**, 283 (1970).

[91] M.G. Itkis, *et al*, Nucl. Phys. A **944**, 204 (2015).

[92] D. J. Hinde, M. Dasgupta, and A. Mukherjee, Phys. Rev. Lett. **89**, 282701 (2002).

[93] C. J. Lin *et al*, Phys. Rev. C **85**, 014611 (2012).

[94] A. C. Berriman *et al*, Nature (London) **413**, 144 (2001).

[95] R. Rafiei *et al*, Phys. Rev. C **77**, 024606 (2008).

[96] T. Rajbongshi *et al*, Phys. Rev. C **93**, 054622 (2016).

[97] W. Reisdorf *et al*, Nucl. Phys. A **438**, 212 (1985).

[98] P.N. Nadtochy *et al*, Phys. Rev. C **89**, 014616 (2014).

[99] K. Mazurek *et al*, Eur. Phys. J. A **53**, (4) 79 (2017).

[100] K. Kim *et al*, Phys. Rev. C **91**, 064608 (2015).

[101] M.G. Itkis, A.Y. Rusanov, Phys. Part. Nucl. **29**, 160 (1998).

[102] G. N. Knyazheva *et al*, Phys. Rev. C **75**, 064602 (2007).

[103] P. Moller *et al*, Phys. Rev. C **91**, 024310 (2015).

[104] A.J. Sierk Phys. Rev. C **33**, 2039 (1986).

[105] A. Gavron Phys. Rev. C **21**, 230 (1980).

[106] K. Mahata *et al*, Phys. Rev. C **92**, 034602 (2015).

[107] G.D. Adeev *et al*, Fiz. Elem. Chastits At. Yadra **19**, 1229 (1988).

[108] T. Ichikawa *et al*, Phys. Rev.C **86**, 024610 (2012).

[109] V. Liberati *et al*, Phys. Rev. C **88**, 044322 (2013).

[110] D. J. Hinde *et al*, Nucl. Phys. A **398**, 308 (1983).

[111] P. Moller *et al*, Phys. Rev. C **91**, 044316 (2015).

[112] N. Schunck and L. M. Robledo, Rep. Prog. Phys. **79**, 116301 (2016).

[113] S. I. Mulgin *et al*, Nucl. Phys. A **640**, 375 (1998).

[114] J.F. Wild *et al*, Phys. Rev. C **41**, 640 (1990).

[115] E.K. Hulet *et al*, Phys. Rev. Lett. **56**, 313 (1986).

[116] T. Gorbinet et. al., Scientific Workshop on Nuclear Fission dynamics and the Emission of Prompt Neutrons and γ-rays, Opatcja, Croatia (Sept 2014).

[117] R. Vandebosch and J.R. Huizenga, *Nuclear fission* (Academic, New York, 1973).

[118] J. Benlliure *et al*, Nucl. Phys. A **628**, 458 (1998).

[119] K. Hirose *et al*, Phys. Rev. Lett. **119**, 222501 (2017).

[120] E. K. Hulet *et al*, Phys.Rev. C **40**, 770 (1989) references and therein.

[121] N. Carjan *et al*, Phys. Rev. C **99**, 064606 (2019).